Simplified Dynamic Models for Modern Flying Vehicles

POLITECNICO DI TORINO

SCUOLA DI DOTTORATO
Dottorato inIngegneria Aerospaziale – XXVI ciclo

Tesi di Dottorato

Simplified dynamic models for modern flying vehicles

Irene Alice Piacenza

Tutore
Prof. Giulio Avanzini

Coordinatore del corso di dottorato
Prof. Fulvia Quagliotti

Febbraio 2014

For you, mum,
so near, so far.

Through dangers untold and hardships unnumbered,
I have fought my way here to the castle beyond the Goblin City
to take back the child that you have stolen,
for my will is as strong as yours, and my kingdom as great.
You have no power over me.
(cit. Sarah, Labyrinth)

Abstract

This dissertation contributes to the definition of minimum–complexity approaches that allows for representing realistic effects typical of modern fixed- and rotary-wing configurations, limiting as much as possible increase in order and overall complexity of the dynamic model of the class of aerial vehicles considered. In particular, the thesis deals with (1) the development of a novel low–order mathematical model for including structural deformation effects in the analysis of response to control inputs of flexible aircraft; (2) the derivation of a simplified models for unsteady aerodynamic effects, with an application to helicopter main rotor; (3) modeling and assessment of the maneuvering potential for a novel quadrotor configuration with tilting rotors.

A mixed Newtonian–Lagrangian approach is proposed for the derivation of flexible aircraft equations of motion, where Lagrange equations are used for flexible degrees of freedom, discretized by means of Galërkin method, whereas the evolution of transport degrees of freedom (position and attitude variables) is obtained by means of Newton second law and generalized Euler equation. A strong link with conventional rigid aircraft equations of motion is maintained, that allows highlighting those terms less relevant for aircraft response. When negligible, these terms are removed and a minimum complexity flexible aircraft model is derived, suitable for real–time simulation and control law synthesis.

Similarly, unsteady aerodynamic effects over a rotating blade are modeled by means of an available approach, namely the ONERA dynamic stall model. Some reasonable simplifying assumptions based on the comparison of simulation results with a quasi–static aerodynamic model are then derived and a minimum complexity, 6 degree–of–freedom helicopter model is proposed which takes into account the issues related to retreating blade stall.

Finally, an existing inverse simulation algorithm is applied for the first time to the determination of the control laws for tracking desired maneuvers by means of an unconventional quad-rotor configuration featuring four tilting rotors. This novel configuration allow access to an extended maneuver envelope and ad hoc instruments are needed for assessing its maneuvering potential. For all the considered problems, the approaches developed are demonstrated by means of numerical results, applied to a particular class of modern fixed- or rotary-wing aircraft, but the possibility of extending the results to different classes of vehicles is also highlighted.

Contents

1 Introduction **1**

1.1 Motivation 1

1.2 Problem Statement, Approach, and Contributions 2

1.2.1 Structure Flexibility Effects 3

1.2.2 Unsteady Aerodynamics Effects 4

1.2.3 Performance Potential Analysis 4

1.3 Literature Review 5

1.3.1 Flexible Aircraft Models 5

1.3.2 Helicopter Modeling 7

1.3.3 Unsteady Aerodynamics 8

1.3.4 Dynamic Stall 9

1.3.5 Quadrotor Modeling 9

1.3.6 Inverse Simulation Algorithm 10

1.4 Outline 11

2 Flexible Aircraft Model **12**

2.1 Introduction 12

2.2 Derivation of a Low-Order Flexible Aircraft Model 13

2.2.1 Transport and deformation variables 13

2.2.2 Translational dynamics 16

2.2.3 Rotational dynamics 17

2.2.4 Kinematic equations 18

2.2.5 Aerodynamic model 19

2.2.6 Deformation variable dynamics 19

2.2.7 Forces acting on the deformable elements 21

2.2.8 Tail surfaces 22

2.2.9 Equation of motion for deformation variables 23

2.2.10 Complete flexible aircraft model 24

3 Rotorcraft Mathematical Models **25**
3.1 Levels of Rotorcraft Modeling . . . 25
3.2 Helicopter Equations of Motion . . . 26
3.2.1 Main Rotor . . . 27
3.2.2 Fuselage . . . 28
3.2.3 Tail Rotor . . . 28
3.2.4 Empennage . . . 29
3.3 Main Rotor Model . . . 29
3.4 Unsteady Aerodynamics . . . 32
3.4.1 Extended thin airfoil theory . . . 32
3.4.2 Dynamic inflow motion . . . 37
3.4.3 Dynamic Stall Model . . . 40
3.4.4 The Unified Model . . . 42
3.5 Small Scale Rotorcraft Models . . . 42

4 Flexible Aircraft Dynamic Response **47**
4.1 Case Study . . . 47
4.2 Static deformations vs deformable aircraft . . . 49
4.3 Approximately constant moments of inertia . . . 53

5 Helicopter Unsteady Aerodynamics **57**
5.1 2D test case . . . 57
5.2 Main Rotor Results . . . 58
5.2.1 Unsteady Aerodynamics Complete Unified Model . . . 58
5.3 Simplifying assumptions considered . . . 61
5.3.1 Approximation of the derivatives . . . 61
5.3.2 Harmonic Truncation . . . 61
5.3.3 Comparison . . . 62
5.4 Complete Helicopter Results . . . 64

6 Quadrotor Dynamics **69**
6.1 Agility Potential . . . 69
6.1.1 Inverse Simulation Algorithm . . . 69
6.1.2 MPC algorithm . . . 71
6.2 Results . . . 72
6.2.1 U turn maneuver . . . 75
6.2.2 360° yaw turn straight flight . . . 76
6.2.3 90° roll tilt . . . 79
6.3 MPC control of a Quadrotor . . . 83

7 Conclusions **88**

Bibliography **91**

A Definition of the rotation matrices **98**
A.1 Coordinate Systems 98
A.2 Inertial reference frame 98
A.3 Body axes 99
A.4 Wind axes 99
A.5 Rotor reference frames 100
A.5.1 Non–rotating and Rotating shaft 100
A.5.2 Blade span 101
A.6 Tail rotor reference frame 101

B Evaluation of the Main Rotor loads **103**
B.1 Blade element kinematics 103
B.2 Aerodynamic loads 105
B.3 Inertial loads 106
B.4 Blade equations of motion 108
B.5 Dynamic twist 109
B.6 Lag damper 110
B.7 Equations summary 111

C Matrices and vectors definition for the Unsteady Thin Airfoil Theory **114**

D Helicopter Configuration Data **117**

List of Tables

3.1 Levels of rotor modeling ([65], [89]) 27
4.1 Aircraft data 48
4.2 Aircraft trim data 48
4.3 Aircraft eigenvalues for rigid (R), fully flexible (FF), quasi–static (QS), static torsion (ST), and constant inertia (CI) cases 51
5.1 Dynamic Stall Parameter typical values 58
6.1 Quadrotor data 72
6.2 Test cases characteristics 73
D.1 Helicopter configuration data. 118

List of Figures

1.1 Unconventional configurations of atmospheric vehicles: a) tiltrotor; b)Prandtl plane; c) NASA double–bubble; d)wing–body 2
2.1 Architecture of the flexible aircraft model. 14
2.2 Aircraft transport and deformation variables 15
3.1 Interacting main subsystems of an helicopter [65]. 26
3.2 Geometry of the airfoil. 32
3.3 Physical meaning of the first three shape functions. 35
3.4 Static stall illustration 40
3.5 Unified model operating scheme 43
3.6 Quad-rotor configurations: a) conventional; b) with tilting rotors. . . 44
4.1 Linear density and stiffness distribution for deformable elements: (a) wing; (b) fuselage. 47
4.2 Root locus: comparison between rigid, flexible, and quasi-static deformation models. 50
4.3 Open-loop response to a 2 deg step command on the elevator deflection, rigid, complete and static cases comparison. 51
4.4 Open-loop response to a 1 deg doublet command on the aileron deflection, rigid, complete and static cases comparison. 52
4.5 Comparison of root loci for rigid model, completely flexible, and without inertia effects. 54
4.6 Open-loop response to a 2 deg pitch-down step command on the elevator deflection, with or without inertia properties variations. 55
4.7 Open-loop response to a 2 deg doublet command on the aileron deflection, with or without inertia properties variations. 56
5.1 Comparison between $C_L - \alpha$ curves obtained using the parameters defined in Tab. 5.1 for $k = 0.1$ 59
5.2 $C_L - \alpha$ curves obtained for $V_S = 25.7 m/s$ for each blade section, for the quasi–static C_L (solid line), complete (dash–dotted line), and the two approximate cases (dashed line for the first, dotted the second). . 63
5.3 Comparison of $\dot{\beta}$ response considering the complete (continue) and two approximate cases. 64

5.4 Comparison of β response considering the complete (continue) and two approximate cases. 65
5.5 Comparison of α response considering the complete (continue) and two approximate cases. 66
5.6 UH–60 commands evaluation for unsteady aerodynamics (continue), baseline (dashed), and Flightlab (dotted) models compared to flight tests 67
5.7 UH–60 required power evaluation for unsteady aerodynamics (continue), baseline (dashed), and Flightlab (dotted) models compared to flight tests 68
6.1 MPC–IS scheme [89]. 72
6.2 U-turn: desired x (a) and y (b) inertial speed. 73
6.3 Yaw rotation: desired ψ (a) and x inertial speed (b). 74
6.4 Roll tilt: desired ϕ (a) and x inertial speed (b). 74
6.5 Inertial speeds for the U turn maneuver, comparison between the standard case (dashed line) and the tilting rotor configuration (solid line) 76
6.6 Body speeds for the U turn maneuver, comparison between the standard case (dashed line) and the tilting rotor configuration (solid line) 77
6.7 Euler angles variation for the U turn maneuver, comparison between the standard case (dashed line) and the tilting rotor configuration (solid line) 77
6.8 Rotor speed commands for the U turn maneuver, comparison between the standard case (dashed line) and the tilting rotor configuration (solid line) 78
6.9 Tilting rotors angle command for the U turn maneuver 78
6.10 Inertial speed for the 360° yaw turn maneuver, comparison between the standard case (dashed line) and the tilting rotor configuration (solid line) 79
6.11 Euler angle variations for the 360° yaw turn maneuver, comparison between the standard case (dashed line) and the tilting rotor configuration (solid line) 80
6.12 Rotor speed command for the 360° yaw turn maneuver, comparison between the standard case (dashed line) and the tilting rotor configuration (solid line) 81
6.13 Tilting rotors angle command for the 360° yaw turn maneuver, comparison between the standard case (dashed line) and the tilting rotor configuration (solid line) 82
6.14 Inertial speed for the 90° roll tilt maneuver 82
6.15 Euler angle variations for the 90° roll tilt maneuver 83
6.16 Rotor speed command for the 90° roll tilt maneuver 83

6.17 Tilting rotors angle command for the 90° roll tilt maneuver 84
6.18 Inertial speeds for the U turn maneuver MPC–IS algorithm 85
6.19 Body speeds for the U turn maneuver MPC–IS algorithm 86
6.20 Euler angles variation for the U turn maneuver MPC–IS algorithm . . 86
6.21 Rotor speed commands for the U turn maneuver MPC–IS algorithm . 87
6.22 Tilting rotors angle command for the U turn maneuver MPC–IS algorithm 87
A.1 Wind axes reference frame. 99
A.2 Non–rotating shaft reference frame 100
A.3 Rotating shaft reference frame 101
B.1 UH60 lag damper geometry. 110

Chapter 1

Introduction

1.1 Motivation

In the last years a wide range of innovative configurations for aerial vehicles has been developed. These new configurations (Fig. 1.1) can be a cross–over between standard configurations (tiltrotor aircraft), or an evolution of standard ones (like the double–bubble proposed by NASA), but sometimes they represent dramatic changes with respect to previous configuration paradigms (as in the case of Prandtl plane or the blended wing–body airliner). Some of the problems that need to be faced in order to simulate the flight dynamics of such unconventional vehicles are quite common, but sometimes specific issues need to be addressed in order to derive reliable simulation models. As an example flexibility of lifting structures (wings or blades), unsteady aerodynamics effects induced by non–stationary periodic flow conditions, are aspects that must be modeled independently on the vehicle considered if they are relevant for the considered configuration. These effects may affect the ride comfort. Other aspects, such as vehicle control, are specific to the particular configuration considered (rotary vs fixed wings, redundancy of control surfaces, etc).

Traditional methods for flight dynamics analysis can fail by large amounts in identifying correctly the expected behavior of these unconventional configurations. This work is thus aimed at developing simplified models that take into account some of these aspects, and with models that are suitable for preliminary design, real–time simulations, and synthesis of control laws. The effects are analyzed in different frameworks, because even if there is a strong dependency on the flight condition, the model developed could be applied with some minor modification also to a different vehicle.

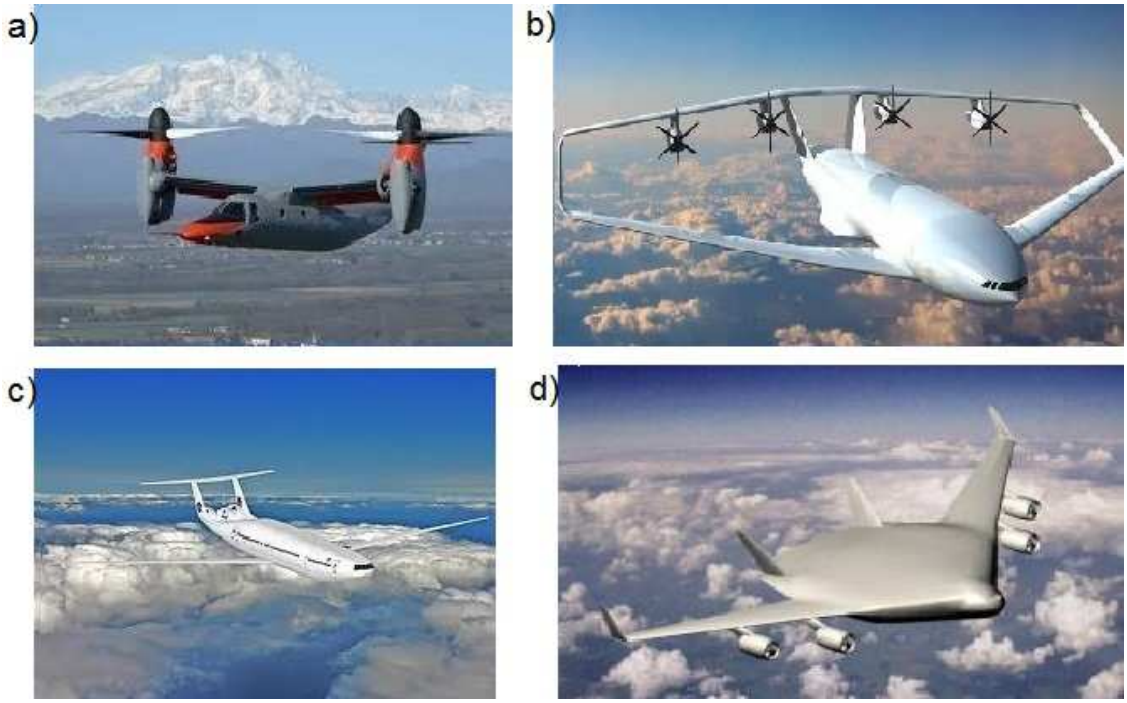

Figure 1.1: Unconventional configurations of atmospheric vehicles: a) tiltrotor; b)Prandtl plane; c) NASA double–bubble; d)wing–body

1.2 Problem Statement, Approach, and Contributions

The analysis of flight mechanics is an important task in the development of new vehicles. The development of mathematical models capable of describing the most relevant features of aerial vehicles behavior represented a fundamental need over the whole aviation history. When properly linked with suitable numerical techniques, these models allow for the evaluation of vehicle performance, agility potential and handling qualities with various degrees of reliability, depending on model complexity and availability of data.

The available models, thanks to modern advances in computation capabilities, can reach high levels of complexity when various effects are taken into account. The problem with such models is that the level of detail of the characteristics of the vehicle considered and the computational effort needed are both too great to allow for their use during the preliminary design phase when many features of the configuration are still not known with sufficient detail, or for piloted simulations, when computational effort is limited by the requirement of running the model in real time. The need for simplified models for the analysis of the dynamic response of aerial vehicles is still significant and often neglected. An example of this philosophy

is discussed for the case of helicopter rotor aerodynamics in Ref. [69]. Peters in this paper explain the success of the dynamic inflow method with five fundamental reasons:

- *the various models and improvements have always come in response to important, yet unexplained, experimental results;*
- *the response to those results was invariably based on sound physical intuition as to the nature of the discrepancies;*
- *the model improvements at each step were based on engineering physics, rather then heuristic fit of data;*
- *the models included only enough physics to explain the phenomenon, and no more;*
- *each model was hierarchical to earlier models so that no model was ever replaced.*

The present study is focused on three different aspects, that represent a wide benchmark of typical flight mechanics problems.

1.2.1 Structure Flexibility Effects

Stemming from the work by Tuzcu and Meirovitch, the main objective of the first part of the work is to develop a minimum complexity model for flexible aircraft, capturing the most important interactions between structural dynamics and overall vehicle motion variables. This is done by taking into account the effects of bending and torsion of wing and fuselage on aircraft translational and rotational motion. The modeling approach suits the representation of the dynamic behavior of large commercial transport aircraft, for the development of real-time simulators and the synthesis of guidance and control laws (*e.g.* a stability and control augmentation systems, autopilots, etc.), where the importance of keeping model complexity down to a minimum level is crucial for simplifying the control system task. The approach proposed is based on the idea of splitting the equations into two classes (mixed Newtonian-Lagrangian approach), using the conventional equations of flight dynamics for transport degrees of freedom and a Lagrangian formulation for flexible dynamics. The assumed modes method [45] is at the basis of the derivation of a low order model for deformation variables. This method allows for representing major features of structure deformation by means of a limited set of base functions that naturally fulfill structure boundary conditions (e.g. clamped-free beam for half-wings), when comparison functions are employed [45]. The same model can be applied with only minor modifications also for the description of rotor blade flexibility.

Novelty of the method implemented lie in the overall simple representation of the problem and in the analysis of the coupling between the effects due to the flexibility (e.g. inertia moments changes) and the dynamic response of the aircraft. While studies on blade flexibility have been widely covered [31, 35, 84, 90], similar works for the analysis of wing flexibility are less common, and are are even more sporadic research that consider the interaction with the flight mechanics with a low–level model.

1.2.2 Unsteady Aerodynamics Effects

The analysis of the effects of unsteady aerodynamics and dynamic stall on an helicopter rotor has been performed. First a linear airloads theory was applied, thus obtaining a set of generalized loads, that depend on generalized coordinates, i.e. a representation of angle of attack, plunge motion, and morphing of the airfoil, and on flowfield geometry, including the induced inflow. The representation of the induced inflow is different in 2D and 3D cases, thus both models will be presented in the following sections. The presence of dynamic stall modifies the loads obtained. The method implemented considers that dynamic stall correction factor depends on the actual conditions of the flow, and on the difference between the linear and static stall airloads coefficients. Wind tunnel test data are available mainly for the 2D cases, thus in the first a comparison was made in that condition. Then a comparison between static coefficients and unsteady aerodynamics rotor model was performed, and eventually some simplifying assumptions were derived. The validity of the model was discussed by means of a set of simulations for a complete helicopter dynamic model response considering (1) static loads, (2) unsteady aerodynamic loads, and (3) the simplified version of the latter.

Contribution of the present work is on the model simplifications used, that allow for a compact representation of the problem, still accounting for the main effects on the flight dynamics.

1.2.3 Performance Potential Analysis

In the third part of the study, an innovative quad–rotor configuration with tilting rotors is considered and ad hoc methods are developed for analyzing its maneuvering and agility potential, when compared to a conventional quad–copter. Control of a conventional quad-rotor is based on the variation of thrust developed by the four rotors, which is achieved by variations of rotor rotation rates. In hover all rotors provide equal thrust, such that the total equals vehicle weight. Two rotors turn in one direction and two in the opposite one, so that the overall yaw aerodynamic moment is cancelled (Fig. 3.6.a). Yawing control moments are obtained by unbalancing these aerodynamic moments by accelerating the rotors spinning in one

direction and slowing down the other two. Pitch and roll moments are obtained by unbalancing the thrust of forward and rear or lateral rotors, respectively, for a conventional cruciform configuration. A variation of the rotation rates of all the rotors allows for vertical acceleration and maneuvers at a load factor greater than one. The possibility of tilting the rotors allows for a significantly greater flexibility in obtaining control moments. With 4 more control variables, the system becomes redundant, and it is possible to control flight conditions and perform maneuvers simply unachievable for a conventional quad-rotor configuration with fixed propellers. A patent request has been issued for the configuration discussed here [6]. As an example, it is possible to accelerate and fly in forward flight without the need for pitching the vehicle down. In order to determine the control action necessary for performing a prescribed maneuver, an inverse simulation algorithm is applied. Inverse simulation has been considered in the past as a useful and versatile tool for investigating several aspects of both fixed- and rotary-wing vehicle dynamics, [87]. An integration approach is here applied, which is derived from an algorithm that was successfully applied to the evaluation of helicopter handling qualities, [7].

The quadrotor considered has an unconventional configuration that lead to redundancy on the controls, that make the problem of control quite different from the standard set up. In addition the extended inverse simulation algorithm used in [7] was applied for the analysis of the quadrotor considering a more complex model for the forward simulation.

1.3 Literature Review

1.3.1 Flexible Aircraft Models

Until recent times the additional complexity of flexible modes in the derivation of aircraft dynamic equations was not necessary, and the development of simulation models in the framework of atmospheric flight dynamics has been carried out for almost a century under the assumptions of rigid aircraft [11]. As a consequence, coupling between aeroelasticity and flight dynamics was neglected, thus limiting resulting model complexity. This was possible, when structural dynamics did not significantly affect aircraft response to either pilot inputs or external disturbances, structural modes being faster than the fastest modes of aircraft dynamics (short period and roll subsidence poles).

In spite of these practical considerations, the study on flexible aircraft models has been undertaken since the late 50s. The unavailability of analytical solutions on one side and, on the other hand, the lack of sufficient computational power for dealing with the complex models necessary for representing flexible aircraft dynamics, made it impossible at the time to tackle the problem without preliminarily

considering strong simplifying assumptions [63, 80, 83]. Nonetheless, many of the most promising approaches for developing a flexible aircraft simulation model, still adopted nowadays, were derived during this early period.

As a major example, Milne [63] proposed a general approach for flexible aircraft longitudinal motion, under the assumption that both flexible deformations and increments of rigid-body variables from trim conditions were small. Three possible choices for the aircraft-fixed reference frame were considered in Ref. [63], in order to describe translational and attitude dynamics of a flexible aircraft, namely attached axes, mean axes and principal axes. Mean axes were considered as the best choice, as the contribution of deformation rate to the total angular momentum vanishes, when represented in this particular reference frame, thus allowing to inertially decouple transport degrees of freedom (rotation and translation) from deformation ones. Another important milestone in the development of elastic aircraft models was set by Cavin III and Dusto [14], who used Hamilton's principle to derive the equations for the flexible body, looking for approximate solutions by means of the finite elements method.

In the late 80s Buttrill, Airbuckle and Zeiler [12] created an integrated nonlinear aircraft model with flexible degrees of freedom using Lagrange equations in a mean axes reference frame for a F/A-18 aircraft. Unfortunately, an accurate estimate of the position of the mean axes is far from trivial. This issue significantly affects the overall uncertainty level of the model, and it makes the use of this approach rather difficult in practice, when a reasonable approximation for their position relative to the aircraft structure needs to be sought and/or a suitable procedure for their determination from measurements realistically available on-board is required for active control of the elastic aircraft.

Alternative approaches for modeling flexible aircraft dynamics not based on the use of mean axes began to emerge in the late 90s, usually associated to the problem of control law design. Meirovitch and Tuzcu [61] derived a flexible aircraft model based on the formulation proposed by Meirovitch for flexible spacecraft [57], later extended to generic flexible bodies [58] and flexible multibody systems [60] modeled as a system of beam(s). A hybrid system of ordinary (for transport degrees of freedom, namely position and attitude variables) and partial differential equations (with proper boundary conditions for elastic degrees of freedom) in terms of quasi-coordinates was derived. Transport variables are here associated to position and attitude of a set of pseudo-body axes, fixed to the undeformed structure.

During the derivation based on a Lagrangian approach, the quasi-coordinate system takes into account that some of the "velocity variables" (*e.g.* aircraft speed and angular velocity expressed in terms of body frame components) are not the derivatives of "position variables" (*e.g.* center of mass position vector, and Euler angles). The formulation proposed by Meirovitch and Tuzcu is mathematically elegant and effective in dealing with the problem, where the use of quasi-coordinates

allows for a description of transport degrees of freedom in terms of standard flight dynamic variables (namely translational velocity $\boldsymbol{V}_B = (u,v,w)^T$ and rotational rate components $\boldsymbol{\omega}_B = (p,q,r)^T$). At the same time, the derivation of the equations of motion via a fully Lagrangian approach becomes more cumbersome, because of the presence of additional terms introduced by the kinematic equations that relate position and velocity variables. Moreover, a hybrid system of ordinary and partial differential equations is obtained, that needs some form of discretization. After the discretization, the identification of the origin of all the terms derived during the procedure, from the global expression of the Lagrangian to the final finite order system of nonlinear differential equations may not be straightforward.

1.3.2 Helicopter Modeling

The choice of helicopter model is fundamental in order to study performance and handling qualities. Since the beginning of helicopter engineering, mathematical models of increasing complexity and detail have been proposed. A helicopter model needs to "embody the important aerodynamic, structural and other internal dynamic effects (e.g., engine, actuation) that combine to influence the response of the aircraft to pilot's controls and external atmospheric disturbances" [65]. Usually a greater effort is necessary for the study of main rotor dynamics. For this reason Padfield [65] introduced a classification based on the complexity of rotor modelization levels that will be described in detail in the next chapter.

Most of the textbooks on helicopter dynamics present a model for the description of its dynamic response. Bramwell [10] described a relatively simple model that can be useful for preliminary design as well as for the physical interpretation of dynamic and aerodynamic phenomena. No dynamic equations are involved, but only static equations derived from momentum theory. Padfield [65] moves forward in developing a static model that features an equivalent hinge stiffness in the center of the rotor, suitable for describing articulated and hingeless rotors. Other works use second order TPP (Tip Path Plane) models for the evaluation of rotor loads transmitted to the fuselage, defining empirical correction factors in order to match the helicopter performances [3, 42, 49, 79].

A simplified first order TPP model was proposed by Heffley and Minch [32] in order to minimize the number of parameters necessary to represent the helicopter for pilot training purpose. In this work a quasi–static uniform inflow model is assumed, but the use of a uniform dynamic inflow model is a rather straightforward possible extension.

The work by Chen et al. [15] presents a second order TPP model for articulated and teetering rotors, considering for the blade flapping a Fourier series truncated at the first harmonic coefficients. Also in those work the aerodynamic considered for blade sections is linear, with static uniform inflow. Tail rotor is described with a

quasi–static TPP approach, that includes interference from main rotor downwash.

Individual blade models have been used by Howlett [39, 40] and Kim [48] for the description of the UH–60A helicopter. This model includes a full non–linear description of fuselage aerodynamics, rigid articulated blades, a triangular dynamic inflow for the main rotor [73] and a dynamic uniform inflow for the tail rotor. Flexibility effects on blades and fuselage, with the only exception of blade twist are neglected. Also unsteady aerodynamic effects are not included in the model.

More recently, the description of blade flexibility and aerodynamic advanced features allowed for the derivation of more realistic, but very complex helicopter models. Regarding blade flexibility a one–dimensional finite element is often used to model deformation in flap and lag directions, torsion along the blade span, and elongation. An example of fully flexible rotor model is presented in [31, 90].

1.3.3 Unsteady Aerodynamics

The first thin airfoil unsteady aerodynamic theory was developed by Max Munk in 1920 [64]. This study allows to determine aerodynamic loads on an airfoil easily, using the hypothesis of a two dimensional flow in a non–viscous, incompressible fluid, and small angles of attack. The work by Munk derived general integral relationships for the zero lift angle, static pitching moment, and center of pressure, and demonstrated that these are properties of only the mean camber line geometry for sufficiently thin airfoils.

Thin airfoil theory was later refined by Theodorsen and Garrick [85,86] in order to include also the study of the mechanism of flutter. Using a simple harmonic motion for the angle of attack and considering the Kutta condition, Theodorsen obtained a frequency–response function for the airfoil. Further extensions of this theory were carried out in the next two decades. Von Kármán [92] analyzed the leading edge suction peaks on a thin airfoil. Garrick [27] used Von Kármán equations to determine the drag (or propulsive) force generated by flapping airfoils. Isaacs [41] extended Theodersen theory considering that also the free stream can undergo harmonic oscillations. Greenberg [30] stemmed from the work of Isaacs and considered some simplification on vortex spacing. Loewy [53] generalized Theodorsen theory for a helicopter in hover or climb. The common characteristic of all these methods is that the analysis is carried in the frequency domain. The study of unsteady aerodynamic effects in the time domain was focused mostly on indicial methods [44,93] until 1970. In the following twenty years many studies proposed methods for transforming the response from the frequency to the time domain. One of the solutions proposed to this problem is based on the use of approximate Padé functions [18, 20, 21, 91].

More recent work [28] analyzed the possibility of converting CFD results into reduced order models that represent the non–linear behavior with adequate accuracy.

All the models described above are two–dimensional, thus cannot be directly

applied to 3D cases. The method derived by Peters et al. [72, 75, 76] uses a Glauert expansion, basing the theory on potential flow with a non-penetration boundary condition on a thin surface in two dimensions, and applying the Kutta condition on the trailing edge. There are many advantages in using this model. As an example, Chebychev polynomials can be used for deriving a simple description of the airfoil motion. Moreover, this model could be coupled with both 2D or 3D induced inflow models. Ref. [76] added also the possibility to consider unsteady free stream velocity. The limited number of terms required to describe the phenomena make this model suitable for the preliminary analysis of airfoil aerodynamics, thus it was implemented in the present work.

1.3.4 Dynamic Stall

The phenomenon of dynamic stall is one of the limiting factor for high speed helicopter performance. For fixed wing aircraft stall occurs at low speed, whereas for helicopters it will occur at relatively high velocities. That is because the advancing and retreating blades work in different conditions at high speed the advancing blade operates at low values of angle of attack, but close to shock induced separation boundary. On the other hand, the retreating blades operate at lower speed, with large angle of attack, close to the airfoil stall condition. The condition in which the blade operates are not constant, due to blade flapping, cyclic pitch inputs, velocity fluctuations induced by rotor rotation in forward flight and wake inflow. For this reason the phenomenon is referred to as dynamic stall.

CFD methods have been developed to analyze dynamic stall phenomenon, but the computational effort required is large not suitable for flight mechanics applications such as real time simulation.

Mathematical models currently in use rearrange the results from 2D oscillating wind tunnel experiments, either obtaining lookup tables of parameters (resynthesis models, [13, 26]) or representing the essential physics using sets of linear and non–linear equations for the aerodynamic loads, that use a set of empirical coefficients (semi–empirical models, [8, 23, 29, 43, 50, 77]). Most of these models are reviewed in Ref. [49].

The dynamic stall model used in this work is the ONERA method [77], including the modification proposed by Peters in [68].

1.3.5 Quadrotor Modeling

In the last 20 years the study of Unmanned Vertical Take Off and Landing Vehicles (VTOL UAVs) has raised a growing interest. In this framework, quad-rotors and other multi-rotor configurations achieved an increasing popularity, because of their mechanical simplicity, low cost and availability of reliable off–the–shelf vehicles.

This makes this class of platforms ideal for various mission scenarios and research on autonomous flight.

As an example, the Stanford Testbed of Autonomous Rotorcraft for Multi-Agent Control (STARMAC) quad-rotor helicopter is one of the many platforms analyzed in the literature, [37]. For a standard configuration load-factor is controlled by total thrust, and lateral and longitudinal accelerations are controlled through pitch and roll angles of the aircraft. The main goal of the control is to minimize the effects of disturbances. In Ref. [37] this is demonstrated for a rather complex simulation model, where blade flapping and total thrust variation in translational flight are considered.

The work by Stingu and Lewis, where the design and manufacturing of a quad-rotor is presented, provides a simpler 6 DoF simulation model for quad-rotors, [81]. The main issue of this paper is to obtain a simple control system that successfully stabilizes a custom-built quad-rotor platform in hover, in order to have a user-friendly semi-autonomous machine.

Most of the quad-rotors found in literature are very small, with an overall mass of less than 3 kg. One of the most notable exceptions is represent by the X-4 Flyer, [78]. Also in this case the model used for simulations and the control design are both quite standard, and a PID controller is designed to stabilize the dominant decoupled pitch and roll modes.

More recent studies are focused on the development of a self-stabilizing and self-navigating quad-rotor. The problem of navigation and autonomous flight for this class of vehicles, as well other VTOL UAVs, are well discussed in [47] and [62].

1.3.6 Inverse Simulation Algorithm

Inverse simulation has been considered in the past as a useful and versatile tool for investigating several aspects of both fixed- and rotary-wing vehicle dynamics, [87]. A wide plethora of methods for solving inverse simulation problems in flight mechanics has been considered, that can be broadly grouped into three major categories:

- differential methods, [46], suitable for nominal problems only, where the number of control inputs equals that of tracked variables;

- integration methods, [33], where the required control action is evaluated over a discrete time interval and can handle also redundant problems (e.g. by means of a local optimization approach, [16]);

- global methods, where the time-history of the control variable is determined over the whole duration of the tracked maneuver by means of a variational approach, [9].

An integration approach will be applied in this work, which is derived from an algorithm that was successfully applied to the evaluation of helicopter handling qualities, [7].

1.4 Outline

In what follows, Chapters 2 is dedicated to the description of the mathematical model used for the description of flexible aircraft dynamics. The derivation of the equation of motion of the aircraft are described in this chapter, considering the Netwonian approach for the evolution of the transport degrees of freedom, and Lagrangian for the elastic degrees of freedom of the two half–wings and the aft–fuselage. Chapter 3 is dedicated to the description of rotorcraft models. First the complete helicopter set of equation are presented, the the unified model implemented for the derivation of the unsteady aerodynamic loads is discussed, for both the 2D and 3D cases. Finally in the last part the simplified dynamic of a small quadrotor is presented. Chapter 4, 5, and 6 present the results obtained for the model described. In Chapter 4 the dynamic response of a transport aircraft is presented comparing the rigid, fully flexible, quasi–static, and without inertia variation cases. Chapter 5 present some results for the analysis of helicopter response considering unsteady aerodynamics on the blades. In the first part the 2D case is considered, then the complete rotor response is analyzed considering some simplifying assumptions, and in the end the complete helicopter performance are evaluated. In the last Chapter the feasibility of some maneuvers using a tilting quadrotor are verified using a inverse simulation algorithm and compared with a standard configuration one. In the last section the same maneuvers are performed considering a more advanced model for the tilting quadrotor.

Chapter 2

Flexible Aircraft Model

2.1 Introduction

This section proposes a novel method for deriving simplified models of flexible aircraft dynamics by means of a mixed Newtonian-Lagrangian approach. On one side, a standard second-order matrix formulation for flexible degrees of freedom is obtained from Lagrange equations, discretizing flexible displacement and torsion variables by means of Galërkin method. [56] On the other hand the evolution of transport degrees of freedom (namely translation and attitude variables) is obtained by means of second Newton's Law and generalized Euler equations, the latter suitable for describing the dynamics of deformable bodies.

As a major advantage of the method with respect to previous (and mathematically more elegant) techniques, transport degrees of freedom are here described in terms that closely resemble classical equations of motion for rigid aircraft, thus making the engineering interpretation of the terms more intuitive. Moreover, deformation variables are approximated from the beginning of the procedure by means of a finite number of generalized coordinates. This allows for a direct derivation of a finite-order system of ordinary differential equations, without the need for passing through a hybrid system of ordinary and partial differential equations, as in Ref. [61]. At the same time, the use of a set of pseudo-body axes fixed to the undeformed aircraft structure [61] simplifies the description of its deformation, with respect to the case when mean axes are used [22, 63], as explained in more detail in the next section.

Inertial coupling terms and the effects of structural deformations on aerodynamic loads are easily highlighted in the equations of motion, and it is thus easier to drop some of them, when either numerically negligible or hardly relevant for aircraft response. A low-order, minimum complexity flexible aircraft model can thus be derived. This is a particularly interesting feature, when the dynamic model is used

for real-time simulation or control law synthesis. In the first case, computational burden is minimized, thus allowing to run the simulation software on smaller CPU's. In the second case the synthesis of the controller becomes easier, if aircraft response is described in a frequency range limited to the expected control task bandwidth. In this latter framework, the presence of unnecessary high frequency modes makes the derivation of the feedback law more demanding, possibly leading to high-order control systems that may require high performance, high bandwidth actuators for their implementation. High-order models of flexible aircraft derived by means of finite element methods, where the number of degrees of freedom reaches the order of hundreds of variables, may not suit these types of application [66].

2.2 Derivation of a Low-Order Flexible Aircraft Model

2.2.1 Transport and deformation variables

The scope of this section is to develop a minimum complexity model for the dynamics of a flexible aircraft, capturing the most relevant interactions between structural dynamics and overall vehicle motion variables. As in Ref. [61], a pseudo-body set of axes, $\mathcal{F}_B = \{O; x_B, y_B, z_B\}$ is chosen for representing position and attitude of the vehicle, where the axes are chosen like a standard set of body-axes [22] for the undeformed aircraft configuration. The origin O of the frame lies in the center of mass of the undeformed airplane, the axes x_B and z_B lying in the longitudinal plane with x_B pointing forward. The axis y_B completes a right-handed triad. The undeformed aircraft (in particular, its mass distribution, geometry and elastic properties) is assumed symmetric with respect to the longitudinal plane.

Transport degrees of freedom are represented by the position $\boldsymbol{r}_0 = (r_N, r_E, -h)^T$ of the origin O of $\mathcal{F}_B$ with respect to the surface of the Earth (assumed as flat and non-rotating [22]) and attitude of the pseudo-body axis reference frame with respect to a local vertical/local horizontal frame. Attitude is represented in terms of roll, pitch and yaw angles, $\boldsymbol{\Phi} = (\phi, \theta, \psi)^T$. The evolution of transport variables and the associated linear and angular rates is described by means of a set of 12 nonlinear ordinary differential equations of motion. Dynamic equations for deformation variables are derived using a Lagrangian formulation that, under the assumption of small flexible displacement and perfectly elastic structure response, results into a system of linear, second order ordinary differential equations, featuring a forcing term that depends on transport variables only.

Deformations cause the center of mass to move from its nominal position in the origin of the pseudo-body axes reference frame (that is, the center of mass in the undeformed configuration) together with variations of the moments of inertia. Figure

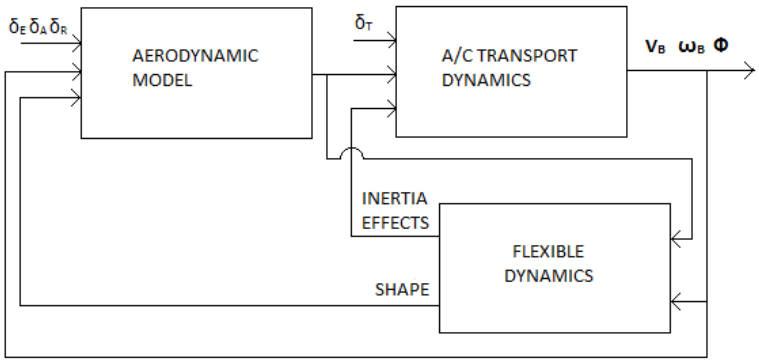

Figure 2.1: Architecture of the flexible aircraft model.

1 shows the architecture of the simulation model, where deformation of flexible parts work like a dynamic feedback for dynamics of transport variables through the aerodynamic model, whereas changes of inertial properties operate directly on it, coupling the highest order derivatives of the two sub-systems (that is, linear and angular accelerations and time-derivatives of deformation rates). Inertial effects can sometimes be negligible with respect to the variation of aerodynamic loads due to the deformation, and this assumption was at the basis of the flexible aircraft model adopted in Ref. [4], where only the effects of structural deformation on aerodynamic loads was taken into account in transport degrees of freedom, without any inertial coupling. In this work changes of inertia properties are also included in the model.

Similarly to what was done in Ref. [4], the only deformations considered are those of the two half-wings and that of the aft portion of fuselage, modeled as cantilevered beams using the Euler-Bernulli beam model. Differently from [4], the model is not a purely longitudinal one, but if features all 6 transport degrees of freedom. Deformation variables considered are bending in the z_B axis direction and torsion for the two half-wings (variables ξ_{w_L}, ξ_{w_R}, ϑ_{w_L}, and ϑ_{w_R}), and bending along the z_B and y_B axis and torsion for the aft portion of the fuselage (variables ξ_{fz}, ξ_{fy}, and ϑ_f) as represented in Fig. 2.2. Note that the two half wings are considered as independent clamped-free beams. Symmetrical and non-symmetrical deformations for the wing structure as a whole are thus obtained from the semi-sum and semi-difference of assumed mode amplitudes for the two half wings, respectively.

The choice of the set of generalized coordinates is a key point to represent the behavior of a flexible system by means of a minimum complexity model. Galërkin method [56] is here adopted to describe the deformation state of flexible elements, where deformation of each element depends on both time and a spatial variable (i.e. an abscissa counted along the deformable element, for the beam case). It is possible to approximate the evolution of the deformation by means of truncated series expansions in the form

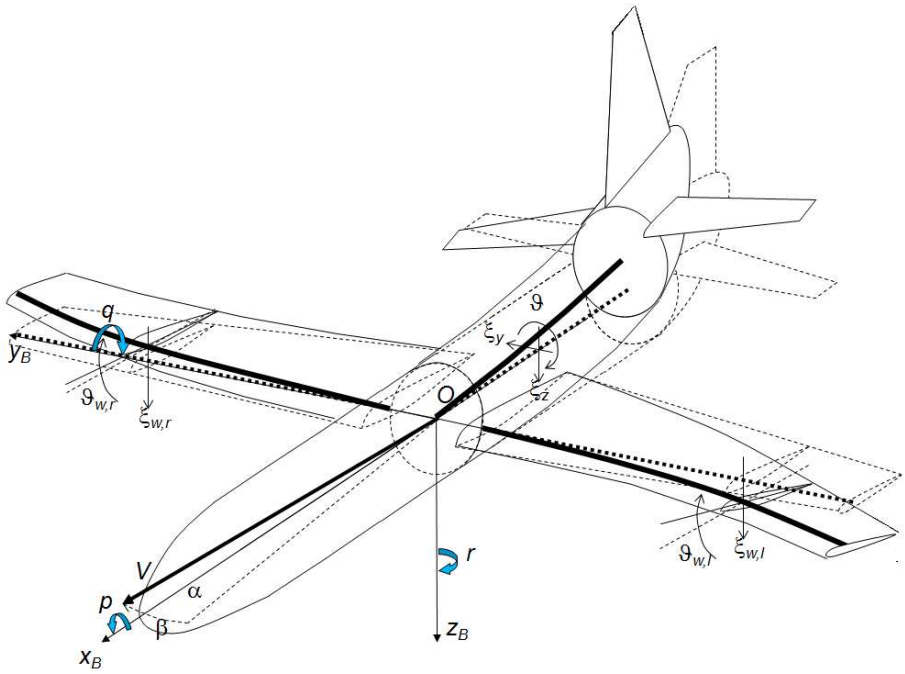

Figure 2.2: Aircraft transport and deformation variables

$$\xi_i(x_i,t) = \sum_{j=1}^{N_i} \Phi_j(x_i)\eta_j^i(t) \qquad i = f_z,f_y,w_L,w_R \tag{2.1}$$

$$\vartheta_i(x_i,t) = \sum_{j=1}^{N_i} \Psi_j(x_i)\zeta_j^i(t) \qquad i = f,w_L,w_R \tag{2.2}$$

where $\eta_j^i(t)$ and $\zeta_j^i(t)$ are amplitudes of the assumed modes represented by shape functions $\Phi_j(x_i)$ and $\Psi_j(x_i)$ for bending and for torsional degrees of freedom, respectively.

Summarizing, the state vector $\boldsymbol{x}$ of the model includes transport variables (namely position and velocity of the origin O of the pseudo–body axes frame, and attitude angles and angular velocity components of the same frame) together with generalized coordinates for bending and torsion of deformable structural elements of the aircraft, and their derivatives. The state vector can thus be partitioned as follows, $\boldsymbol{x} = (\boldsymbol{x}_V,\dot{\boldsymbol{x}}_D,\boldsymbol{x}_P,\boldsymbol{x}_D)^T$ where $\boldsymbol{x}_V = (u,v,w,p,q,r)^T$ groups velocity variables (that is, speed components and angular rates), $\boldsymbol{x}_P = (\phi,\theta,\psi,r_N,r_E,-h)^T$ groups position variables, and deformation variables are listed in the vector $\boldsymbol{x}_D = (\eta_1^z,\ldots,\eta_{n_z}^z,\ldots,\eta_1^y,\ldots,\eta_{n_y}^y,\zeta_1,\ldots,\zeta_{n_\vartheta})^T$, where n_y and n_z are the total numbers of generalized coordinates used for representing bending deformations in the y and z

directions, respectively, whereas a total of n_ϑ generalized coordinates are associated to torsion deformations of wing and fuselage.

Note that, like in conventional flight dynamics, yaw angle and position with respect to the horizontal plane (r_N and r_E) can be dropped since the beginning, together with h, if a constant air density ρ is assumed for simplicity [22]. This is not possible when a fully Lagrangian approach is adopted and all position variables need to be accounted for during the whole derivation process of the equations of motion. Decoupled variables can be dropped only *a posteriori*.

2.2.2 Translational dynamics

The equations of motion for transport variables result from the application of Newton's second law to the deformable vehicle. Under the hypothesis of flat, non-rotating Earth, the acceleration of the origin of the pseudo-body axes can be written as

$$\boldsymbol{a}_0 = \boldsymbol{a}_{CoM} - \frac{d^2\boldsymbol{r}_{CoM}}{dt^2} \tag{2.3}$$

where the acceleration of the center of mass, $\boldsymbol{a}_{CoM}$, can be expressed according to Newton's second law as the sum of external forces (thrust, aerodynamic forces and weight) divided by the total gravity. When all the vector quantities are represented in the pseudo-body axis frame, one gets

$$\dot{\boldsymbol{V}}_{0_B} + \boldsymbol{\omega}_B \times \boldsymbol{V}_{0_B} = \boldsymbol{F}/m - \ddot{\boldsymbol{r}}_{CoM_B} - 2\boldsymbol{\omega}_B \times \dot{\boldsymbol{r}}_{CoM_B} - \dot{\boldsymbol{\omega}}_B \times \boldsymbol{r}_{CoM_B} - \boldsymbol{\omega}_B \times (\boldsymbol{\omega}_B \times \boldsymbol{r}_{CoM_B}) \tag{2.4}$$

where $\boldsymbol{V}_{0_B} = (u,v,w)^T$ and $\boldsymbol{\omega}_B = (p,q,r)^T$ are linear and angular velocity components in $\mathcal{F}_B$, respectively, and the external force $\boldsymbol{F} = \boldsymbol{F}_A + \boldsymbol{F}_T + m\boldsymbol{g}_B$ is given by the sum of aerodynamic forces, thrust and weight.

The distance between the origin of the reference frame and the center of mass, $\boldsymbol{r}_{CoM}$, depends on the displacements of the flexible parts. Assuming that torsion of the deformable elements does not affect significantly the position of the center of mass, it is possible to express $\boldsymbol{r}_{CoM_B}$ as a function of the generalized coordinates $\boldsymbol{\eta} = (\dots,\eta_j^i,\dots)^T$ adopted in Eq. (2.1) for representing bending displacements. Assuming small elastic displacements for the deformable elements modeled as clamped-free beams of length ℓ_k and linear density $\mu(x_k)$, the components of

$\boldsymbol{r}_{CoM} = (x_{CoM}, y_{CoM}, z_{CoM})^T$ are

$$\begin{aligned}
x_{CoM} &= 0 \\
y_{CoM} &= \frac{1}{m}\sum_{k=1}^{N_y}\left\{\int_0^{l_k}\left[\mu(x_k)\sum_{j=1}^{N_k}\Phi_j(x_k)\eta_j^y(t)\right]dx_k + m_{tip_k}\sum_{j=1}^{N_k}\Phi_j(\ell_k)\eta_j^y(t)\right\} = \sum_{j=1}^{n_y}\Lambda_{j,y}\eta_j \\
z_{CoM} &= \frac{1}{m}\sum_{k=1}^{N_z}\left\{\int_0^{l_k}\left[\mu(x_k)\sum_{j=1}^{N_k}\Phi_j(x_k)\eta_j^z(t)\right]dx_k + m_{tip_k}\sum_{j=1}^{N_k}\Phi_j(\ell_k)\eta_j^z(t)\right\} = \sum_{j=1}^{n_z}\Lambda_{j,z}\eta_j
\end{aligned} \tag{2.5}$$

where N_y and N_z are the numbers of deformable elements that can bend in the y and z directions of $\mathcal{F}_B$, and N_k the number of assumed modes used for approximating its deformation. In the present application, no deformation in the x_B direction is present and it is $n_y = N_{f_y}$ and $n_z = N_{f_z} + N_{w_R} + N_{w_L}$. For the considered aircraft model, a tip mass m_{tip_k} is present only at the edge of the aft portion of the fuselage, that is, the assembly of horizontal and vertical tail empennages.

Equation (2.5) can be recast in matrix form as $\boldsymbol{r}_{CoM} = \boldsymbol{\Lambda}\boldsymbol{\eta}$, where the matrix

$$\boldsymbol{\Lambda} = \begin{bmatrix} 0 & \dots & \dots & \dots & \dots & 0 \\ \Lambda_{y,1} & \dots & \Lambda_{y,n_y} & 0 & \dots & 0 \\ 0 & \dots & 0 & \Lambda_{z,1} & \dots & \Lambda_{z,n_z} \end{bmatrix} \tag{2.6}$$

is constant under the hypothesis of linear, purely elastic, deformations. The equation that describes translational dynamics of the origin of $\mathcal{F}_B$ can thus be written in the form

$$\dot{\boldsymbol{V}}_{0_B} + \boldsymbol{\Lambda}\ddot{\boldsymbol{\eta}} - (\boldsymbol{\Lambda}\boldsymbol{\eta}) \times \dot{\boldsymbol{\omega}}_B = \boldsymbol{F}/m - \boldsymbol{\omega}_B \times \boldsymbol{V}_{0_B} - 2\boldsymbol{\omega}_B \times \boldsymbol{\Lambda}\dot{\boldsymbol{\eta}} - \boldsymbol{\omega}_B \times \boldsymbol{\omega}_B \times \boldsymbol{\Lambda}\boldsymbol{\eta} \tag{2.7}$$

2.2.3 Rotational dynamics

The evolution of attitude degrees of freedom of the pseudo-body reference frame can be expressed using the generalized form of angular momentum equation, expressed in the pseudo-body axis reference frame

$$\frac{d\boldsymbol{h}}{dt} + \boldsymbol{S} \times \boldsymbol{a}_0 = \boldsymbol{M} \tag{2.8}$$

where the static moment is $\boldsymbol{S} = m\boldsymbol{r}_{CoM} = m\boldsymbol{\Lambda}\boldsymbol{\eta}$ and the absolute acceleration of O expressed in $\mathcal{F}_B$ is $\boldsymbol{a}_{0_B} = \dot{\boldsymbol{V}}_{0_B} + \boldsymbol{\omega}_B \times \boldsymbol{V}_{0_B}$. When projected in terms of components in the pseudo-body axis frame, Eq. (2.8) achieves the compact form

$$\boldsymbol{I}\dot{\boldsymbol{\omega}}_B + \dot{\boldsymbol{I}}\boldsymbol{\omega}_B + \boldsymbol{\omega}_B \times (\boldsymbol{I}\boldsymbol{\omega}_B) + \dot{\boldsymbol{h}}_{rel} + \boldsymbol{\omega}_B \times \boldsymbol{h}_{rel} + m\boldsymbol{\Lambda}\boldsymbol{\eta} \times \left(\dot{\boldsymbol{V}}_{0_B} + \boldsymbol{\omega}_B \times \boldsymbol{V}_{0_B}\right) = \boldsymbol{M}_{0_B} \tag{2.9}$$

Note that, for a deformable body, the moment of inertia tensor $\boldsymbol{I}$ depends on the deformation states, that is, in the present case, on the values of $\boldsymbol{\eta}$ and, to a minor extent, $\boldsymbol{\zeta}$. As a consequence, $\boldsymbol{I}$ is no longer constant, like in the rigid-body case, and its time derivative $\dot{\boldsymbol{I}}$ shows up in the equations of motion. The inertia tensor can be written as $\boldsymbol{I} = \boldsymbol{I}_0 + \Delta\boldsymbol{I}$, where $\boldsymbol{I}_0$ is the (constant) moment of inertia for the undeformed configuration and the elements of the matrix $\Delta\boldsymbol{I}$ can be expressed as linear functions of deformation states. The expressions for $\Delta\boldsymbol{I}$ and $\dot{\boldsymbol{I}} = \Delta\dot{\boldsymbol{I}}$ are derived following an approach similar to that used in the derivation of Eq. 2.5, but the procedure is omitted for the sake of conciseness.

The term $\boldsymbol{h}_{rel}$ in Eq. (2.9) represents the contribution of the deformation rate to the relative angular momentum

$$\boldsymbol{h}_{rel} = \sum_{k=1}^{N_{def}} \left[\int_{\mathcal{B}_k} \boldsymbol{r}_{OP} \times \dot{\boldsymbol{\xi}} \delta m + \int_{\mathcal{B}_k} \delta\boldsymbol{I}(\dot{\vartheta}\hat{\boldsymbol{\tau}}_k + \dot{\boldsymbol{\xi}}') + m_{tip_k}\boldsymbol{r}_{tip} \times \dot{\boldsymbol{\xi}} + \boldsymbol{I}_{tip_k}(\dot{\vartheta}\hat{\boldsymbol{\tau}}_k + \dot{\boldsymbol{\xi}}')_{\ell_k} \right] \tag{2.10}$$

where $\boldsymbol{r}_{OP} = (x, y+\xi_y, z+\xi_z)^T$ is the position of the mass element δm in $\mathcal{F}_B$, $\delta\boldsymbol{I}$ its moment of inertia, $\dot{\boldsymbol{\xi}}$ is the deformation rate, and the relative angular rate is given by the sum of the torsion rate $\dot{\vartheta}$ around the torsion axis $\hat{\boldsymbol{\tau}}_k$ and the rotation rate $\dot{\boldsymbol{\xi}}'$ induced by bending deformations. Again, the fuselage features a tail assembly at the tip with moment of inertia $\boldsymbol{I}_{tip_k}$.

Once the approximations for the deformation variables, Eqs. (2.1)-(2.2), are substituted into the definition of $\boldsymbol{h}_{rel}$, it is possible to derive a linear expression for $\boldsymbol{h}_{rel}$ as a function of $\dot{\boldsymbol{\eta}}$ and $\dot{\boldsymbol{\theta}}$. The effect of torsion rate is usually smaller than that of bending and it can be omitted. In such a case one gets

$$\boldsymbol{h}_{rel} = \boldsymbol{\Gamma}\dot{\boldsymbol{\eta}}$$

Also in this case, the expressions of the elements of $\boldsymbol{\Gamma}$ depend on shape functions, and the derivation is omitted for the sake of conciseness. The final expression for rotational variable dynamics is given by

$$\boldsymbol{I}\dot{\boldsymbol{\omega}}_B + \boldsymbol{\Gamma}\ddot{\boldsymbol{\eta}} + (m\boldsymbol{\Lambda}\boldsymbol{\eta}) \times \dot{\boldsymbol{V}}_{0_B} = \boldsymbol{M}_{0_B} - \dot{\boldsymbol{I}}\boldsymbol{\omega}_B - \boldsymbol{\omega}_B \times (\boldsymbol{I}\boldsymbol{\omega}_B) + (\boldsymbol{\Gamma}\boldsymbol{\eta}) \times \boldsymbol{\omega}_B - m(\boldsymbol{\Lambda}\boldsymbol{\eta}) \times (\boldsymbol{\omega}_B \times \boldsymbol{V}_{0_B}) \tag{2.11}$$

2.2.4 Kinematic equations

The evolution of transport variables is ruled by kinematic equations, their rate of variation being expressed as a function of linear and angular velocity components. The derivative of the position of the origin of $\mathcal{F}_B$ is simply given by

$$\dot{\boldsymbol{r}}_I = \boldsymbol{T}_{IB}(\phi, \theta, \psi)\boldsymbol{V}_{B_0} \tag{2.12}$$

where $\boldsymbol{T}_{IB}$ is the coordinate transformation matrix from pseudo-body to inertial frame, that depends on Euler angles [22]. Euler angle rates depend on angular velocity components as [22]

$$\begin{aligned} \dot{\phi} &= p + (q\sin\phi + r\cos\phi)\tan\theta \\ \dot{\theta} &= q\cos\phi - r\sin\phi \\ \dot{\psi} &= (q\sin\phi + r\cos\phi)/\cos\theta \end{aligned} \tag{2.13}$$

2.2.5 Aerodynamic model

Strip theory is used for the determination of aerodynamic force and moment components. This method has the great advantage of simplicity and limited computational effort, because it describes the aerodynamic loads as a function of the direction of the local flow only, thus avoiding unnecessary complexity in the aerodynamic model. This is possible in all those cases where the analysis is focused on piloting task (bandwidths below 2 Hz) and aeroelastic coupling between unsteady aerodynamics and higher frequency structural dynamics is not accounted for.

The wing is divided in spanwise elements, where properties of each section are assumed uniform and aerodynamic forces and moments are evaluated from the local two-dimensional flow. Lift, drag and aerodynamic moment are thus determined for each element as a function of the local angle of attack only, independently of the angle of attack at any other station. Integrating aerodynamic loads over the wing span the total aerodynamic load generated by the wing is obtained. A similar approach is used for fuselage elements and horizontal and vertical tail surfaces. Note that aerodynamic loads will depend also on deformation rate, inasmuch as this will affect the local direction of the flow.

2.2.6 Deformation variable dynamics

The equations of motion of flexible dynamics are derived using the Lagrangian approach after the elastic displacements has been represented by means of a finite number of generalized coordinates. This method can easily accommodate any desired level of complexity in the representation of elastic degrees of freedom, from low frequency, fundamental ones up to high frequency modes.

Lagrange's equation is given in general by [59]

$$\frac{d}{dt}\frac{\partial \mathcal{L}}{\partial \dot{\boldsymbol{q}}} - \frac{\partial \mathcal{L}}{\partial \boldsymbol{q}} = \boldsymbol{Q} \tag{2.14}$$

where the Lagrangian $\mathcal{L} = \mathcal{T} - \mathcal{U}$ is defined as the difference between kinetic ($\mathcal{T}$) and potential energy ($\mathcal{U}$), and $\boldsymbol{q}$ is a vector of generalized variables. In the present case

the vector of generalized variables is represented by the amplitude of the assumed modes in the expansions of flexible degrees of freedom provided by Eqs. (2.1) and (2.2). For flexible dynamics, Lagrange equation can be written in compact form as

$$\frac{d}{dt}\left(\frac{\partial \mathcal{T}}{\partial \dot{\boldsymbol{q}}}\right) - \frac{\partial \mathcal{T}}{\partial \boldsymbol{q}} + \frac{\partial \mathcal{U}}{\partial \boldsymbol{q}} = \boldsymbol{Q} \tag{2.15}$$

The total kinetic energy of the system is defined as the sum of kinetic energy of different parts, namely, fore fuselage, considered as rigid, aft fuselage (where the tail assembly is modeled as a tip mass) and two half-wings. The kinetic energy of the whole body is given by

$$\mathcal{T} = \frac{1}{2}\int_{\mathcal{B}} \boldsymbol{V}_P^T \boldsymbol{V}_P \delta m + \int_{\mathcal{B}} \boldsymbol{\Omega}_P^T \delta \boldsymbol{I} \boldsymbol{\Omega}_P \tag{2.16}$$

where $\boldsymbol{V}_P$ represents the local speed of the generic point, $\boldsymbol{\Omega}_P$ is the angular speed for both rigid and flexible parts and $\delta \boldsymbol{I}$ is the inertia tensor of the structure element. In general, $\boldsymbol{V}_P$ and $\boldsymbol{\Omega}_P$ are expressed as

$$\begin{aligned} \boldsymbol{V}_P &= \boldsymbol{V}_0 + \boldsymbol{\omega}_B \times \boldsymbol{r}_{OP} + \dot{\boldsymbol{\xi}}(x_P,t) \\ \boldsymbol{\Omega}_P &= \boldsymbol{\omega} + \dot{\vartheta}(x_P,t)\hat{\boldsymbol{\tau}}_P + \dot{\boldsymbol{\xi}}'(x_P,t) \end{aligned}$$

For rigid elements the terms $\dot{\boldsymbol{\xi}}$, $\dot{\vartheta}$ and $\dot{\boldsymbol{\xi}}'$ vanish (*e.g.* for the forward portion of the fuselage and the tail empennages, in the example model considered in the next section).

The potential energy can be written as the sum of the elastic energy of the system flexible parts plus gravitational potential,

$$\mathcal{U} = \mathcal{U}_f + \mathcal{U}_{w_L} + \mathcal{U}_{w_R} + mgh_{CoM}$$

where h_G is the vertical displacement of the center of mass CoM. Provided that altitude variations are several orders of magnitude larger than center of mass displacement from the origin O of the pseudo-body axes frame, it is possible to assume $h_{CoM} \approx h_O$. In this way, the latter term is not affected by deformation variables and it can be dropped.

For the flexible elements, the strain energy can be expressed as

$$\mathcal{U}_f = \frac{1}{2}\int_0^{l_f} \left[(EI_y)_f \left(\xi''_{f_z}\right)^2 + (EI_z)_f \left(\xi''_{f_y}\right)^2 + (GJ_t)_f \left(\vartheta'_f\right)^2 \right] dx_f \tag{2.17}$$

for the aft portion of the fuselage, that can bend in the y and z directions, whereas if is

$$\mathcal{U}_{w_X} = \frac{1}{2}\int_0^{l_w} \left[(EI)_w \left(\xi''_{w_X}\right)^2 + (GJ_t)_{w_X} \left(\vartheta'_{w_X}\right)^2 \right] dx_w \ , \quad X = L,\, R \tag{2.18}$$

for the two half-wings, for which the only bending deformation considered is in the direction normal to the wing planform.

2.2.7 Forces acting on the deformable elements

Generalized forces $\boldsymbol{Q}$, on the right-hand side of the Lagrangian equations, can be derived through the principle of virtual works. For each flexible part the virtual work can be expressed as a function of external forces that act on it (i.e. aerodynamic distributed and concentrated loads) multiplied by the virtual displacements

$$\delta W_i = \int_{\mathcal{B}} f^i_{ext} \delta\xi_i \qquad i = w_L, w_R, f_y, f_z \tag{2.19}$$

The aerodynamic load on each section of the two half-wings is a function of the local angle of attack, which is given by the sum of aircraft angle of attack, α_{WB}, wing twist angle i_w, roll and pitch rates, p and q, bending rate $\dot{\xi}$, torsion angle ϑ and its time derivative, $\dot{\vartheta}$. Aerodynamic force and moment acting on the wing section are thus given by

$$\begin{aligned} f_{Aw} &= \frac{1}{2}\rho S U^2 C_{L\alpha}\left[\alpha_{WB} + i_W(x_w) + \frac{p y_w - q x_w}{U} + \frac{\dot{\xi}}{U} + \vartheta + \frac{\dot{\vartheta}(x_\vartheta - x_{CA})}{U}\right] \\ M_{Aw} &= \frac{1}{2}\rho S U^2 C_{L\alpha}(x_\vartheta - x_{CA})\left[\alpha_{WB} + i_W(x_w) + \frac{p y_w - q x_w}{U} + \frac{\dot{\xi}}{U} + \vartheta + \frac{\dot{\vartheta}(x_\vartheta - x_{CA})}{U}\right] \end{aligned} \tag{2.20}$$

where x_w and y_w are the coordinates of the wing section aerodynamic center in $\mathcal{F}_B$ and $x_\vartheta - x_{CA}$ is the distance between the torsion center and the airfoil aerodynamic center.

External aerodynamic force and moment can be written in the form

$$\begin{aligned} f_A(x) &= f_{A_0} + \frac{\partial f_A}{\delta\dot{\xi}}\dot{\xi} \\ M_A(x) &= M_{A_0} + \frac{\partial M_A}{\delta\dot{\vartheta}}\dot{\vartheta} \end{aligned} \tag{2.21}$$

where the subscript 0 indicates the aerodynamic load generated by the "frozen" configuration, for the current values of transport and deformation variables, whereas the second term indicates the increment generated by deformation rates. The virtual work of aerodynamic forces acting on the k-th deformable element can thus be expressed as

$$\begin{aligned} \delta W_{k,b} &= \int_0^{\ell_k} (f_A \delta\xi) dx_k = \int_0^{\ell_k} (f_{A_0}\delta\xi) dx_k + \int_0^{\ell_k} \left(\frac{\partial f_A}{\delta\dot{\xi}}\dot{\xi}\right)\delta\xi dx_k \\ \delta W_{k,t} &= \int_0^{\ell_k} (M_A \delta\vartheta) dx_k = \int_0^{\ell_k} (M_{A_0}\delta\vartheta) dx_k + \int_0^{\ell_k} \left(\frac{\partial M_A}{\delta\dot{\vartheta}}\dot{\vartheta}\right)\delta\vartheta dx_k \end{aligned} \tag{2.22}$$

Generalized forces $\boldsymbol{Q}_{A_0}$ associated to the "frozen" term of the aerodynamic load, $\boldsymbol{f}_{A_0}$, are determined by the projection of the local aerodynamic load on the assumed

modes. The increment induced by deformation rates can be expressed in terms of a Rayleigh dissipation function [45, 59]. Considering the k-th deformable element, it is

$$\int_0^{\ell_k} \left(\frac{\partial f_A}{\delta \dot{\xi}} \dot{\xi} \right) \delta\xi dx_k = \sum_{j=1}^{N} \frac{\partial F_b^{(k)}}{\partial \dot{\eta}_j} \delta\eta_j \quad ; \quad \int_0^{\ell_k} \left(\frac{\partial M_A}{\delta \dot{\vartheta}} \dot{\vartheta} \right) \delta\vartheta dx_k = \sum_{j=1}^{N} \frac{\partial F_t^{(k)}}{\partial \dot{\zeta}_j} \delta\zeta_j \tag{2.23}$$

(2.24)

where $F_b^{(k)}$ and $F_t^{(k)}$ are defined as

$$F_b^{(k)} = \frac{1}{2} \int_0^{\ell_k} \frac{\partial f_A}{\delta \dot{\xi}} \dot{\xi}^2 dx_k \quad ; \quad F_t^{(k)} = \frac{1}{2} \int_0^{\ell_k} \frac{\partial M_A}{\delta \dot{\vartheta}} \dot{\vartheta}^2 dx_k \tag{2.25}$$

Both terms in the definition of the dissipation function can be recast in a quadratic form as

$$F_b^{(k)} = \dot{\boldsymbol{\eta}}^T \boldsymbol{C}_b^{(k)} \dot{\boldsymbol{\eta}} \; ; \quad F_t^{(k)} = \dot{\boldsymbol{\zeta}}^T \boldsymbol{C}_t^{(k)} \dot{\boldsymbol{\zeta}}$$

where the elements of the positive definite matrices $\boldsymbol{C}_b^{(k)}$ and $\boldsymbol{C}_t^{(k)}$ are given by

$$(C_b)_{i,j}^k = \frac{1}{2} \int_0^{l_k} \frac{\partial f_{Ak}}{\partial \dot{\xi}_k} \Phi_i(x_k) \Phi_j(x_k) dx_k \tag{2.26}$$

$$(C_t)_{i,j}^k = \frac{1}{2} \int_0^{l_k} \frac{\partial M_{Ak}}{\partial \dot{\vartheta}_k} \Psi_i(x_k) \Psi_j(x_k) dx_k \tag{2.27}$$

where the subscript b is related to bending and t is related to torsion.

2.2.8 Tail surfaces

Fuselage is assumed for simplicity as a non-lifting body, so that its deformation is induced by the aerodynamic loads acting on the horizontal and vertical tail empennages. These loads are assumed as concentrated at the tip of the deformable element. The angle of attack of the horizontal tail, α_H, depends on transport and deformation variables,

$$\alpha_H = \alpha_{WB} + i_H + \xi'_{f_z}(\ell_f,t) + \frac{\dot{\xi}(\ell_f,t)}{U} - \frac{q\ell_H}{U} \tag{2.28}$$

where i_H is horizontal tail incidence, $\xi'_{f_z} = \partial \xi_{f_z} / \partial x_f$ is the rotation of fuselage tip due to bending in the z direction, $\dot{\xi}(\ell_f,t)$ is its deformation rate and ℓ_H is the distance between horizontal tail aerodynamic center and aircraft center of mass. The magnitude of the aerodynamic force acting on the horizontal tail surface is then given by

$$f_{A_h} = \frac{1}{2} \rho S_H U^2 C_{L\alpha_H} \alpha_H \tag{2.29}$$

In the $\mathcal{F}_B$ frame the resulting components are $\left[\boldsymbol{f}_{A_h}\right]_B = f_{A_h}(\sin(\alpha_H - i_H),0, -\cos(\alpha_H - i_H))^T$.

Similarly, the local sideslip angle evaluated at the fuselage tip, equal to the angle of attack of the vertical tail surface, is given by

$$\beta_V = \beta_{WB} + \xi'_{f_y} + \frac{pz_P - ry_P}{2U} + \frac{\dot{\vartheta}_f z_P}{U} \tag{2.30}$$

where $\xi'_{f_y} = \partial\xi_{f_z}/\partial x_f$ is the rotation of the terminal fuselage section around the z axis due to fuselage bending out of the longitudinal plane, and (y_P,z_P) is the position of the vertical tail aerodynamic center on a plane perpendicular to the fuselage axis. Given the above definitions, the vertical fin generates a lateral aerodynamic load and a torsion moment,

$$f_{Af_y} = \frac{1}{2}\rho S_V U^2 C_{Y\beta_f}\beta_V \tag{2.31}$$

$$M_{Af_z} = \frac{1}{2}\rho S_V U^2 C_{Y\beta_f}\beta_V z_p \tag{2.32}$$

Tail surfaces generate contributions to both global and local aerodynamic loads, to be accounted for in the definition of force and moments driving transport variable dynamics as well as increments to the virtual work $\delta\mathcal{W}$, that provides the generalized forces for the equations of motion of deformation variables. The derivation of these terms, performed in a way similar to the approach discussed above for aerodynamic loads acting on a wing section, is omitted.

2.2.9 Equation of motion for deformation variables

Once all the terms considered in the previous subsections are expressed in terms of generalized coordinates for the amplitude of the assumed modes, flexible dynamics achieves the form

$$\boldsymbol{M}\ddot{\boldsymbol{x}}_D + \boldsymbol{M}_C\dot{\boldsymbol{x}}_V = -\boldsymbol{C}\dot{\boldsymbol{x}}_D - \boldsymbol{K}\boldsymbol{x}_D + \boldsymbol{Q}_{A_0}(\boldsymbol{x}_V,\boldsymbol{x}_P,\boldsymbol{x}_D) + \boldsymbol{f}_{in}(\boldsymbol{x}_V) \tag{2.33}$$

where $\boldsymbol{M}$ is a mass matrix, $\boldsymbol{M}_C$ is the matrix of inertial coupling terms with transport variables, generated by the term $\partial(\partial\mathcal{T}/\partial\dot{\boldsymbol{q}})/\partial t$ in Lagrange's equation, $\boldsymbol{C}$ is the damping matrix, introduced by the dissipative aerodynamic terms, $\boldsymbol{K}$ is the stiffness matrix, $\boldsymbol{Q}_{A_0}$ is a vector of generalized aerodynamic forces, and, finally, $\boldsymbol{f}_{in}(\boldsymbol{x}_V)$ collects the inertia terms related to current values of transport velocity variables. Mass, damping and stiffness matrices are all properly partitioned.

2.2.10 Complete flexible aircraft model

Considering Eq. (2.7), (2.11), (2.12), (2.13) and (2.33), the complete system of equations can be expressed in the following compact form:

$$\boldsymbol{A}(\boldsymbol{x})\dot{\boldsymbol{x}} = \boldsymbol{b}(\boldsymbol{x},\boldsymbol{u}) \tag{2.34}$$

where $\boldsymbol{A}(\boldsymbol{x})$ is the matrix of the coupling terms. Some of the coefficients of $\boldsymbol{M}$ depend on the state vector $\boldsymbol{x}$, so that, in general, it is not constant in time. In particular, there are coupling terms in the dynamics of transport variables that depend on center of mass displacement. As a consequence, the matrix $\boldsymbol{A}$ needs to be calculated at every time step and its inverse evaluated in order to obtain an explicit formulation for the equations of motion, suitable for numerical integration.

The matrix $\boldsymbol{A}$ is partitioned as follows

$$\boldsymbol{A} = \begin{bmatrix} \tilde{\boldsymbol{A}} & \boldsymbol{0} \\ \boldsymbol{0} & \boldsymbol{I} \end{bmatrix}$$

with

$$\tilde{\boldsymbol{A}} = \begin{bmatrix} \boldsymbol{A}_{rig} & \boldsymbol{A}_{f2r} \\ \boldsymbol{A}_{r2f} & \boldsymbol{A}_{flex} \end{bmatrix}$$

where $\boldsymbol{A}_{rig}$ is the inertial coupling matrix between transport degrees of freedom, $\boldsymbol{A}_{flex} = \boldsymbol{M}$ is the mass matrix, while $\boldsymbol{A}_{f2r}$ and $\boldsymbol{A}_{r2f}$ are the inertial coupling matrices between transport and deformation variables.

If the displacement of the center of mass, $\boldsymbol{\Lambda\eta}$, remains small and terms such as $\boldsymbol{\Lambda\eta} \times \dot{\boldsymbol{\omega}}$ and $\boldsymbol{\Lambda\eta} \times \dot{\boldsymbol{V}}_{0_B}$ in Eqs. (7) and (11) become negligible, than the coupling matrix $\tilde{\boldsymbol{A}}$ becomes independent of the current state and it can be evaluated once, before numerically integrating the equations of motion. When possible, this simplification saves a significant amount of computational time.

Chapter 3

Rotorcraft Mathematical Models

3.1 Levels of Rotorcraft Modeling

The mathematical modeling of rotorcraft is not an easy task, because usually different elements that have coupled non–linear dynamics should be analyzed. Considering conventional helicopters, which main components are shown in Fig. 3.1, each element can be described by means of models that use different levels of complexity. Padfield [65] proposed a classification based on the complexity of rotor models for simulation. This classification has been later modified by Torasso [89] adding a lower level of modelization. The complete classification is shown in table 3.1.

Level 0 can be used for the study of preliminary configurations, giving a relation between design parameters, vehicle characteristics, and expected performances. Level 1 models are used to determine parametric trends for flying qualities and performance studies well within operational flight envelope, as well as design of low bandwidth control. Level 2 models are used for the study of the whole flight envelope, and for the design of medium bandwidth of control tasks. Finally level 3 models are use for the vibration analysis, for the rotor design and analysis, and for the study of the safe flight envelope.

One of the goal of this work is to provide a level 0/1 model that can take into account some of the higher complexity effects, like those in level 2 models, but considering a simplified approach, suitable for the preliminary study or the implementation of control algorithm, like the inverse simulation approach.

In the last section of this chapter two simplified model for quadrotors are derived, one for the standard configuration and the second for a tilting rotor one.

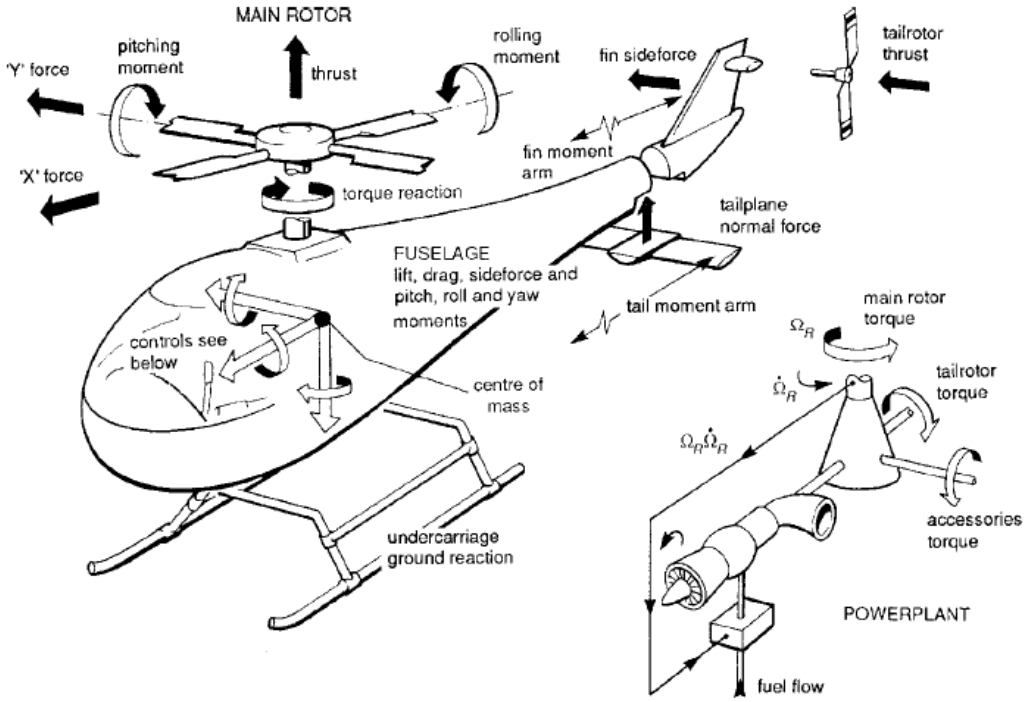

Figure 3.1: Interacting main subsystems of an helicopter [65].

3.2 Helicopter Equations of Motion

In this work an articulated rotor will be taken into account and, in particular, the characteristics considered will be those of a UH–60A main rotor. This is because the details and configurations of this helicopter are easily available in literature [39]. The flap and lag hinge axes of this rotor are coincident, but the model can be easily modified in order to describe a different set of hinges or a hingeless rotor.

The equation of motion for an helicopter, written using a Newtonian approach and written in the body–fixed coordinate system are as follow:

$$m\left(\dot{\boldsymbol{v}}_B + \boldsymbol{\omega}_B \times \boldsymbol{v}_b\right) = \boldsymbol{F}_B \tag{3.1}$$

$$\boldsymbol{I}\dot{\boldsymbol{\omega}}_B + \boldsymbol{\omega}_B \times (\boldsymbol{I}\boldsymbol{\omega}_B) = \boldsymbol{M}_B \tag{3.2}$$

where $\boldsymbol{F}_B$ and $\boldsymbol{M}_B$ are the external forces and moments. This can be divided in contributions by the main rotor loads, fuselage aerodynamic loads, horizontal and vertical tail aerodynamic loads, tail rotor loads, and weight. In this section a brief description of the equations of motions of the different components are presented, while detail of complete derivation can be found in Appendix B, as the definition of the reference frames and their transformation are in Appendix A.

Table 3.1: Levels of rotor modeling ([65], [89])

Level 0	Aerodynamics	linear airfoil aerodynamics
		static uniform inflow with momentum theory
		analytically averaged aerodynamic loads
	Dynamics	rigid blades featuring
		steady–state flapping motion
		described in terms of multi blade coordinates
Level 1	Aerodynamics	linear 2-D dynamic inflow
		local momentum theory
		analytically integrated loads
	Dynamics	rigid blades:
		quasi–steady motion
		3 DoF flap
		6 DoF flap + lag
		6 DoF flap + lag + quasi–steady torsion
Level 2	Aerodynamics	nonlinear (limited 3-D) dynamic inflow
		local momentum theory
		local effects of blade vortex interaction
		unsteady 2-D compressibility
		numerically integrated loads
	Dynamics	rigid blades with options as in Level 1
		limited number of blade elastic modes
Level 3	Aerodynamics	nonlinear 3-D full wake
		analysis (free or prescribed) unsteady
		2–D compressibility
		numerically integrated loads
	Dynamics	detailed structural representation
		as elastic modes
		or finite elements

3.2.1 Main Rotor

The main rotor is the most important component of the helicopter, because it provides most of forces and moments that control the vehicle. As a matter of fact the dynamic of the main rotor influence greatly the overall response of the helicopter, and for this reason it is very important the model used for its description. In section 3.3 the mathematical model used to describe the rotor dynamics is shown, while in section 3.4 the unsteady aerodynamic model used for the determination of the aerodynamic loads is described. The model used for the description of the unsteady

aerodynamic is not alternative to the CFD analysis, but rather a reduced order model, that can be used in flight simulation or during preliminary design.

For this work the rotor states equation of motion are derived for individual blade model, so that the vector of states is:

$$\begin{aligned} \boldsymbol{x}_r &= \Big(\beta_i,\ldots,\beta_{N_b},\dot{\beta}_i,\ldots,\dot{\beta}_{N_{BL}}, \\ &\quad \zeta_i,\ldots,\zeta_{N_{BL}},\dot{\zeta}_i,\ldots,\dot{\zeta}_{N_{BL}},\varphi_i,\ldots,\varphi_{N_{BL}},\dot{\varphi}_i,\ldots,\dot{\varphi}_{N_{BL}}\Big)^T \end{aligned} \tag{3.3}$$

In addition to those the aerodynamic states should be considered, thus the dynamic inflow and the dynamic stall states.

3.2.2 Fuselage

The methods used to determine the fuselage aerodynamic forces and moments in flight dynamics applications use some simplifications in order to be comparable to the wind tunnel tests or CFD results. In the simpler models the fuselage drag is calculated using an equivalent parasite area, and the dependency on the act of motion is given only by the flow speed. More complex approaches describe the forces and moments as a function of the fuselage angle of attack and sideslip. The relationship can be expressed as polynomial interpolating functions [82] or tables [39]. The use of polynomial can be faster, but in this work the lookup table for a set of data implemented for [89] was used, as it allow the representation of some local behavior and guarantee greater accuracy. Most of the database was taken from [39] and [34], and for the flight conditions for which data were not available they were deduced on the basis of empirical considerations [79] or other publications [96]– [65]. The final forces and moments are written as a function of the coefficients evaluated as explained:

$$\boldsymbol{F}_F = \frac{1}{2}\rho \boldsymbol{V}_F^2 S_{ref} \begin{bmatrix} C_{A,x_F}(\alpha_F,\beta_F) \\ C_{A,y_F}(\alpha_F,\beta_F) \\ C_{A,z_F}(\alpha_F,\beta_F) \end{bmatrix} \tag{3.4}$$

$$\boldsymbol{M}_F = \frac{1}{2}\rho \boldsymbol{V}_F^2 S_{ref}\ell_{ref} \begin{bmatrix} C_{A,l_F}(\alpha_F,\beta_F) \\ C_{A,m_F}(\alpha_F,\beta_F) \\ C_{A,n_F}(\alpha_F,\beta_F) \end{bmatrix} + \boldsymbol{r}_B^F \times \boldsymbol{F}_F \tag{3.5}$$

3.2.3 Tail Rotor

The tail rotor can be described using the main rotor models, but the level of detail required is generally lower. There are many simpler models available, some are based on Bailey coefficient [39]– [48], others use tip path plane models [82], and some use data from wind–tunnel tests.

The most challenging part in the description of tail rotor is the evaluation of the rotor and fuselage downwash effect. This effect is rather complex and furthermore the tilt rotor is affected only in limited speed range, so that this interaction is usually evaluated using lookup tables as function of the advance ratio, rotor skew angle, and tip path plane tilt.

In this work tail rotor forces and moments are computed using the momentum theory, as described in [42], as a function of the collective command θ_{0tr}.

3.2.4 Empennage

In the considered configuration of helicopter there are both vertical and horizontal tail, so that yaw and longitudinal stability are improved.

The horizontal tail is modeled as a finite wing, thus lift and drag are given in the classical form:

$$L_{HT} = \frac{1}{2}\rho V_{HT}^2 S_{HT} C_L(\alpha_{HT}) \tag{3.6}$$

$$D_{HT} = \frac{1}{2}\rho V_{HT}^2 S_{HT} C_D(\alpha_{HT}) \tag{3.7}$$

C_L and C_D evaluated from wind–tunnel tests or CFD simulations. The effects of main rotor and fuselage influence greatly and in a complex way the angle of attack and the flow speed on the horizontal tail, as for the tail rotor. For the helicopter model considered it is possible to find in literature wind–tunnel and CFD data that describe precisely this effect, so that the airspeed can be evaluated as

$$\boldsymbol{V}_{HT} = \left(\boldsymbol{v}_B + \boldsymbol{\omega}_B \times \boldsymbol{r}_B^{HT}\right) k_{HT} + \boldsymbol{v}_{\lambda HT} \tag{3.8}$$

where $\boldsymbol{v}_{\lambda HT}$ collects the influence of the rotor and fuselage wake, while k_{HT} is a factor that account for the loss of dynamic pressure.

Considering the vertical tail the same approach can be used, paying attention that the lift and drag coefficient will be function of the sideslip rather than the angle of attack.

3.3 Main Rotor Model

The following assumptions were made for the development of the model, as in [89]:

- rotor blades are assumed rigid in flap and lag direction
- blade mass is assumed to be concentrated along the blade span axes
- blade torsional degree of freedom is modeled empirically as a dynamic twist affecting independently each blade

- aerodynamic moments developed by the airfoil around the blade pitch axis are neglected
- flap and lag hinges are assumed to be coincident, with the flap rotation following the lag rotation in sequence
- no pitch–flap coupling K_{PC} is included
- the weight of the blade is assumed as negligible, and it would be not included in the flap and lag equation of motion

Considering the evaluation of aerodynamic loads two models will be compared. The baseline model is the same as in [89] and the only unsteady effect considered is the dynamic inflow, while the second one take into account also the effect of unsteady aerodynamic and dynamic stall.

The motion of the generic blade elements is obviously related to the motion of the complete helicopter. Given the motion of the helicopter as linear and angular velocities, $\boldsymbol{v}_B = (u_B,v_B,w_B)^T$ and $\boldsymbol{\omega}_B = (p_B,q_B,r_B)^T$ respectively, it is possible to obtain the motion of the blade elements using a series of rotation from one reference frame to another. The complete evaluation for the linear and angular speed in the blade span reference frame will be given in Appendix B, nevertheless the linear speed in the blade reference frame is given by:

$$\boldsymbol{v}'_{BL} = \boldsymbol{L}_{BL,R}\left(\boldsymbol{v}_R + \boldsymbol{\omega}_R \times \boldsymbol{r}_R^{R,BL} + \dot{\boldsymbol{r}}_R^{R,BL}\right) \tag{3.9}$$

The speed of the blade with respect to the surrounding air should include the effects given by the inflow. The inflow model used for the evaluation of the aerodynamic loads is described in section 3.4.2. Anyhow calling $U_{R\lambda}$ and $U_{P\lambda}$ the speed components obtained along the y and z direction respectively, then

$$\boldsymbol{v}_{BL} = U'_T\boldsymbol{i}_{BL} + (U'_R + U_{R\lambda})\boldsymbol{j}_{BL} + (U'_P + U_{P\lambda})\boldsymbol{k}_{BL} \tag{3.10}$$

$$= U_T\boldsymbol{i}_{BL} + U_R\boldsymbol{j}_{BL} + U_P\boldsymbol{k}_{BL} \tag{3.11}$$

The angle of attack of the blade element is then defined as

$$\alpha = \theta_G + \tan^{-1}\frac{U_P}{U_T} \tag{3.12}$$

where the geometric pitch is given by the commands, the blade twist, and the dynamic twist:

$$\theta_G = \theta_0 + A_{1s}\cos\psi + B_{1s}\sin\psi\theta_{TW} + \theta_{DT} \tag{3.13}$$

The blade twist is a geometric non–linear function of the blade element radial position that can be found using lookup table. The dynamic twist is also a non–linear

function of the radial position, that can be described by a second order dynamical system, using generalized coordinate (φ_1 and φ_2). The complete dissertation about the dynamic twist can be found in Appendix B. The aerodynamic loads are a function of the angle of attack, calculated for $N_S = 5$ section of the blade. In the baseline model a lookup table that contains the lift and drag coefficients as a function of angle of attack and Mach number is used, while the evaluation considering unsteady aerodynamics is explained in detail in the next section.

The inertia forces can be found using the expression of the blade element acceleration in non–rotating frame (derived from 3.9) substituted in

$$F_{I,x_S} = \int_e^R \rho_{BL} a_{S,x} dr \tag{3.14}$$

$$F_{I,y_S} = \int_e^R \rho_{BL} a_{S,y} dr \tag{3.15}$$

$$F_{I,z_S} = \int_e^R \rho_{BL} a_{S,z} dr \tag{3.16}$$

It is evident that from the expressions above highest order derivative states would appear. It is thus more convenient to group this terms in order to obtain an expression of the form

$$\boldsymbol{M}_{FI}\dot{\boldsymbol{x}}_C = \boldsymbol{f}_{FI} \tag{3.17}$$

where $\boldsymbol{x}_C$ is the vector of coupled velocity variables $\boldsymbol{x}_C = \Big(u_B,v_B,w_B,p_B,q_B,r_B,$ $\dot{\beta}_1,\ldots,\dot{\beta}_{N_{BL}},\dot{\zeta}_i,\ldots,\dot{\zeta}_{N_{BL}}\Big)^T$. Inertial moments are generated by the inertial forces:

$$\boldsymbol{M}_{IS} = \boldsymbol{r}_S^e \times \boldsymbol{F}_{IS} \tag{3.18}$$

In a similar fashion this equation can be rearranged in order to obtain one of the form

$$\boldsymbol{M}_{MI}\dot{\boldsymbol{x}}_C = \boldsymbol{f}_{MI} \tag{3.19}$$

The system obtained is composed by six equations for 14 variables. In order to close the problem is necessary to add the flap and lag dynamic equations. The equations follow the approach proposed in Refs. [39]– [48], thus the sum of the moments applied to the hinges, that is aerodynamic, inertial, hinge spring, and lag damper moments, must be equal to zero. The final form that can be obtained is

$$\boldsymbol{M}_{\beta}\dot{\boldsymbol{x}}_C = \boldsymbol{f}_{\beta} \tag{3.20}$$

$$\boldsymbol{M}_{\zeta}\dot{\boldsymbol{x}}_C = \boldsymbol{f}_{\zeta} \tag{3.21}$$

The dynamic of the rotor is dependent on the dynamic of the overall helicopter due to the coupled variables, so that the set of variables that describe its dynamic are

$$\boldsymbol{x} = \Big(u_B,v_B,w_B,p_B,q_B,r_B,\beta_i,\ldots,\beta_{N_b},\dot{\beta}_i, \ldots,\dot{\beta}_{N_{BL}},\zeta_i,\ldots,\zeta_{N_{BL}},\dot{\zeta}_i,\ldots,\dot{\zeta}_{N_{BL}},\varphi_i,\ldots,\varphi_{N_{BL}},\dot{\varphi}_i,\ldots,\dot{\varphi}_{N_{BL}}\Big)^T \quad (3.22)$$

3.4 Unsteady Aerodynamics

3.4.1 Extended thin airfoil theory

Consider a thin airfoil that moves through a mass of still air, like the one presented in fig. 3.2 [75]. The coordinate system is located in the mid chord. The motion of the air, as seen from the coordinate system, is described by the horizontal speed u_0, the vertical speed v_0, and the rotation v_1 along the z axis.

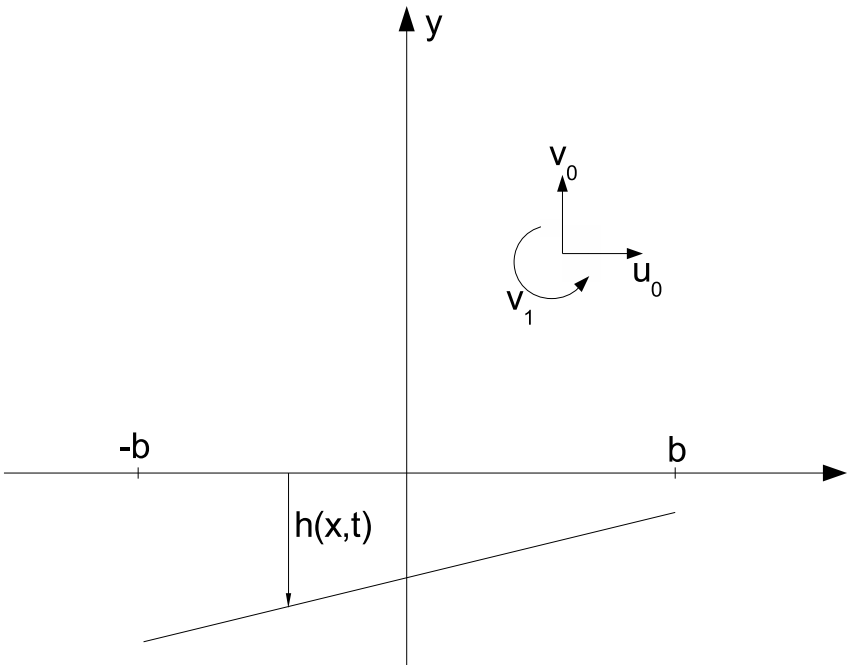

Figure 3.2: Geometry of the airfoil.

Circulation is assumed to be shed along the x axis. As in classical thin airfoil

theory it is possible to apply the non–penetration boundary condition:

$$w = \bar{v} + \lambda = u_0 \frac{\delta h}{\delta x} + \frac{\delta h}{\delta t} + v_0 + v_1 \frac{x}{b} \tag{3.23}$$

where w is the total induced flow, λ is the induced flow from the shed circulation, h are the displacements, and $\bar{v}$ is the induced inflow from bound circulation. From the Biot–Savart law $\bar{v}$ and λ can be expressed as a function of the bound circulation for unit length γ_b and wake circulation γ_w respectively (see [75]– [49])

$$\bar{v} = -\frac{1}{2\pi} \int_{-b}^{+b} \frac{\gamma_b(\chi,t)}{x-\chi} d\chi \tag{3.24}$$

$$\lambda = -\frac{1}{2\pi} \int_{+b}^{+\infty} \frac{\gamma_w(\chi,t)}{x-\chi} d\chi \tag{3.25}$$

On the airfoil (so for $-b \leq x \leq +b$) it is possible to define a relationship between the pressure and the bound circulation

$$\Delta P = \rho u_0 \gamma_b + \rho \int_{-b}^{x} \frac{\delta \gamma_b}{\delta t} d\chi \tag{3.26}$$

Defining the total bound circulation Γ of the airfoil as

$$\Gamma = \int_{-b}^{+b} \gamma_b d\chi \tag{3.27}$$

the conservation of circulation requires that

$$\frac{\delta \lambda}{\delta t} + u_0 \frac{\delta \lambda}{\delta x} - \frac{1}{2\pi} \frac{d\Gamma/dt}{b-x} = 0 \tag{3.28}$$

In order to transform eq. 3.23–3.28 in a matrix form easier to apply for the generalized loads all the variables must be expressed as expansions of the Glauert variable φ. The change of variable is given by

$$x = b \cos \varphi \tag{3.29}$$

so that when $x = -b$, $\varphi = 0$, and when $x = +b$, $\varphi = \pi$. The expansions of the

considered variables are

$$\gamma_b = 2\left[\frac{\gamma_s}{\sin\varphi} - \frac{\gamma_0\cos\varphi}{\sin\varphi} + \sum_{n=1}^{\infty}\gamma_n\sin(n\varphi)\right] \tag{3.30}$$

$$\Delta P = 2\rho\left[\frac{\tau_s}{\sin\varphi} - \frac{\tau_0\cos\varphi}{\sin\varphi} + \sum_{n=1}^{\infty}\tau_n\sin(n\varphi)\right] \tag{3.31}$$

$$w = \sum_{n=0}^{+\infty} w_n\cos(n\varphi) \tag{3.32}$$

$$\lambda = \sum_{n=0}^{+\infty}\lambda_n\cos(n\varphi) \tag{3.33}$$

$$h = \sum_{n=0}^{\infty} h_n\cos(n\varphi) \tag{3.34}$$

where the terms $\cos(n\varphi)$ are equivalent to the Chebychev polynomials. As shown in Fig. 3.3 it is possible to evidence the physical meaning of the coefficient for the generalized airfoil displacements, for instance, the first term (h_0) represent the plunge motion, the second (h_1) the pitch, and the third (h_2) the camber, while all the following represent other displacements modes. In this work only the first 3 displacements modes would be considered, and for the third one only static camber would be used.

The equation 3.31 can be simplified by means of the Kutta condition expressing τ_s as a function of the Glauert loads

$$\tau_s = f\tau_0 \tag{3.35}$$

where f is the reversed flow parameter. The sign of f must change accordingly with the direction of the velocity u_0. The choice for f can be many, but the main cases are

- $f = 1$ if there is not any flow reversion
- $f = sgn(u_0)$ if the loads change sign instantaneously
- $f = cos(\alpha)$ if the reversion is smooth.

In the first case the zero pressure point is always in $x = +b$, while in the second case it can be either in $x = +b$ or $x = -b$ according to sign of u_0.

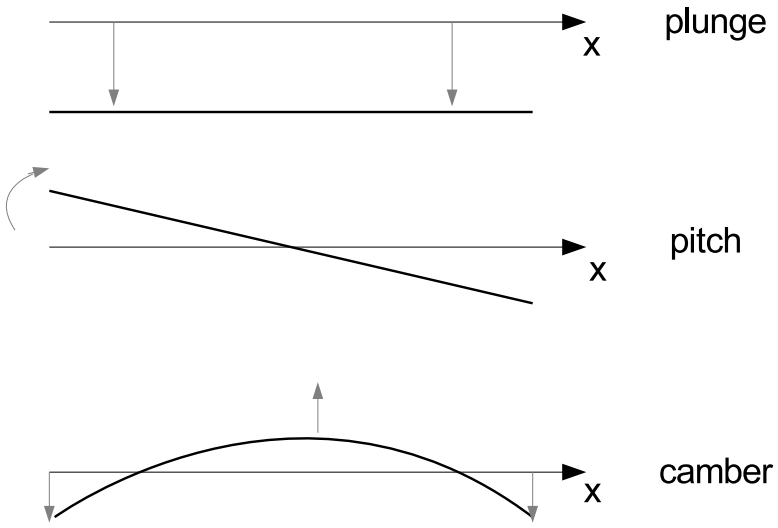

Figure 3.3: Physical meaning of the first three shape functions.

Combining the previous equations [75] the following expressions are obtained

$$u_0(w_0 - \lambda_0) = \tau_0 \tag{3.36}$$

$$b(\dot{w}_0 - \frac{1}{2}\dot{w}_2 + u_0 w_1) = \tau_1 \tag{3.37}$$

$$\frac{b}{2n}(\dot{w}_{n-1} - \dot{w}_{n+1}) + u_0 w_n = \tau_n \qquad n \geq 2 \tag{3.38}$$

so that the loads are functions of airfoil motions w and the uniform component of induced flow λ_0.

The generalized loads can be expressed using the virtual work

$$L_n = \int_{-b}^{+b} \Delta P \cos(n\varphi) d\chi = -\int_0^{\pi} \Delta P \cos(n\varphi) \sin\varphi d\varphi \tag{3.39}$$

where L_n is a force for unit length. Substituting here the expansion of eq. 3.31 the

final form for the generalized loads is

$$L_0 = -2\pi\rho b f u_0(w_0 - \lambda_0) - \pi\rho b u_0 w_1 - \pi\rho b^2(\dot{w}_0 - \frac{1}{2}\dot{w}_2) \tag{3.40}$$

$$L_1 = \pi\rho b u_0(w_0 - \lambda_0) - \frac{1}{2}\pi\rho b u_0 w_2 - \frac{1}{8}\pi\rho b^2(\dot{w}_1 - \dot{w}_3) \tag{3.41}$$

$$L_2 = \frac{1}{2}\pi\rho b u_0(w_1 - w_3) + \frac{1}{2}\pi\rho b^2(\dot{w}_0 - \frac{1}{2}\dot{w}_2) - \frac{1}{12}\pi\rho b^2(\dot{w}_2 - \dot{w}_4) \tag{3.42}$$

$$L_n = \frac{1}{2}\pi\rho b u_0(w_{n-1} - w_{n+1}) + \frac{1}{4(n-1)}\pi\rho b^2(\dot{w}_{n-2} - \dot{w}_n) + \\ -\frac{1}{4(n+1)}\pi\rho b^2(\dot{w}_n - \dot{w}_{n+2}) \qquad n \geq 3 \tag{3.43}$$

In this case the load L_0 represent a uniform force that act in the negative y direction, so its absolute value is the lift for unit length, while L_1 is a linear force distribution, thus $L_1 x/2$ is the nose up pitching moment about the mid chord. The total bound circulation can be expressed as

$$\Gamma = 2\pi b\left[f(w_0 - \lambda_0) + \frac{1}{2}w_1 - \frac{1}{2}\lambda_1\right] \tag{3.44}$$

Although the lift is perpendicular to the local airfoil surface, a parallel component of force can be defined as

$$D = \int_0^\pi b\Delta P\frac{\delta h}{\delta x}\sin\varphi d\varphi - 2\pi\rho b f(w_0 - \lambda_0)^2 \tag{3.45}$$

where a positive value represent a induced drag and a negative value implies a propulsive force.

In order to rewrite the generalized loads in a more compact form it is useful to express the total induced inflow expansion coefficients, using eq. 3.23, as

$$w_0 = v_0 + \dot{h}_0 + u_0\sum_{n=1,3,5}^{\infty}\frac{nh_n}{b} \tag{3.46}$$

$$w_1 = v_1 + \dot{h}_1 + 2u_0\sum_{n=2,4,6}^{\infty}\frac{nh_n}{b} \tag{3.47}$$

$$w_m = \dot{h}_m + 2u_0\sum_{n=m+1,m+3}^{\infty}\frac{nh_n}{b} \qquad m \geq 2 \tag{3.48}$$

Substituting in eq. 3.40–3.45 and rearranging the matrix form obtained is

$$\begin{aligned}
\frac{1}{2\pi\rho}\boldsymbol{L}_n &= -b^2\boldsymbol{M}\left[\ddot{\boldsymbol{h}}_n + \dot{\boldsymbol{v}}_n\right] - bu_0\boldsymbol{C}\left[\dot{\boldsymbol{h}}_n + \boldsymbol{v}_0 - \boldsymbol{\lambda}_0\right] - u_0^2\boldsymbol{K}\boldsymbol{h}_n + \\
&\quad -b\boldsymbol{G}\left[\dot{u}_0\boldsymbol{h}_n - u_0\boldsymbol{v}_n + u_0\boldsymbol{\lambda}_0\right] \qquad (3.49)\\
\frac{1}{2\pi}\Gamma &= b\boldsymbol{U}^T\left[\boldsymbol{C} - \boldsymbol{G}\right]\left[\dot{\boldsymbol{h}}_n + \boldsymbol{v}_n - \boldsymbol{\lambda}_1\right] + u_0\boldsymbol{U}^T\boldsymbol{K}\boldsymbol{h}_n \qquad (3.50)\\
\frac{1}{2\pi\rho}D &= -b\left[\dot{\boldsymbol{h}}_n + \boldsymbol{v}_n - \boldsymbol{\lambda}_0\right]^T\boldsymbol{S}\left[\dot{\boldsymbol{h}}_n + \boldsymbol{v}_n - \boldsymbol{\lambda}_0\right] + b\left[\ddot{\boldsymbol{h}}_n + \dot{\boldsymbol{v}}_n\right]^T\boldsymbol{G}\boldsymbol{h}_n + \\
&\quad -u_0\left[\dot{\boldsymbol{h}}_n + \boldsymbol{v}_n - \boldsymbol{\lambda}_n\right]^T\left[\boldsymbol{K} - \boldsymbol{H}\right]\boldsymbol{h}_n + \left[\dot{u}_0\boldsymbol{h}_n - u_0\boldsymbol{v}_n + u0\boldsymbol{\lambda}_0\right]^T\boldsymbol{H}\boldsymbol{h}_n \\
&\qquad (3.51)
\end{aligned}$$

The definition of the matrix and vector used above are given in Appendix C.

3.4.2 Dynamic inflow motion

2D inflow

In order to compute the loads in the 2D case it is necessary to know the λ_0 component of the induced inflow. This is easily found using a two dimensional inflow model. From reference [76] and [19] the expansion coefficients of the induced inflow are written as a function of a functional

$$Q[f(x)] = -\frac{1}{\pi}\int_b^\infty \gamma_w f(x)dx = -\frac{1}{\pi}\int_b^\infty \gamma_w g(\eta)\sinh(\eta)d\eta \qquad (3.52)$$

with $f(x)$ and $g(\eta)$ are two generic function, thus

$$\begin{aligned}
\Gamma &= \frac{1}{2}Q[1] \qquad (3.53)\\
\lambda_0 &= \frac{1}{2}Q\left[\frac{1}{\sinh(\eta)}\right] \qquad (3.54)\\
\lambda_n &= \frac{1}{2}Q\left[\frac{e^{-n\eta}}{\sinh(\eta)}\right] \qquad (3.55)
\end{aligned}$$

Applying the functional to eq. 3.28 and integrating by parts then

$$\begin{aligned}
\dot{Q}[f] &= \frac{1}{\pi}\int_b^\infty \frac{d\gamma_w}{dx}f(x)dx \\
&= -\frac{1}{\pi}f(1)\gamma_w(1) - \frac{1}{\pi}\int_0^\infty \frac{d\gamma_w}{dx}f(x)dx = 2\dot{\Gamma}f(1) + Q\left[\frac{df}{dx}\right] = \\
&= 2\dot{\Gamma}g(0)\left[\frac{dg/d\eta}{\sinh(\eta)}\right] \qquad (3.56)
\end{aligned}$$

In order to ensure that $g(0) = f(1)$ is finite then $g(\eta)$ should be in the form

$$g(\eta) = \frac{e^{-(n-1)\eta} - e^{-(n+1)\eta}}{\sinh(\eta)} = 2e^{-n\eta} \tag{3.57}$$

To determine λ_0 is necessary another expression, that relate it with λ_n. Writing $Z = e^{-\eta}$, for each η greater than zero it is valid

$$1 \approx \sum_{n=1}^{\infty} b_n Z^n \qquad 0 < Z \leq 1 \tag{3.58}$$

Then λ_0 can be expressed as

$$\lambda_0 \approx \frac{1}{2} \sum_{n=1}^{\infty} b_n \lambda_n \tag{3.59}$$

with the constraint $\sum b_n = 1$. There are many different choices for b_n, but one of the best is the augmented least squares

$$\begin{aligned} b_n &= (-1)^{n-1} \frac{(N+n)!}{(N-n)!} \frac{1}{(n!)^2} \qquad n = 1,2,\ldots,N-1 \\ b_N &= (-1)^{N-1} \end{aligned} \tag{3.60}$$

Applying the identity to equation 3.28 the result differential equation for the generalized inflow states can be obtained

$$\begin{aligned} b\left(\dot{\lambda}_0 - \frac{1}{2}\dot{\lambda}_2\right) + u_0\lambda_1 &= \frac{\dot{\Gamma}}{\pi} \\ \frac{b}{2n}\left(\dot{\lambda}_{n-1} - \dot{\lambda}_{n+1}\right) + u_0\lambda_n &= \frac{\dot{\Gamma}}{n\pi} \qquad n \geq 2 \end{aligned} \tag{3.61}$$

Combining eq. 3.44, 3.59, and 3.60 and differentiating, the right hand side of previous equation becomes

$$\dot{\Gamma} = 2\pi b \left[f(\dot{w}_0 - \frac{1}{2}\boldsymbol{b}^T\dot{\boldsymbol{\lambda}}) + \frac{(\dot{w}_1 - \dot{\lambda}_1)}{2} \right] + \dot{\Gamma}_0 \tag{3.62}$$

where Γ_0 is the total bound circulation due to stall. Substitution in eq. 3.61 and rearranging in a matrix form, the expression for the induce inflow is

$$\dot{\boldsymbol{\lambda}} = \boldsymbol{A}^{-1} \left[\boldsymbol{c} \left(\boldsymbol{e}^T \left(\dot{\boldsymbol{v}}_n + \ddot{\boldsymbol{h}}_n \right) + \frac{u_0}{b} \boldsymbol{f}^T \dot{\boldsymbol{h}}_n + \frac{\dot{\Gamma}_0}{2b\rho} \right) - \frac{u_0}{b} \boldsymbol{\lambda} \right] \tag{3.63}$$

Only λ_0 is required to obtain the airloads, but all λ_n are coupled, thus many states are necessary.

3D inflow

If the whole rotor is considered it is necessary to evaluate the effective 3D induced inflow. In this case the Peters–HaQuang induced airflow can be considered [73]. This model uses three dynamic variables as states for the description of the inflow. The advantage of this model is that describes the nonlinear dynamic inflow model, including perturbations in hub motions, in skew angle, and in yaw angle, but keeping low complexity with respect to higher order models (e.g. [74]).

The inflow velocity field is thus described by three components, the first one, ν_0, represents the uniform component, while the other two, ν_c and ν_s, are the first harmonic terms, or rather the longitudinal and lateral variations of the inflow. The velocity field is therefore described as

$$\nu_i(x,\psi) = \Omega R \left(\nu_0 + \nu'_s \frac{r_{el}}{R} \sin\psi + \nu'_c \frac{r_{el}}{R} \cos\psi \right) \tag{3.64}$$

The time histories of the components of the velocity field are described by the following equation in hub wind axes:

$$\frac{1}{\Omega} \boldsymbol{M}_\lambda \begin{Bmatrix} \dot{\nu}_0 \\ \dot{\nu}'_s \\ \dot{\nu}'_c \end{Bmatrix} + \boldsymbol{L}_\lambda^{-1} \begin{Bmatrix} \nu_0 \\ \nu'_s \\ \nu'_c \end{Bmatrix} = \begin{Bmatrix} C_T \\ C'_l \\ C'_m \end{Bmatrix} \tag{3.65}$$

where C_T, C'_l, and C'_m are the aerodynamic contribution to the thrust, and roll and pitch moment coefficients, the apparent mass matrix is defined as

$$\boldsymbol{M}_\lambda = \begin{bmatrix} 8/3\pi & 0 & 0 \\ 0 & -16/45\pi & 0 \\ 0 & 0 & -16/45\pi \end{bmatrix} \tag{3.66}$$

and the static gain matrix is

$$\boldsymbol{L}_\lambda = \begin{bmatrix} \frac{1}{2v_T} & 0 & \frac{15\pi}{64v_M} \tan\frac{\chi}{2} \\ 0 & -\frac{4}{v_M(1+\cos\chi)} & 0 \\ \frac{15\pi}{64v_M} \tan\frac{\chi}{2} & 0 & -\frac{4\cos\chi}{v_M(1+\cos\chi)} \end{bmatrix} \tag{3.67}$$

In order to express in the non–rotating shaft frame is is necessary to multiply for the rotating matrix $\tilde{\boldsymbol{L}}_{wS}$ (defined in Appendix A) so that

$$\frac{1}{\Omega} \boldsymbol{M} \begin{Bmatrix} \dot{\nu}_0 \\ \dot{\nu}_s \\ \dot{\nu}_c \end{Bmatrix} + \boldsymbol{L}^{-1} \begin{Bmatrix} \nu_0 \\ \nu_s \\ \nu_c \end{Bmatrix} = \begin{Bmatrix} C_T \\ C_l \\ C_m \end{Bmatrix} \tag{3.68}$$

3.4.3 Dynamic Stall Model

As described in section 1.3.4 there are many methods for the description of the dynamic stall phenomenon. The ONERA method for the study of dynamic stall has the advantage that is not based on curve fitting process from experimental data, but is instead based on ordinary differential equations.

Considering fig. 3.4 it can be seen the static stall phenomenon. When the angle of attack go beyond a certain limit (α_S) the airfoil begin to stall, so that a static loss of lift occur. The difference between the linear lift and the static lift is the driving factor in the equation for the dynamic stall in the ONERA method [77]. The same logic can be applied for any airloads.

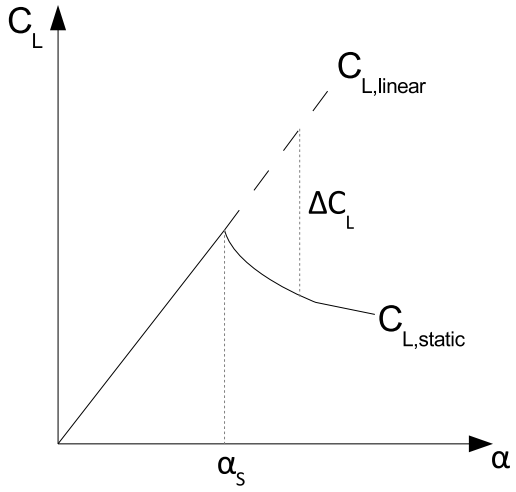

Figure 3.4: Static stall illustration

In literature a closed–form for the study of dynamic stall does not exist, but it is possible to define it as a transfer function [77]. At first the differential equations associated to transfer functions were found by comparison with experimental results on an airfoil undergoing small amplitude oscillation. Later version of ONERA method considered bigger oscillations and separated the effects of plunge and pitch motions.

The model inputs are the instantaneous angle of attack, its first and second derivatives, and speed of the airfoil. Each load can be described as a sum of two

components, one described by a first order differential equation and the second by a second order equation, whit which time delay and overshoot due to the shed vorticity can be taken into account. The first components represent the response to airfoil oscillations below stall, while the second the variation introduced beyond stall.

Using F to represent the airload considered, then

$$F = F_1 + F_2 \tag{3.69}$$

$$\dot{F}_1 + \lambda F_1 = \lambda F_l + (\lambda s + \sigma)\,\dot{\alpha} + s\ddot{\alpha} \tag{3.70}$$

$$\ddot{F}_2 + \eta \dot{F}_2 + \omega^2 F_2 = -\omega^2 \left(\Delta F_0 + e \frac{\delta \Delta F_0}{\delta \theta} \dot{\theta} \right) \tag{3.71}$$

where ΔF_0 represent the departure of the static coefficient from its linear trend (as shown in Fig. 3.4), and λ, σ, s, η, ω, and e can be determined by parameter identification. If, for example, the lift coefficient is substituted in eq. 3.70–3.71, then the first equation is used to determine the static lift coefficient, while using the second the lift loss can be calculated.

Reference [68] shows that the model can be written in terms of lift coefficient, C_L, non–dimensional circulation, Γ, or non–dimensional lift, L. If the free stream velocity is steady then the three forms are exactly equivalent, while the presence of variations in that term can change the response. The same reference determines that the behavior closer to experimental results is obtained using the non–dimensional circulation in expression 3.70–3.71. From comparisons with experimental results some observations were made in [68] that led to some modifications on the original ONERA method, thus for example

- the angle of attack due to plunge should be treated separately
- circulatory and mass lift should not be treated by the same transfer function

The final form of the ONERA method in a rotating reference frame can be written as

$$\bar{k}\Gamma_1^+ + \hat{\lambda}\Gamma_1 = +\hat{\lambda}\hat{a}U + \hat{\sigma}\bar{b}\hat{\epsilon} \tag{3.72}$$

$$\bar{k}^2\Gamma_2^{++} + \bar{k}\hat{\eta}\Gamma_2^+ + \hat{\omega}^2\Gamma_2 = -\hat{\omega}^2 \left[U\Delta C_L + \hat{e}\bar{k} \left(U^+ \Delta C_L + \frac{\delta \Delta C_L}{\delta \theta} U^+ \right) \right] \tag{3.73}$$

where $^+$ represent the differentiation with respect to the non dimensional time based on the averaged u_0, $\hat{\epsilon}$ represents the rotation rate of the airfoil with respect to the air mass, and

$$\bar{k} = \frac{b}{r} \tag{3.74}$$

$$\bar{b} = \frac{b}{R} \tag{3.75}$$

The coefficient involved in equation 3.73 are generally time dependent, but ONERA assume that the variations are sufficiently slow to be found by means of dynamic perturbations of angle of attack. Both ONERA and NASA performed tests in order to obtain values for the parameters that led to a behavior similar to experiments [77], [54]. The functional form of the dynamic stall coefficient resulted to be

$$\hat{\omega} = \omega_0 + \omega_2 \left(\Delta C_L\right)^2 \tag{3.76}$$
$$\hat{\eta} = \eta_0 + \eta_2 \left(\Delta C_L\right)^2 \tag{3.77}$$
$$\hat{e} = e_0 + e_2 \left(\Delta C_L\right)^2 \tag{3.78}$$

3.4.4 The Unified Model

The unified model allow to use Peter's finite state theory to compute the generalized loads and then correct them using the ONERA dynamic stall method. The dynamic stall parameter are assumed constant for all the generalized loads, considering them as a characteristic of the fluid. When considering the complete rotor it can be not sufficient to consider the 2D inflow model, but it is more convenient to use the Peters–HaQuang model [73]. Under this assumption then

$$\lambda_0 = \nu_i = \Omega R \left(\nu_0 + \frac{r_{el}}{R} \sin\psi + \frac{r_{el}}{R} \cos\psi\right) \tag{3.79}$$

The expressions for the generalized loads remains that of Eq. 3.50 through 3.51 using the appropriate inflow model described above, summed to the total dynamic stall correction factor:

$$\boldsymbol{L}_{n,tot} = \boldsymbol{L}_n + \rho u_T \Gamma_2 \tag{3.80}$$

One of the benefits of the airloads theory presented here is that there is no need to assume a particular direction for the linear lift. The rigorous application of the definition of motion between the fluid and the airfoil gives back the x and y in the correct way, without considering the small perturbation theory. The scheme used to calculate the total airloads is presented in Fig. 3.5.

3.5 Small Scale Rotorcraft Models

The quad-rotor under consideration consists of a rigid cross frame equipped with four rotors as shown in Fig. 3.6.a. The model is derived under the assumptions that motor and rotor response is fast and their dynamics can therefore be neglected. Also, rotor blades are assumed to be rigid (i.e. no blade flapping occurs). As outlined above, control moments can be obtained either differentially changing the value of

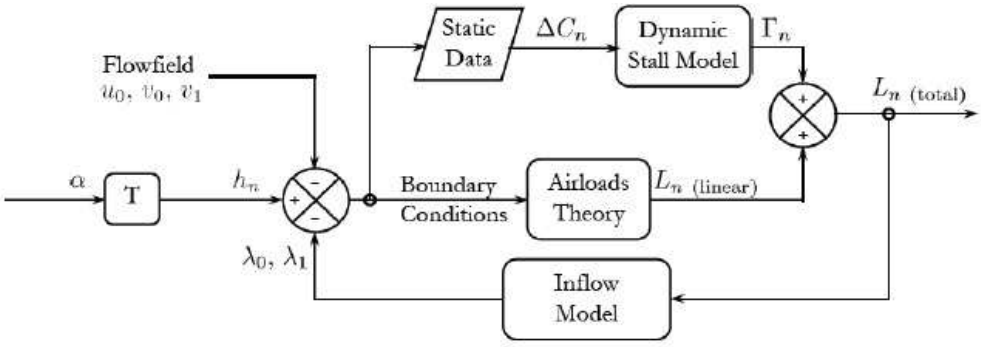

Figure 3.5: Unified model operating scheme

thrust and torque of each rotor changing its angular speed or tilting the rotor so that thrust can be projected into a horizontal and a vertical component in the body frame. The configuration of the quad-rotor with all the rotors tilted is shown in Fig. 3.6.b.

The equations of motion are developed in terms of the translational and rotational velocities represented in body-frame components, $\boldsymbol{v}_b$ and $\boldsymbol{\omega}_b$, where attitude is represented using quaternions, $(q_0,\boldsymbol{q}^T)^T$, [95]:

$$\dot{\boldsymbol{v}}_b = -\boldsymbol{\omega}_b \times \boldsymbol{v}_b + \frac{\boldsymbol{F}}{m} + \boldsymbol{g}_b \tag{3.81}$$

$$\dot{\boldsymbol{\omega}}_b = \boldsymbol{J}^{-1}\left[\boldsymbol{M} - \boldsymbol{\omega}_b \times (\boldsymbol{J}\boldsymbol{\omega}_b)\right] \tag{3.82}$$

$$\dot{q}_0 = -\frac{1}{2}\boldsymbol{\omega}_b \cdot \boldsymbol{q} \tag{3.83}$$

$$\dot{\boldsymbol{q}} = \frac{1}{2}\left(q_0\boldsymbol{\omega}_b - \boldsymbol{\omega}_b \times \boldsymbol{q}\right) \tag{3.84}$$

$$\dot{\boldsymbol{r}}_i = \boldsymbol{T}_{bi}\boldsymbol{v}_b \tag{3.85}$$

where $\boldsymbol{F}$ and $\boldsymbol{M}$ indicate aerodynamic force and moments, respectively, $\boldsymbol{g}_b$ is gravity acceleration, $\boldsymbol{J}$ is the inertia tensor, and $\boldsymbol{T}_{bi}(q_0,\boldsymbol{q}^T)$ is the coordinate transformation matrix from inertial to body frame.

The use of quaternions for attitude representation allows the simulation of more aggressive maneuvers, that requires unusual pitch attitude that cannot be represented using Euler angles. The aerodynamic force acting on the quad-rotor $\boldsymbol{F}$ is given by the difference between rotor thrust and vehicle drag:

$$\boldsymbol{F} = \boldsymbol{T} - \boldsymbol{D} \tag{3.86}$$

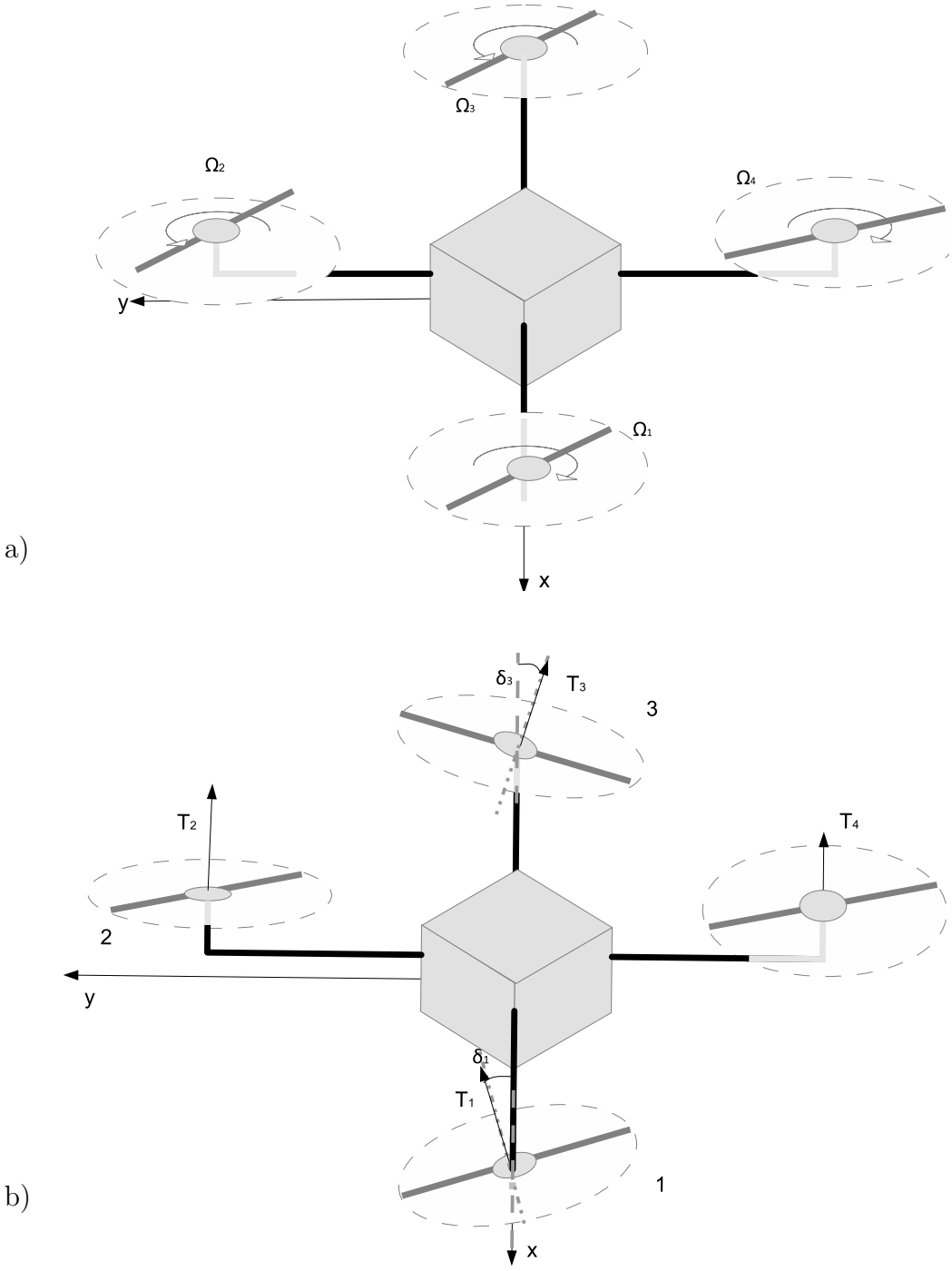

a)

b)

Figure 3.6: Quad-rotor configurations: a) conventional; b) with tilting rotors.

Letting $\mathrm{s}\delta_i = \sin\delta_i$ and $\mathrm{c}\delta_i = \cos\delta_i$, it is

$$\boldsymbol{T} = k_t \begin{bmatrix} 0 & \mathrm{s}(\delta_2) & 0 & -\mathrm{s}(\delta_4) \\ \mathrm{s}(\delta_1) & 0 & -\mathrm{s}(\delta_3) & 0 \\ -\mathrm{c}(\delta_1) & -\mathrm{c}(\delta_2) & -\mathrm{c}(\delta_3) & -\mathrm{c}(\delta_3) \end{bmatrix} \begin{Bmatrix} \Omega_1^2 \\ \Omega_2^2 \\ \Omega_3^2 \\ \Omega_4^2 \end{Bmatrix} \tag{3.87}$$

Drag is considered only for the quad-rotor body. The body is assumed to be a prism with a square base. Following [32], the components of the drag force can be expressed as

$$\boldsymbol{D} = \frac{1}{2}\rho \begin{Bmatrix} C_{dx} S_x V_{bx}^2 \\ C_{dy} S_y V_{by}^2 \\ C_{dz} S_z V_{bz}^2 \end{Bmatrix} \tag{3.88}$$

with $C_{dx} = C_{dy} = 0.8$ and $C_{dz} = 1.05$, [36]. Similarly the moment applied on the quad-rotor is defined as

$$\begin{aligned} \boldsymbol{M} &= \left(k_t \frac{b}{2} \begin{bmatrix} 0 & -\mathrm{c}\delta_2 & 0 & \mathrm{c}\delta_4 \\ -\mathrm{c}\delta_1 & 0 & \mathrm{c}\delta_3 & 0 \\ \mathrm{s}\delta_1 & \mathrm{s}\delta_2 & -\mathrm{s}\delta_3 & -\mathrm{s}\delta_4 \end{bmatrix} \right. \\ &+ \left. k_c \begin{bmatrix} 0 & \mathrm{s}(\delta_2) & 0 & \mathrm{s}(\delta_4) \\ \mathrm{s}(\delta_1) & 0 & \mathrm{s}(\delta_3) & 0 \\ -\mathrm{c}(\delta_1) & \mathrm{c}(\delta_2) & \mathrm{c}(\delta_3) & -\mathrm{c}(\delta_4) \end{bmatrix} \right) \begin{Bmatrix} \Omega_1^2 \\ \Omega_2^2 \\ \Omega_3^2 \\ \Omega_4^2 \end{Bmatrix} \end{aligned} \tag{3.89}$$

The control inputs modify the variation of rotor angular rate and tilt angle. Letting

$$\boldsymbol{\delta} = \begin{bmatrix} 1 & 0 & 1 \\ 1 & 1 & 0 \\ 1 & 0 & -1 \\ 1 & -1 & 0 \end{bmatrix} \begin{Bmatrix} w_1 \\ w_2 \\ w_3 \end{Bmatrix} \tag{3.90}$$

and $\boldsymbol{U}_\Omega = (\Omega_1,\Omega_2,\Omega_3,\Omega_4)^T = \boldsymbol{U}_{\Omega_0} + \boldsymbol{\Delta\Omega}$, with

$$\boldsymbol{\Delta\Omega} = \Omega_0 \begin{bmatrix} 1 & 0 & 1 & 1 \\ 1 & 1 & 0 & -1 \\ 1 & 0 & -1 & 1 \\ 1 & -1 & 0 & -1 \end{bmatrix} \begin{Bmatrix} u_1 \\ u_2 \\ u_3 \\ u_4 \end{Bmatrix} \tag{3.91}$$

the vector of control inputs is given by
$u = (u_1,u_2,u_3,u_4,w_1,w_2,w_3)^T$.

With respect to the control inputs of a conventional single main rotor helicopter, it is possible to notice that the variation of u_1 increases overall rotor thrust and it is thus equivalent to a collective command; u_2 and w_2 provide longitudinal control moments (that is, they are equivalent to a longitudinal cyclic pitch variation), whereas u_3 and w_3 develop a roll control moment, equivalent to the effect of lateral cyclic; finally u_4 and w_1 represent yaw commands, that substitute tail rotor pitch.

Chapter 4

Flexible Aircraft Dynamic Response

4.1 Case Study

The reference flexible aircraft model adopted for this study is a fictitious modern highly deformable twin-engine wide-body aircraft designed for carrying 250 passengers. The main characteristics of the aircraft are summarized in Table 4.1 and Fig. 4.1. A trim speed of $V = 186$ m/s at a cruise altitude of 37,000 ft (that is, 11,300 m) was selected for the stability analysis and for the determination of response to controls. The corresponding Mach number is approximately equal to M= 0.6, such that the flight condition lies in the subsonic range. Trim values for state and control variables are reported in Table 4.2 for both rigid and deformable aircraft case. These values are used as initial conditions for all the simulations reported in the sequel.

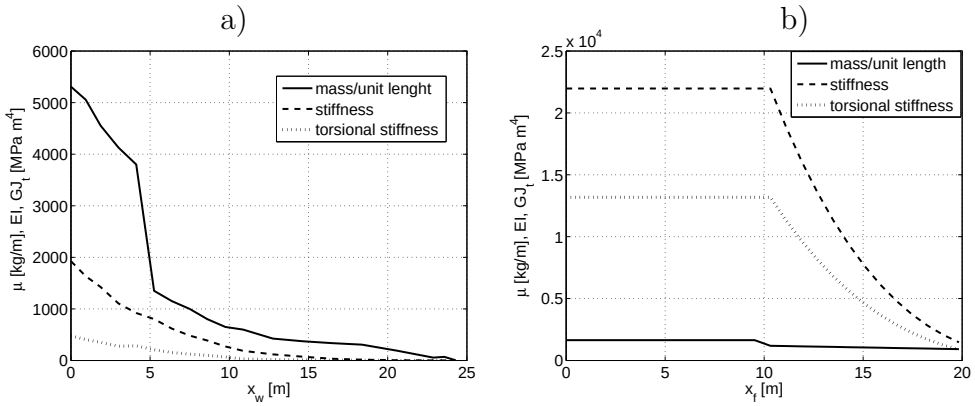

Figure 4.1: Linear density and stiffness distribution for deformable elements: (a) wing; (b) fuselage.

As outlined above, the elastic elements of the configuration are the aft fuselage

Table 4.1: Aircraft data

Data	**Symbol**	**Value**	**Unit**
Total mass	m	235000	kg
Forebody mass	m_{fb}	57100	kg
Tail assembly mass	m_{tip_f}	7000	kg
Wing span	b	65.6	m
Length of wing deformable portion	ℓ_w	25	m
Wing surface	S	368	m^2
Mean aerodynamic chord	$\bar{c}$	7.14	m
Fuselage length	L_f	59	m
Length of aft-fuselage deformable portion	ℓ_f	19	m

Table 4.2: Aircraft trim data

Data	**Symbol**	**Rigid**	**Deformable**	**Unit**
Cruise altitude	h	11300	11300	m
Trim speed	V	186	186	m/s
Angle of attack	α	8.4	8.25	deg
Elevator deflection	δ_E	7.08	7.60	deg
Throttle setting	δ_T	0.39	0.39	

and the two half-wings, modeled as simple flexible beams. From the inertial point of view, horizontal and vertical tail surfaces are modeled as masses at the tip of the aft-fuselage, whereas engines are included as masses placed along the rigid part of the two half-wings.

In order to obtain a minimum complexity model that can still capture the most important effects of deformations with respect to the simpler rigid body model (which will be referred to as Model R in the sequel), a total of four different flexible aircraft models are considered in the sequel. Quite obviously, the fully flexible model (Model FF) derived according to the approach outlined in the previous section, is used as a reference, where the dynamic response of transport and deformation degrees of freedom includes the effects of deformation on aircraft aerodynamics, inertial coupling terms and variations of inertia properties. Starting from Model FF, three simplified models are then derived. Model QS is a quasi-static model, where all deformation variables are assumed at steady state, under the considered aerodynamic

and maneuver loads. When an approximation of quasi-static deformation is retained only for the (usually faster) torsional deformation dynamics, Model ST is derived, where bending deformation is represented by means of the standard second order dynamics, in the form of Eq. (2.33). Finally, the effects of deformation on moments of inertia and position of the center of mass is neglected and a model with constant inertia properties (Model CI) is derived. In this latter case, all deformation variables are considered in their dynamic formulation.

In all cases, two assumed modes are considered for each deformation variable. This means the the order of Model FF and CI is equal to $n = 8 + 7 \times 4 = 36$. In Model ST, 3 torsional degrees of freedom are dropped, that is a total of 12 state variables, and $n = 24$. Finally, in Model QS deformation dynamics is no longer accounted for and the order is $n = 8$, as in the standard rigid body model.

4.2 Static deformations vs deformable aircraft

In the first set of test cases presented, Models R and FF are compare with Models QS and ST in order to assess the relevance of inertial coupling terms in the equations of motion. When quasi-static deformation is assumed, dynamics of flexible modes is neglected, and deformation depends on current values of maneuvering loads. Deformation thus affects the evolution of transport degrees of freedom mostly because of changes in stability derivatives and control power. The assumption of quasi-static deformations is usually valid when frequency separation between flexible modes and modes associated to transport variables is sufficiently large [22].

The eigenvalues of all the models considered are listed in Table 4.3, including Model CI. The linearized systems are obtained for the reference trim condition reported in Table 4.2 for all cases. A graphical representation of the eigenvalues in the Gauss plane is provided in Fig. 4.2 for Models R, FF, QS and ST. A plot of all the eigenvalues is reported in the upper half of Fig. 4.2, where most rigid-body modes are hardly visible. An enlargement is thus provided in the bottom portion of the figure. As expected, the frequency of modes associated to lower-order flexible variables for half-wings and fuselage are close to fast rigid-body modes. This means that these modes are expected to affect more significantly aircraft stability and response.

Deformation dynamics clearly affects significantly only dutch roll and spiral modes. These variations in the eigenvalues are associated to wing bending, that increases dihedral effect, thus inducing a stabilizing effect for the spiral model, but also a loss of damping for dutch roll. Conversely, longitudinal modes do not undergo major changes, when structure deformation is accounted for in the dynamic model, at any level of complexity. If on one side this is quite obvious for the low-frequency phugoid mode, the fact that short period damping changes only marginally indicates

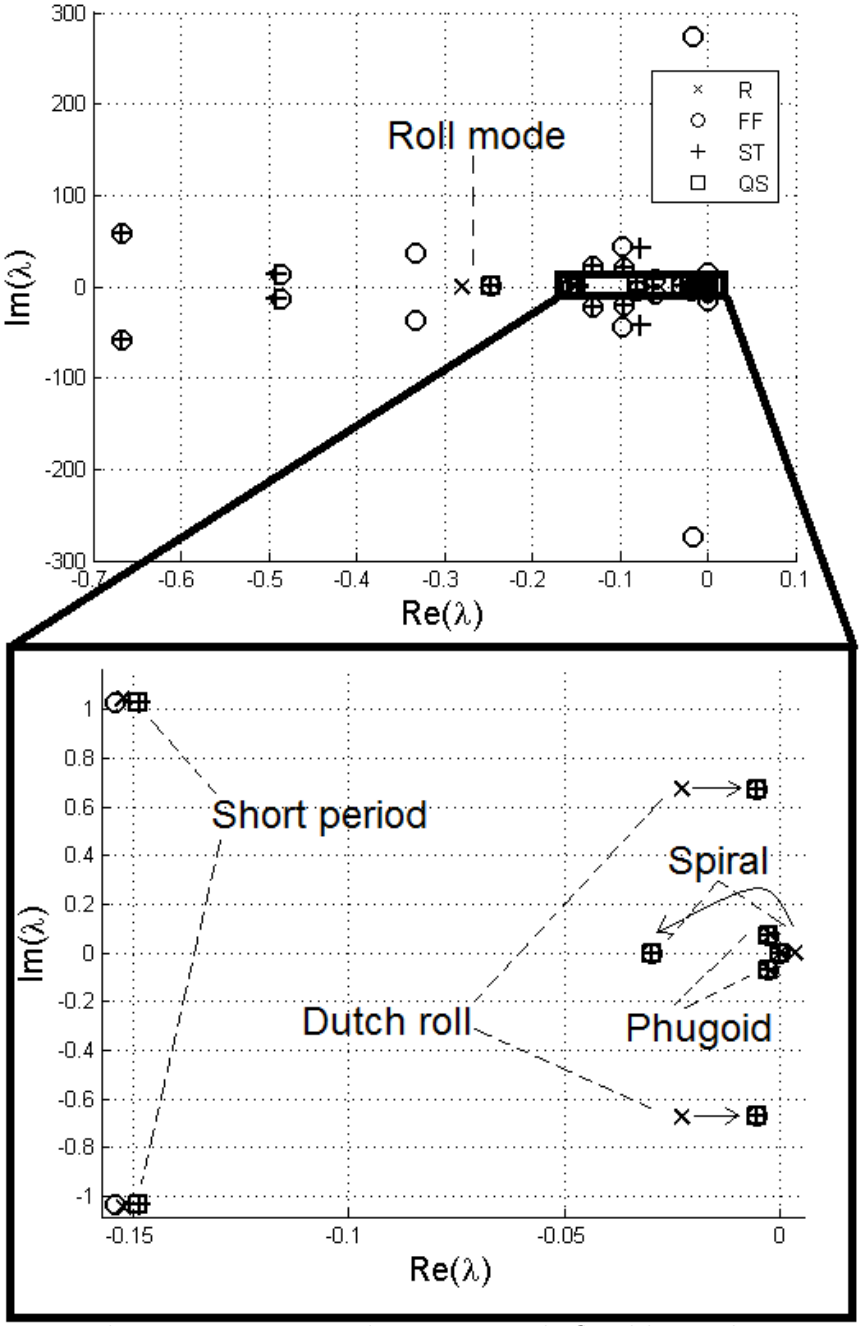

Figure 4.2: Root locus: comparison between rigid, flexible, and quasi-static deformation models.

that fuselage is relatively stiff, for the considered design.

A somehow more pronounced effect of fuselage bending on elevator control power

Table 4.3: Aircraft eigenvalues for rigid (R), fully flexible (FF), quasi–static (QS), static torsion (ST), and constant inertia (CI) cases

R	**FF**	**QS**	**ST**	**CI**
$-0.15 \pm 1.04i$	$-0.15 \pm 1.03i$	$-0.15 \pm 1.03i$	$-0.15 \pm 1.03i$	$-0.15 \pm 1.03i$
$-0.0022 \pm 0.074i$	$-0.0028 \pm 0.073i$	$-0.0028 \pm 0.073i$	$-0.0028 \pm 0.073i$	$-0.0022 \pm 0.073i$
$-0.023 \pm 0.68i$	$-0.0055 \pm 0.67i$	$-0.0052 \pm 0.67i$	$-0.0054 \pm 0.67i$	-0.0054 ± 0.67
-0.28	-0.25	-0.25	-0.24	-0.28
0.0034	-0.030	-0.030	-0.030	0.0053

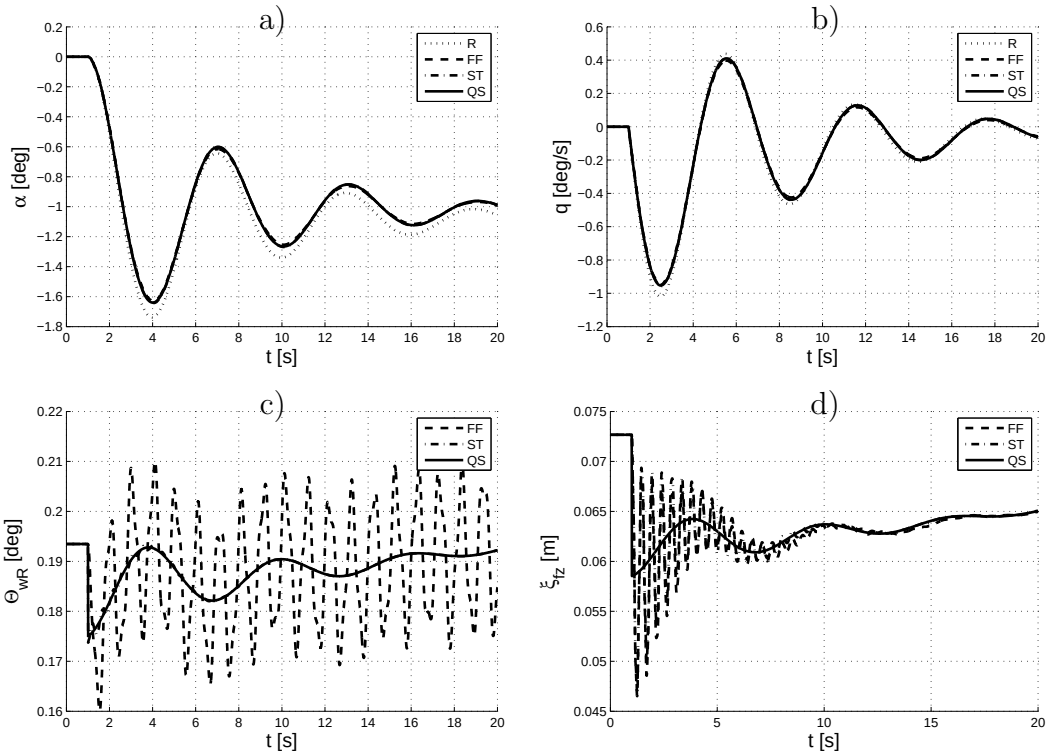

Figure 4.3: Open-loop response to a 2 deg step command on the elevator deflection, rigid, complete and static cases comparison.

is highlighted in Fig. 4.3, where the response of the four aircraft models considered in this section to a pitch down 2 deg step command on elevator deflection from its value at trim is represented. Short period variables $\Delta\alpha$ and q are reported in Figs. 4.3.a and b, whereas Figs. 4.3.c and d provides the time-histories of wing-tip torsional deformation and elastic displacement of fuselage tail, respectively. In Fig. 4.3.a, increments in angle-of-attack are reported, rather than absolute value, to account for minor difference in the values of α at trim for rigid model (R) on one

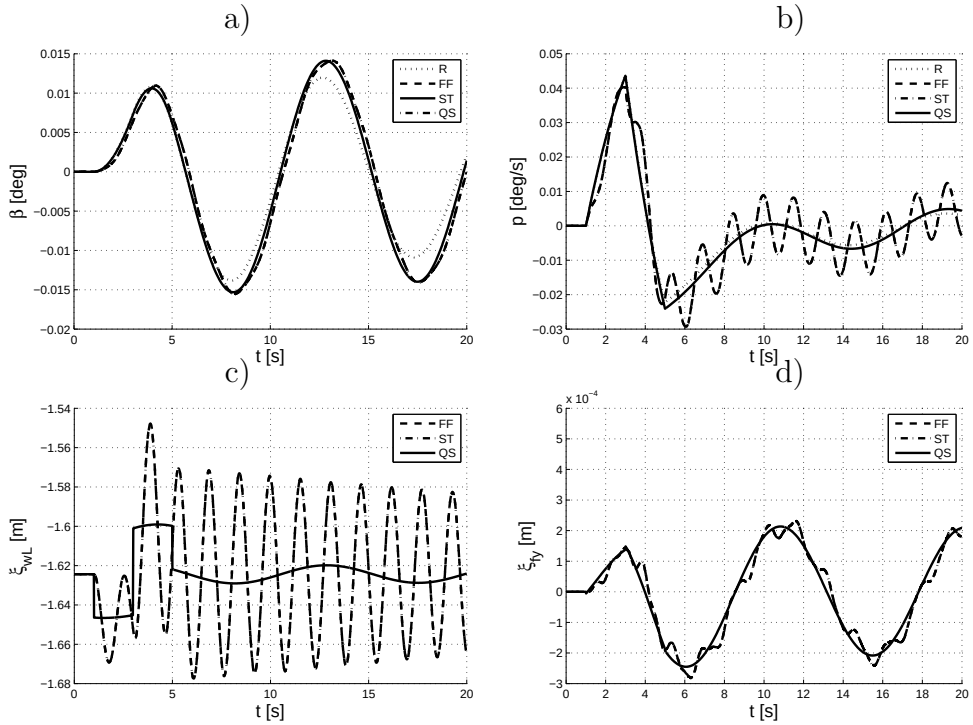

Figure 4.4: Open-loop response to a 1 deg doublet command on the aileron deflection, rigid, complete and static cases comparison.

side and deformable models on the other one (FF, QS, and ST), that, conversely, have the same values of state and control variables at trim.

In this longitudinal test case, a slight reduction in elevator control power is visible, as both peaks on angle of attack and pitch rate response and angle of attack increment at steady state are reduced when the effects of fuselage flexibility is accounted for. Conversely, the reduction of short period damping is so small to be hardly noticeable in aircraft response. As a final observation on this first test-case, the quasi-static model (QS) follows almost exactly the evolution of transport variables obtained from the complete flexible model (FF). In this case there is no significant coupling between the response of transport variables and oscillations of deformation degrees of freedom, and the main effect (a minor loss of control power) is a static one, namely, the deformation induced on the fuselage by the incremental load due to elevator deflection reduces the effective tail angle of attack, leading to a lower initial pitch angular acceleration. As a consequence, longitudinal dynamics can be represented by the quasi-static approximation, which allows savings as large as approximately 40% of computational time (CPU time) for a non-linear simulation, with respect to the CPU time required by a complete flexible model.

In Fig. 4.4 the response to a 1 deg doublet command on the aileron deflection are shown. The same four cases are considered again for a lateral-directional command.

Also in this second case the transient response of the rigid aircraft is quite similar to that of the flexible cases. The effects of deformations is captured by the quasi-static model, where the peak response on roll rate p is slightly reduced because of wing torsional deformation. Also the damping of the oscillation of the rigid body variables is lower. In this case anyway two of the main effects on the rigid body variables is due mostly to wing bending rather then torsion (probably also because the latter is quite small for this aircraft); first in the linear case the spiral mode has become more stable and this means that also in the non-linear simulations the variable Ψ does not diverge and there is a coupling between the oscillation of wing bending and roll rate that could cause a reduction in the handling qualities and the riding comfort, but this effect is completely lost using the completely quasi-static case, while is well modeled by the other quasi-static one.

4.3 Approximately constant moments of inertia

Another simplification is represented by the assumption of constant inertia properties, *i.e.* inertia moments and/or position of the center of mass. If inertia moments are constant in time, it is $\dot{I} = 0$, whereas when center of mass coincide with the origin of the pseudo-body axis frame, it is $\Delta\ddot{\eta} = 0$, $\Delta\dot{\eta} = 0$, and $\Delta\eta = 0$.

Figure 4.5 shows the comparison between the root loci of the rigid, completely flexible, and without the inertia effects models. It could be noted that the presence or the absence of the inertia changes affects some of the flexible modes, but more important the short period and the spiral mode, while the dutch roll, the roll subsidence and the phugoid remain essentially unchanged. While the changes on the short period mode are not so great, the spiral mode becomes closer to the rigid body case then the flexible case.

Figures 4.6 and 4.7 show the response to the same commands used above for a longitudinal and a lateral-directional maneuvers, comparing three cases: the perfectly rigid aircraft (dotted line), the complete deformable model (dashed line), and the deformable model with constant inertia properties (solid line). From the simulations it is clear that this kind of approximation well represents the response of the aircraft for both the inputs considered.

The main advantage of this simplifying assumption is computational time: up to 75% of CPU time required for a nonlinear simulation can be saved, with repect to the completely deformable case, with results close to more complete, fully coupled model, at least for the set of stiffness parameters and mass distribution adopted for the considered aircraft model. This is possible because, when center of mass displacement is not accounted for, the time-varying terms in the mass matrix disappear. It is thus possible to evaluate the coupling matrix $\boldsymbol{A}$ at the beginning of the simulation and invert it only once, rather than at every time-step. Given the

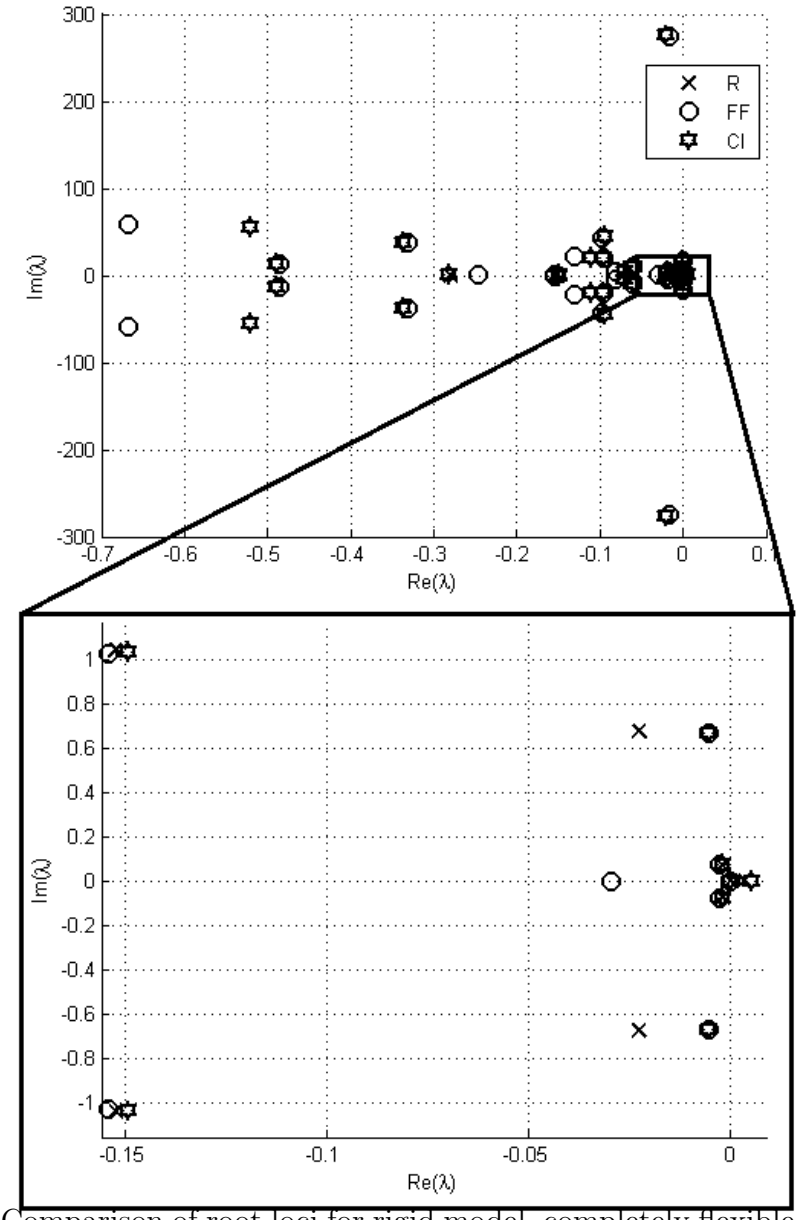

Figure 4.5: Comparison of root loci for rigid model, completely flexible, and without inertia effects.

order of the system, the inversion of the coupling matrix is the computationally most demaning term in the equations of motion.

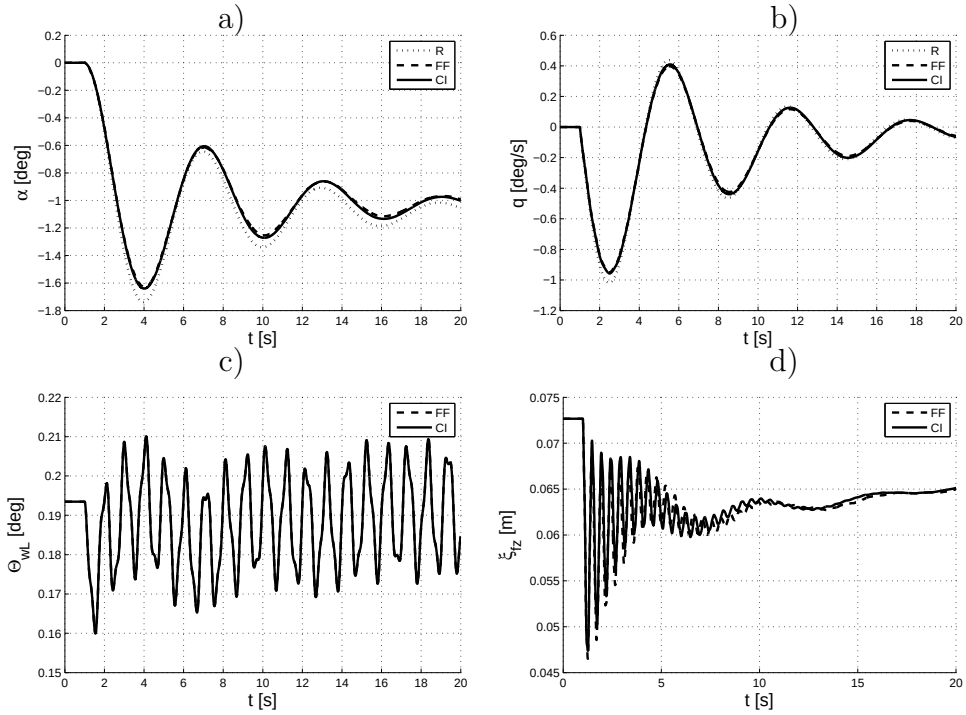

Figure 4.6: Open-loop response to a 2 deg pitch-down step command on the elevator deflection, with or without inertia properties variations.

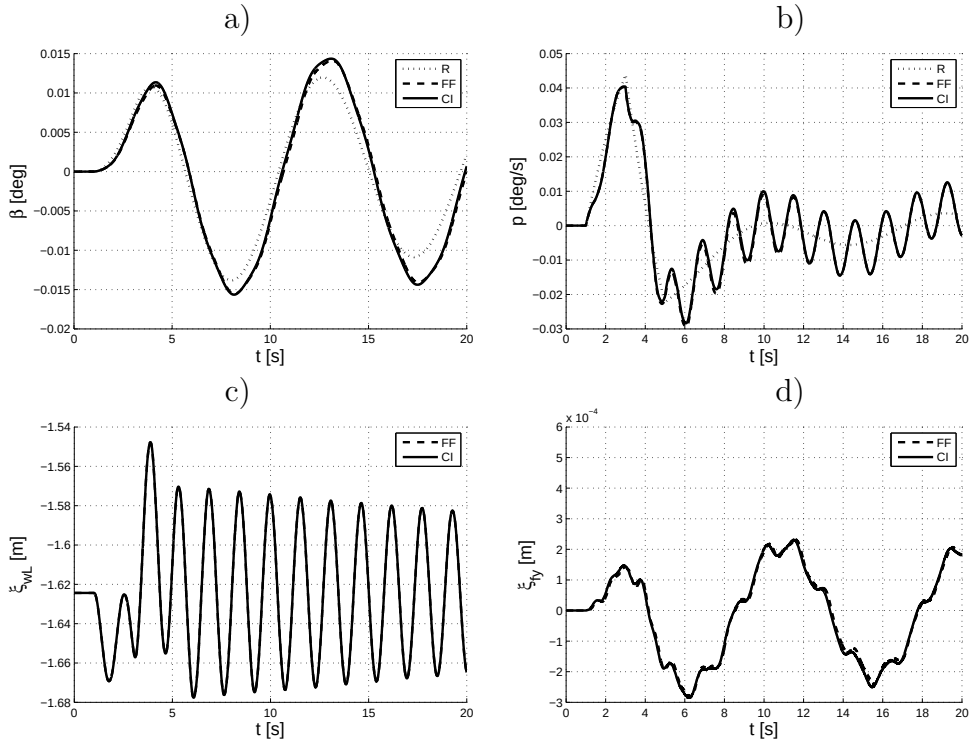

Figure 4.7: Open-loop response to a 2 deg doublet command on the aileron deflection, with or without inertia properties variations.

Chapter 5

Helicopter Unsteady Aerodynamics

5.1 2D test case

In order to validate the model presented in Chapter 3 it was necessary to implement it using consistent numerical values. In literature dynamic stall data considering a NACA0012 airfoil can be easily found [55], so this airfoil was selected for the preliminary analysis. As described before (3.4.3), some parameters are necessary to describe the aerodynamic on the airfoil, that are the $C_L - \alpha$ static curve characteristics, and the coefficient for the description of the dynamic stall (ω_0, ω_2, η_0, η_2, e_0, and e_2). Eq. 3.73 includes the terms ΔC_L and $(\delta \Delta C_L)/(\delta\theta)$. There are many expression for the static stall residual and its derivative in literature, see for example [70, 72, 76], and the one that join accuracy and simplicity is that implemented in the last work

$$\Delta C_L = C_{L0} \cos\alpha + C_{L\alpha} \sin\alpha - C_{Ls} \tag{5.1}$$

where C_{L0} and $C_{L\alpha}$ are the magnitude and the slope for $\alpha = 0$, while C_{Ls} is the static value for the lift coefficient.

In order to completely describe the static stall it is necessary to define 3 coefficients, $\hat{\omega}$, $\hat{\eta}$, and $\hat{e}$. As presented in 3.4.3 these parameters could be describe in a functional form of the flight condition, so that 6 coefficients should be found. In [77] the typical values for the system parameters were defined. Peters et al. works [2, 72, 76] presented different solutions for the determination of these parameters, using parameter identification such as genetic algorithm, in order to obtain the values that allow a closer response of the phenomenon. Reasonable ranges for model parameters proposed by Petot are presented in Table 5.1, together with those used in the following works. Considering Fig. 5.1 it is evident that none of the considered parameters approximate clearly the experimental curve, thus a different set of

Table 5.1: Dynamic Stall Parameter typical values

	Petot	Peters 1994 [72]	Peters 2008 [71]	Ahaus 2010 [2]	Present
ω_0	0.1÷0.4	0.2	0.2581	0.27	0.175
ω_2	0÷0.5	0.1	-0.0264	0.13	0.2
η_0	0.1÷0.4	0.52	0.3861	0.25	0.26
η_2	0÷0.6	0.22	0.3973	0.1	0
e_0	0	3.3	-0.0294	0	3.3
e_2	-0.2÷0	-0.1	-0.1607	-0.3	-0.3

parameters was used, defined in a work by Tomasello [88]. The parameters chosen do not drift apart much from the range defined by Petot, except for e_0. However Peters in [72] explains that using the ONERA method coupled with the finite state requires a greater value for that parameter.

5.2 Main Rotor Results

Once all the parameters needed to describe the dynamic stall are set the complete rotor behavior was considered. As outlined before the reference model used is a Sikorsky UH–60, which main characteristics are listed in Table D.1. This helicopter main rotor has four blades, and for the present analysis each blade was divided in five sections as suggested in [39]. Velocity and angle of attack are evaluated as the magnitude of the velocity component perpendicular to the blade axis and its inclination with respect to the blade chord. All the test are compared to a baseline model in which aerodynamic forces and moments coefficients are evaluated using look–up tables that consider $-180 \leq \alpha \leq 180$ and $0 \leq M \leq 1$. In all models the inflow dynamic is that described in section 3.4.2. Considering the single rotor in the baseline model there are 28 states, that are the variables representing flap, lag, twist angles, and inflow states dynamics plus the anomaly, whereas when dynamic stall is considered 68 states are necessary, that are all the previous ones plus two non–dimensional circulation states for each blade section. The input considered for every model are collective, longitudinal and lateral cyclic.

5.2.1 Unsteady Aerodynamics Complete Unified Model

In section 3.4 was described the mathematical model used for the description of the unsteady aerodynamic, as in section 3.3 the equations for the main rotor dynamics were presented. The coupling of these model present some problems. In fact for the

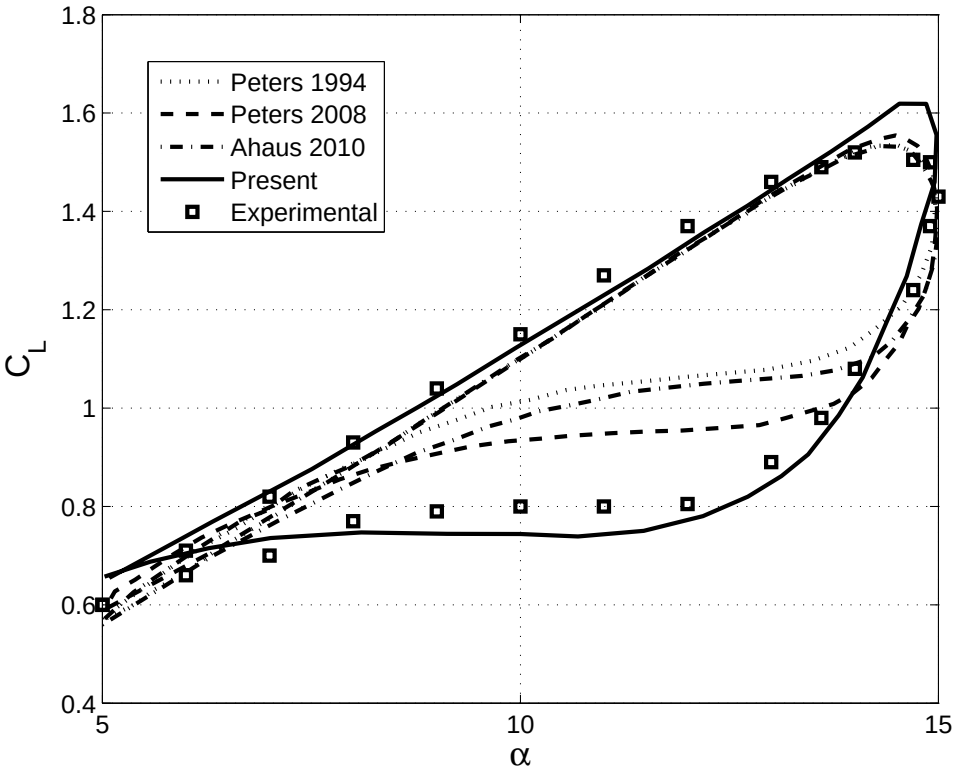

Figure 5.1: Comparison between $C_L - \alpha$ curves obtained using the parameters defined in Tab. 5.1 for $k = 0.1$

description of the aerodynamic loads is necessary the second time derivative of the angle of attack, but this information is not analytically achievable from the rotor dynamic. In order to estimate this derivative, guaranteeing a sufficient accuracy, but without increasing excessively the computational cost, it was approximate using a Taylor series stopped at the second order, thus

$$\alpha(t_{k-2}) = \alpha(t_k) - 2\Delta t\dot{\alpha}(t_k) - \frac{(2\Delta t)^2}{2}\ddot{\alpha}(t_k) \tag{5.2}$$

$$\alpha(t_{k-1}) = \alpha(t_k) - \Delta t\dot{\alpha}(t_k) - \frac{(\Delta t)^2}{2}\ddot{\alpha}(t_k) \tag{5.3}$$

where $\Delta t = t_k - t_{k-1} = 0.5(t_k - t_{k-2})$. Rearranging the expressions above it can be obtained

$$\dot{\alpha}(t_k) = \frac{3\alpha(t_k) - 4\alpha(t_{k-1}) + \alpha(t_{k-2})}{2\Delta t} \tag{5.4}$$

$$\ddot{\alpha}(t_k) = \frac{\alpha(t_k) - 2\alpha(t_{k-1}) + \alpha(t_{k-2})}{(\Delta t)^2} \tag{5.5}$$

Usually the Δt used for the integration is small, (order of magnitude of $10^{-3}s$, and in such cases the expression for $\ddot{\alpha}$ of Eq. 5.5 could lead to numerical errors, thus it is more convenient to save the actual values of the first derivative and use an expression similar to Eq. 5.4

$$\ddot{\alpha}(t_k) = \frac{3\dot{\alpha}(t_k) - 4\dot{\alpha}(t_{k-1}) + \dot{\alpha}(t_{k-2})}{2\Delta t} \tag{5.6}$$

Implementing the unsteady aerodynamic loads there are also other derivatives that should be taken into account, that are the first and second derivatives of the flap angle and the first derivatives of the velocity components on the blade section, but the computation of these derivatives requires the aerodynamic loads obtained. First the blade speed components time derivatives were expressed as a function of the state states and their derivatives, thus

$$\begin{aligned}
\dot{\boldsymbol{v}}_{BL} &= \dot{L}_{BL,R}\boldsymbol{v}_R^{BL} + L_{BL,R}\dot{\boldsymbol{v}}_R^{BL} = \\
&= \dot{L}_{BL,R}\boldsymbol{v}_R^{BL} + L_{BL,R}\left(\dot{\boldsymbol{v}}_R + \dot{\boldsymbol{\omega}}_R \times \boldsymbol{r}_R^{R,BL} + \boldsymbol{\omega}_R \times \dot{\boldsymbol{r}}_R^{R,BL} + \ddot{\boldsymbol{r}}_R^{R,BL}\right) = \\
&= \dot{L}_{BL,R}\boldsymbol{v}_R^{BL} + L_{BL,R}\left(\dot{L}_{RS}\boldsymbol{v}_S + L_{RS}\dot{\boldsymbol{v}}_S + \left(\dot{L}_{RS}\boldsymbol{\omega}_S + L_{RS}\dot{\boldsymbol{\omega}}_S\right) \times \boldsymbol{r}_R^{R,BL} + \right. \\
&\quad \left. + \boldsymbol{\omega}_R \times \left(\dot{L}_{R,BL}\boldsymbol{r}_H^T\right) + \ddot{L}_{R,BL}\boldsymbol{r}_H^T\right)
\end{aligned} \tag{5.7}$$

where $\dot{L}_{BL,R}$ and $\ddot{L}_{BL,R}$ are function of $\dot{\beta}$, $\dot{\zeta}$, $\ddot{\beta}$, and $\ddot{\zeta}$, while $\dot{L}_{RS}$ depends on Ω (see Appendix A). When only the rotor is considered, this manipulation lead to a dependency of the unsteady aerodynamic loads only on the first two time derivatives of flap and lag and on the dynamic of the angle of attack. During the integration step the first derivatives hare included in the state vector, the only problem is on the computation of the second time derivatives. All the aerodynamic loads can be expressed as

$$C = \tilde{C} + \Delta C_\beta \ddot{\beta} + \Delta C_\zeta \ddot{\zeta} \tag{5.8}$$

thus, for each blade, the flap, lag, and circulation derivatives expressions B.44,B.45, and 3.73 can also be rearranged as

$$\ddot{\beta} = \tilde{\boldsymbol{b}}_\beta + \Delta \boldsymbol{b}_\beta^\beta \ddot{\beta} + \Delta \boldsymbol{b}_\zeta^\beta \ddot{\zeta} \tag{5.9}$$

$$\ddot{\zeta} = \tilde{\boldsymbol{b}}_\zeta + \Delta \boldsymbol{b}_\beta^\zeta \ddot{\beta} + \Delta \boldsymbol{b}_\beta^\zeta \ddot{\zeta} \tag{5.10}$$

$$\ddot{\Gamma} = \tilde{\boldsymbol{b}}_\Gamma + \Delta \boldsymbol{b}_\beta^\Gamma \ddot{\beta} + \Delta \boldsymbol{b}_\zeta^\Gamma \ddot{\zeta} \tag{5.11}$$

These equations could then be rewritten as

$$\boldsymbol{M}_{DS} \left\{ \begin{array}{c} \ddot{\beta} \\ \ddot{\zeta} \\ \ddot{\Gamma} \end{array} \right\} = \left\{ \begin{array}{c} \tilde{\boldsymbol{b}}_\beta \\ \tilde{\boldsymbol{b}}_\zeta \\ \tilde{\boldsymbol{b}}_\Gamma \end{array} \right\} \tag{5.12}$$

Solved this equation the aerodynamic load coefficient for each blade can be computed from 5.8. Once the coefficients are obtained the rotor aerodynamic loads can be derived, thus all the state derivatives can be integrated.

The finite state method for unsteady aerodynamics implemented appear to have problems when the incidence on the blade has a dynamic different from a sinusoid. That is the case of the first sections, when the speed on the blade change abruptly, and so does the angle of attack. When the helicopter forward speed is greater than 40 m/s the first and second time derivatives of the angle of attack reach very high values, leading to an instability of the theory. The unsteady aerodynamic theory was considered valid for $-18° \leq \alpha \leq 18°$ and $-458°/s \leq \dot{\alpha} \leq 458°/s$, and outside this range the quasi–steady theory was implemented.

5.3 Simplifying assumptions considered

5.3.1 Approximation of the derivatives

The addition of the unsteady aerodynamic and dynamic stall is obviously computational costly. One of the most expensive operation during the simulation is the inversion of the matrix 5.12. In order to avoid this, each blade second time derivatives of flap and lag angles can be approximate using the same methods described for the angle of attack (Eq. 5.6). The first time derivative at the current integration time step is already supplied in the steady state vector, while its values at the previous two time steps are saved in the output vector, thus the second time derivatives could be calculated as

$$\ddot{\beta}(t_k) = \frac{3\dot{\beta}(t_k) - 4\dot{\beta}(t_{k-1}) + \dot{\beta}(t_{k-2})}{2\Delta t} \tag{5.13}$$

$$\ddot{\zeta}(t_k) = \frac{3\dot{\zeta}(t_k) - 4\dot{\zeta}(t_{k-1}) + \dot{\zeta}(t_{k-2})}{2\Delta t} \tag{5.14}$$

5.3.2 Harmonic Truncation

Another simplification considered stems from the idea that the local angle of attack, the angle of flap, and the velocity, in the range of validity of the model, has a oscillating behavior, that is basically function of the forward speed reached by the helicopter and the position of the blade element with respect to the non–rotating frame. Thus the values of α, β, and V for each blade section used to calculate the aerodynamic loads can be truncated at the first harmonic, obtaining the following

approximated expression

$$\alpha_i = \alpha_{0i} + \alpha_{1i} \sin(\Omega t + \bar{\Psi}) \tag{5.15}$$
$$\beta = \beta_0 + \beta_1 \sin(\Omega t + \bar{\Psi}) \tag{5.16}$$
$$V_i = V_{0i} + V_{1i} \sin(\Omega t + \bar{\Psi}) \tag{5.17}$$

where i is the section considered, $\bar{\Psi}$ is the delay with respect to the reference blade, α_{0i}, α_{1i}, β_0, β_1, V_{0i}, and V_{1i} can be determined from look–up tables as function of V_S and the longitudinal and lateral commands. Once this approximated is used, it is straightforward to evaluate their first and second derivatives:

$$\dot{\alpha_i} = \alpha_{1i}\Omega \cos(\Omega t + \bar{\Psi}) \tag{5.18}$$
$$\ddot{\alpha} = -\alpha_{1i}\Omega^2 \sin(\Omega t + \bar{\Psi}) \tag{5.19}$$
$$\dot{\beta} = \beta_1 \Omega \cos(\Omega t + \bar{\Psi}) \tag{5.20}$$
$$\ddot{\beta} = -\beta_1 \Omega^2 \sin(\Omega t + \bar{\Psi}) \tag{5.21}$$
$$\dot{V} = V_{1i}\Omega \cos(\Omega t + \bar{\Psi}) \tag{5.22}$$

Substituting the expression of Eq. 5.15–5.22 into Eq. 3.73 allows for the definition of the non–dimensional circulation Γ_2 derivative as a function of time and of the coefficients α_{0i}, α_{1i}, β_0, β_1, V_{0i}, and V_{1i}. Expressing the non–dimensional circulation in harmonic form

$$\Gamma_{2i} = \Gamma_{0i} + \Gamma_{si} \sin(\Omega t + \bar{\Psi}) + \Gamma_{ci} \cos(\Omega t + \bar{\Psi}) \tag{5.23}$$

the coefficients Γ_{0i}, Γ_{si}, and Γ_{ci} can be obtained easily for each time step, without the need of integration, substituting on the left hand side of equation 3.73. This allows for the reduction of the number of states to be integrated, thus a great save in computational effort.

5.3.3 Comparison

The results obtained here are presented for a speed of V_S =20 m/s, thus the command applied, that are those would be necessary if the whole helicopter is considered, are $\theta_0 = 16°$, $A_{1S} = -1.2°$, and $B_{1S} = 1°$. Fig. 5.2 show the $CL - \alpha$ curve for each of the 5 sections considered for one of the blade (being the result cyclic it is not necessary to present results for each blade). In some of the plots shown also the static case presents a hysteresis that is only due to different Mach number for the same angle of attack. The use of these approximation has guaranteed a good computational time save: the first approximation allow for 17% of time saved with respect to the complete case, while the second one has almost 40% of reduction with respect to the complete case. It is immediately evident how the presence of dynamic

stall influence mostly the sections nearer to the hub (Fig. 5.2.a and 5.2.b) then the external (5.2.e). It should be noted that the step present in Fig. 5.2.a is due to the fact that also for speed so low the limit of validity of the theory is reached. The precision in prediction of the lift coefficient for the two approximation cases is not perfect, but is still good enough to guarantee similar behavior for the state variables as could be seen in the next figures.

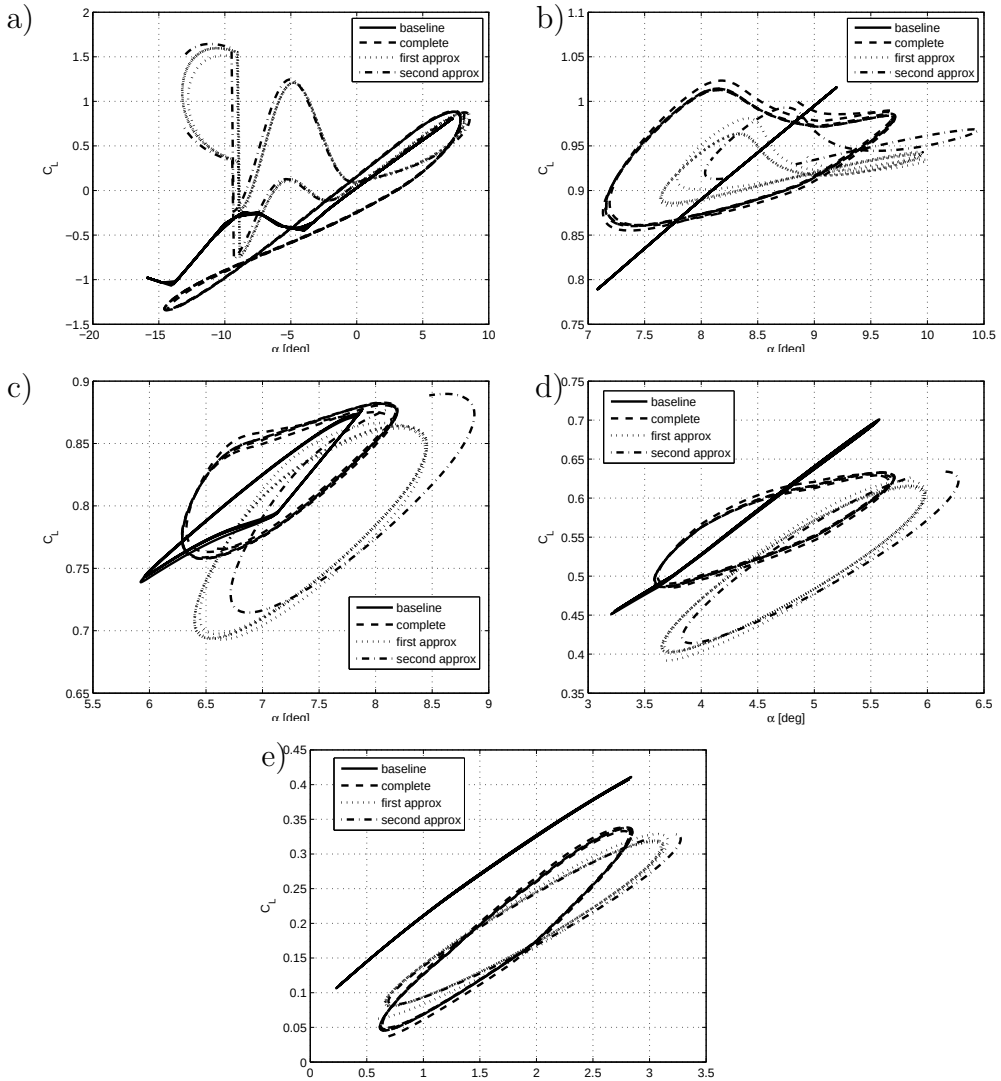

Figure 5.2: $C_L - \alpha$ curves obtained for $V_S = 25.7 m/s$ for each blade section, for the quasi–static C_L (solid line), complete (dash–dotted line), and the two approximate cases (dashed line for the first, dotted the second).

Fig. 5.3 present the comparison between the actual and approximated flap second time derivative obtained in the complete case, and the two approximated cases,

the derivatives approximations and the harmonic truncation, for four different forward speeds, V =0, 20, 40, 60 m/s. This derivative is well represented by both approximations at lower speeds, while for higher velocities the behavior is more complicated and is better represented by the first approximation, while the other capture only the periodicity.

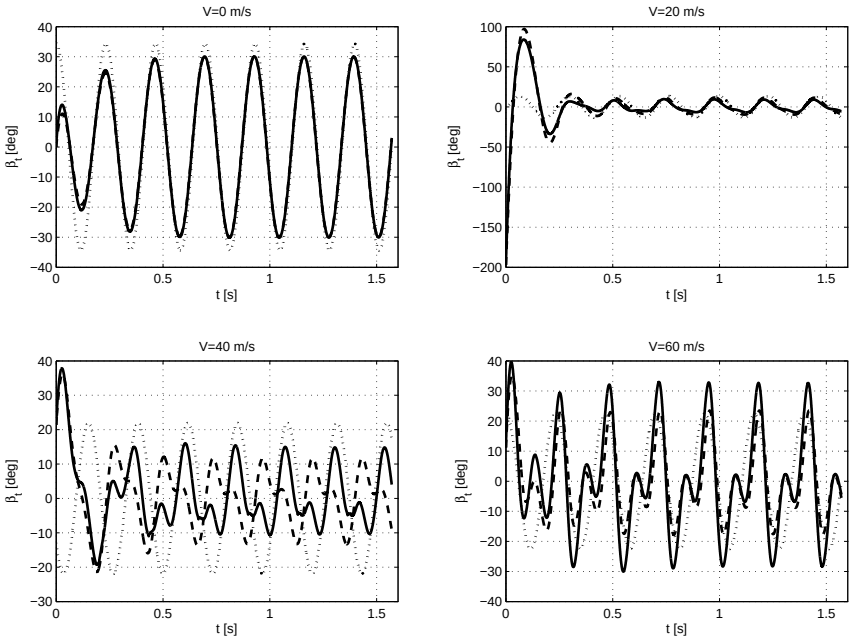

Figure 5.3: Comparison of $\dot{\beta}$ response considering the complete (continue) and two approximate cases.

Figures 5.4 and 5.5 represent the dynamic response of flap angle and angle of attack. It is evident that for fixed speed and controls the harmonic truncation does not present a transient phase to reach the final value, but it follows quite well the behavior of the variables, especially for lower speed.

5.4 Complete Helicopter Results

The model hitherto described was validated comparing the values obtained trimming the complete helicopter model with the results obtained by the baseline model, Flightlab model, and flight tests data. The Flightlab model is developed in [17] and has a similar level of complexity compared to the baseline model developed in [89]. Data from wind–tunnel or flight tests are not easily achievable, because in most cases the information are proprietary. In this work the informations published in [1]

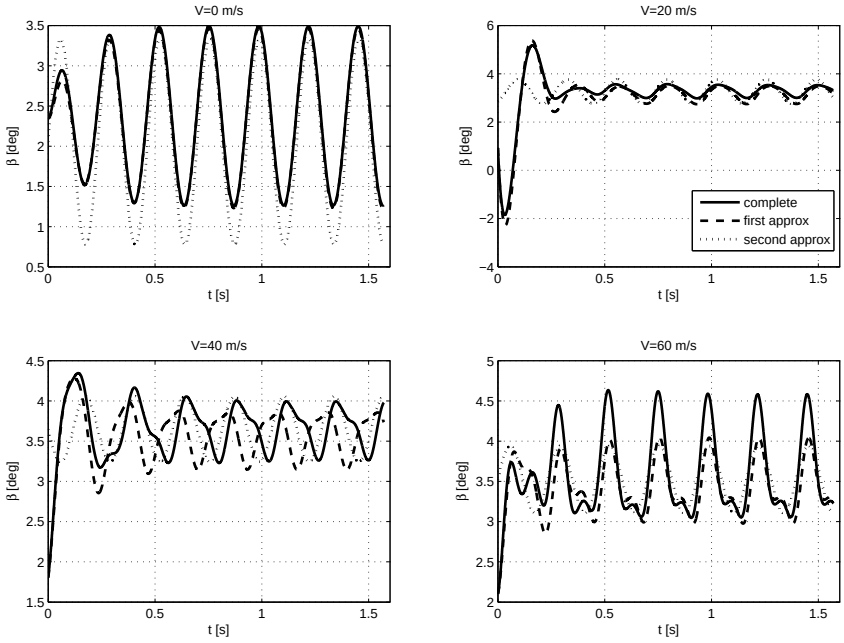

Figure 5.4: Comparison of β response considering the complete (continue) and two approximate cases.

are used for comparison. The trimming conditions for the baseline and unsteady aerodynamics models are derived using the periodic trim for full–order model described in [89]. The configuration considered here presents a 6600 kg mass at about 1600m altitude.

As shown in the previous sections the approximation with α, β, and ζ described with Taylor series gave a good estimate of the derivatives of these variables, so it was chose in the validation of the complete helicopter trim condition. Figures 5.6–5.7 present the comparison between the trim conditions for the commands and the power required in steady flight condition for 4 cases specified before. The value obtained for the commands in the unsteady aerodynamic case seems to be in good agreement with the value from the flight test for lower velocities (in the range 0-40 m/s), getting better results than the baseline and Flightlab cases, but it gets worse for higher speeds.When the unsteady theory is considered the power necessary increase, probably because the value of the drag coefficient is overestimated by the model. The drag coefficient has low effect on the rotor dynamics, while its greater consequence is to increment the power required for the steady flight. The result given by the approximate model are also quite good concerning the commands needed. Regarding the power required it results a little overestimated compared to the baseline or Flightlab results at higher speeds, but lower than the continue line.

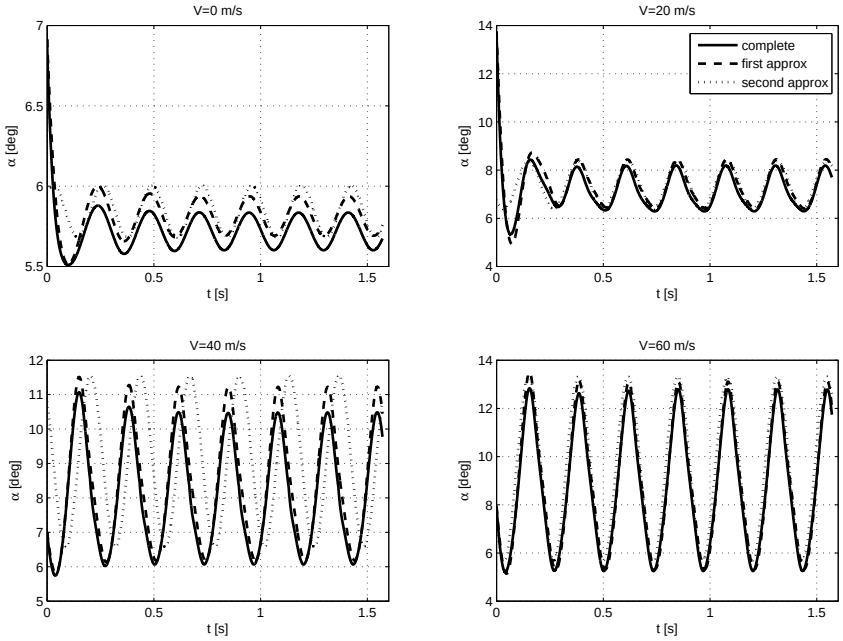

Figure 5.5: Comparison of α response considering the complete (continue) and two approximate cases.

The reason may be found in the rough approximation of the angle of attack and flap angle dynamics in the harmonic truncation case, as discussed in the previous section.

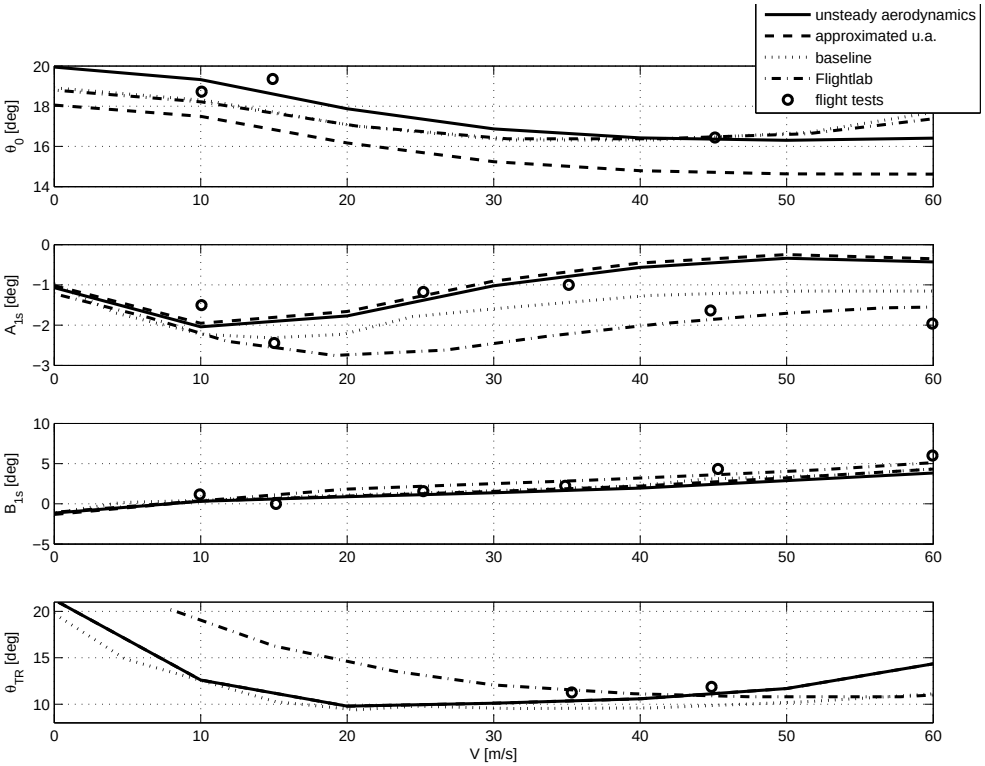

Figure 5.6: UH–60 commands evaluation for unsteady aerodynamics (continue), baseline (dashed), and Flightlab (dotted) models compared to flight tests

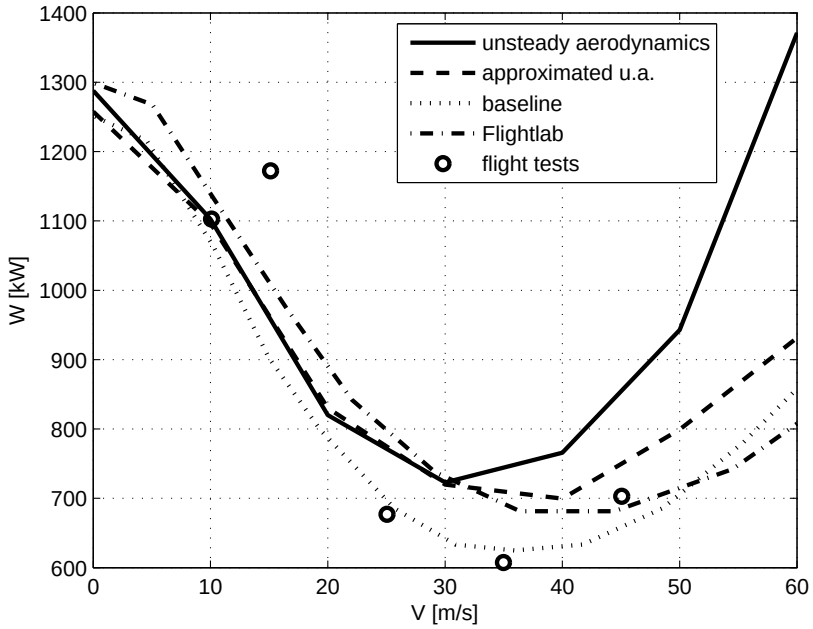

Figure 5.7: UH–60 required power evaluation for unsteady aerodynamics (continue), baseline (dashed), and Flightlab (dotted) models compared to flight tests

Chapter 6

Quadrotor Dynamics

6.1 Agility Potential

6.1.1 Inverse Simulation Algorithm

As anticipated in the Introduction, the IS problem is solved by means of an integration algorithm [16, 33]. When quad-rotor dynamics is expressed in terms of a set of nonlinear ordinary differential equations, it can be represented in compact form as

$$\dot{\boldsymbol{x}} = \boldsymbol{f}(\boldsymbol{x},\boldsymbol{u}) \; ; \quad \boldsymbol{y} = \boldsymbol{g}(\boldsymbol{x}) \tag{6.1}$$

where a dot indicates the time derivative, $\boldsymbol{x} = (\boldsymbol{V}_b^T,\boldsymbol{\omega}_b^T,q_0,$
$\boldsymbol{q}^T,\boldsymbol{r}^T)^T \in \mathbb{R}^n$ is the state vector (with $n = 13$), $\boldsymbol{u} = (u_1,u_2,u_3,u_4,w_1,w_2,w_3)^T \in \mathbb{R}^m$ is the vector of $m = 7$ control variables presented in the previous paragraph for this unconventional configuration. Finally $\boldsymbol{y} \in \mathbb{R}^p$ is the vector of tracked output variables.

Once a desired variation with time of the output, $\boldsymbol{y}_{des}(t)$, is available, equations of motion are integrated from an initial condition $\boldsymbol{x}_I = \boldsymbol{x}_k$ at time t_k over a time interval Δt for a piece-wise constant value $\boldsymbol{u}_k^\star$ of the control variables. The resulting value $\boldsymbol{y}_F = \boldsymbol{g}(\boldsymbol{x}_F)$ of the output variables at time $t_F = t_{k+1} = t_k + \Delta t$ is thus a function of the (given) initial state $\boldsymbol{x}_k$ and of the (unknown) constant control action, $\boldsymbol{u}_k^\star$.

Control variables can then be determined in such a way that $\boldsymbol{y}_F$ matches the value of $\boldsymbol{y}_{des}$ at time t_F, that is, the inverse problem can be stated in terms of a set of p algebraic equations in the form

$$\boldsymbol{y}_F = \boldsymbol{F}(\boldsymbol{x}_k,\boldsymbol{u}_k^\star) = \boldsymbol{y}_{des}(t_F) \tag{6.2}$$

with m unknowns. When $m = p$, the problem is nominal and, if well posed, it can be solved by means of standard numerical techniques, such as Newton-Raphson

(NR) method, [33]. If $m > p$ the problem is redundant, as in many aeronautical applications for fixed and rotary-wing aircraft. When the redundancy degree is $m - p = 1$, as for the conventional quad-rotor, where $\boldsymbol{u} = (u_1,u_2,u_3,u_4)^T \in \mathbb{R}^4$, one additional constraint is sufficient for making the problem nominal, where a desired value of a relevant parameter can be enforced in order to obtain trajectories with an additional desired feature (*e.g.* zero lateral acceleration or zero sideslip).

In the present case, the presence of 3 additional degrees of freedom makes the system highly redundant. This marks a major difference between the standard and the novel configuration, where the conventional quad-rotor features four controls that are used to track three desired trajectory variables plus an additional constraint. The resulting nominal inverse simulation problem is solved using a Newton-Raphson algorithm. Conversely, the novel configuration features 7 control variables and this requires a different approach for the solution of the inverse problem.

In [33] was proposed a solution method for redundant problems based on the use of the so-called Moore-Penrose pseudo-inverse during NR iterations, which results into the minimum-norm control vector that solves the problem. A more general approach was proposed in [16], where an optimization problem is solved in order to enforce, together with the constraints on trajectory variables, relevant properties to the inverse solution by defining a suitable merit function to be minimized locally at each time step of the inverse simulation. In the present case, the inverse simulation step is solved using a sequential programming (SQP) numerical optimization algorithm that, in addition to the constraints defined as for the conventional configuration, also minimizes the control effort on command variables u_2, u_3 and u_4, and deviations from desired values for roll and pitch angles.

A further problem with aeronautical applications of IS integration methods is represented by undesirable oscillations in the control action or even instabilities in the inverse solution, discussed in some details in [51, 52, 87, 97], that may be due to uncontrolled states and/or numerical issues in the evaluation of the output Jacobian matrix $\boldsymbol{J} = \partial \boldsymbol{y}_F / \partial \boldsymbol{u}_k^\star$. These issues can be circumvented, at the cost of increasing the computational burden, by solving the inverse problem stated by Eq. (6.2) over a longer time-horizon, that is, choosing $t_F^\star = t_k + N\Delta t > t_{k+1}$, that is, the piece-wise constant control action is propagated for a longer time interval in order to allow for uncontrolled dynamics to settle down. The initial condition $\boldsymbol{x}_{k+1}$ for the next step is then evaluated at time t_{k+1}, as in [16].

As a variation to a standard integration method, a different definition of the algebraic system is adopted in this paper, where, rather than solving Eq. (6.2) in terms of the actual value of the tracked variables at time t_F, their increments over the time step between t_I and $t_F^\star$ are required to be equal. Equation (6.2) is thus

replaced with

$$\begin{aligned} \Delta \boldsymbol{y} &= \boldsymbol{F}(\boldsymbol{x}_k, \boldsymbol{u}_k^\star) - \boldsymbol{g}(\boldsymbol{x}_k) = \\ &= \boldsymbol{y}_{des}(t_F) - \boldsymbol{y}_{des}(t_I) + K\left[\boldsymbol{y}_{des}(t_I) - \boldsymbol{g}(\boldsymbol{x}_k)\right] \end{aligned} \tag{6.3}$$

where the additional term in square brackets multiplied by a gain K avoids that the actual solution "drifts" away from the desired path because of the incomplete implementation of the considered step during the forward propagation, as outlined above. This term also enforces asymptotic convergence on the tracked variables when they achieve a steady value. By some simple manipulation, Eq. (6.3) can be rearranged as

$$\boldsymbol{F}(\boldsymbol{x}_k, \boldsymbol{u}_k^\star) = \boldsymbol{y}_{des}(t_F) + (K-1)\left[\boldsymbol{y}_{des}(t_I) - \boldsymbol{g}(\boldsymbol{x}_k)\right] \tag{6.4}$$

where for $K = 0$ the additional term disappears and one simply requires that the increment of the actual output variables at the end of the whole inverse simulation step $\Delta t = t_F - t_I$ equals the increment for the desired variation of $\boldsymbol{y}$, whereas for $K = 1$ the original formulation of Eq. (6.2) for the inverse problem is recovered.

This is the most general inverse simulation scheme implemented, unless otherwise stated. Only for the last test case a few difference will be pointed out when discussing the results for the roll tilt maneuver.

6.1.2 MPC algorithm

A Model Predictive Control (MPC) algorithm already used in [89] was also implemented when a more complex model is available. The MPC scheme for the solution of inverse simulation problem allows the use of the low–order model defined before to calculate the inverse problem, while the higher–order model is implemented to propagate forward in time. This allows a better accuracy than the inverse simulation problem using only the low–order model, but lower CPU time than using the higher–order one.

The architecture of the MPC–IS scheme used is described in Fig. 6.1. In the forward simulation block the higher–order model is used, while the inverse simulation block evaluates the command increment $\Delta \boldsymbol{u}$ that achieves the desired increment $\Delta \boldsymbol{y}$, solving the optimization problem for the low–order model. The guidance block defines the desired increment $\Delta \boldsymbol{y}$, defined similarly to what was done in the pure inverse simulation problem. In [89] and [7] it has already been demonstrated the advantages of this method over the pure inverse simulation. The novelty in this case is the application to the quadrotor model developed in [24], where it was necessary to transform the input from one model to the other. The model described in section 3.5 consider the change in rotor speed for the 4 rotors as thrust control while the

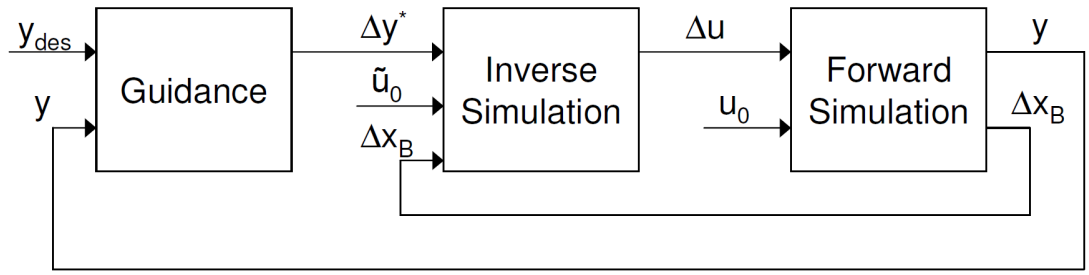

Figure 6.1: MPC–IS scheme [89].

higher–order model of [24] uses constant speed, variable pitch propellers. The low–order model was then modified so that the commands u_i,$i = 1, \ldots 4$ define a variation in thrust and torque, but not on rotor speed. The input for the high–order model becomes then the desired thrust value, from which the pitch value is then evaluated.

6.2 Results

Geometrical characteristics and other model parameters used for describing quadrotor dynamics are summarized in Table 6.1.

Table 6.1: Quadrotor data

Data	Symbol	Value	Unit
Mass	m	0.941	kg
Rotor radius	R	0.127	m
Rotor distance from c.g.	b	0.465	m
Height	h	0.08	m
Width	d	0.1	m
Inertia moments	$J_{xx} = J_{yy}$	0.0121	kg m^2
	J_{zz}	0.0018	kg m^2
Rotor rate at hovering	Ω_0	382.06	rad/s
Thrust constant	k_t	$1.581 \cdot 10^{-5}$	-
Torque constant	k_c	$4.16 \cdot 10^{-7}$	-

The inverse simulation algorithm is tested on 3 different maneuvers: a U turn, a 360° yaw turn in straight flight, and a 90° roll tilt in forward flight. Table 6.2 summarizes data used to define the test cases. All the maneuvers start from a

hovering condition, so that an initial acceleration is always included. A graphical representation of the desired variation of the most relevant tracked outputs for the three maneuvers are reported in Figs. 6.2-6.4.

Table 6.2: Test cases characteristics

Test case	Duration	Tracked outputs
U turn	16s	$V_{x,d}$,$V_{y,d}$
360° yaw turn	22 s	r,$V_{x,d}$
90° roll tilt	20 s	ϕ,$V_{x,d}$

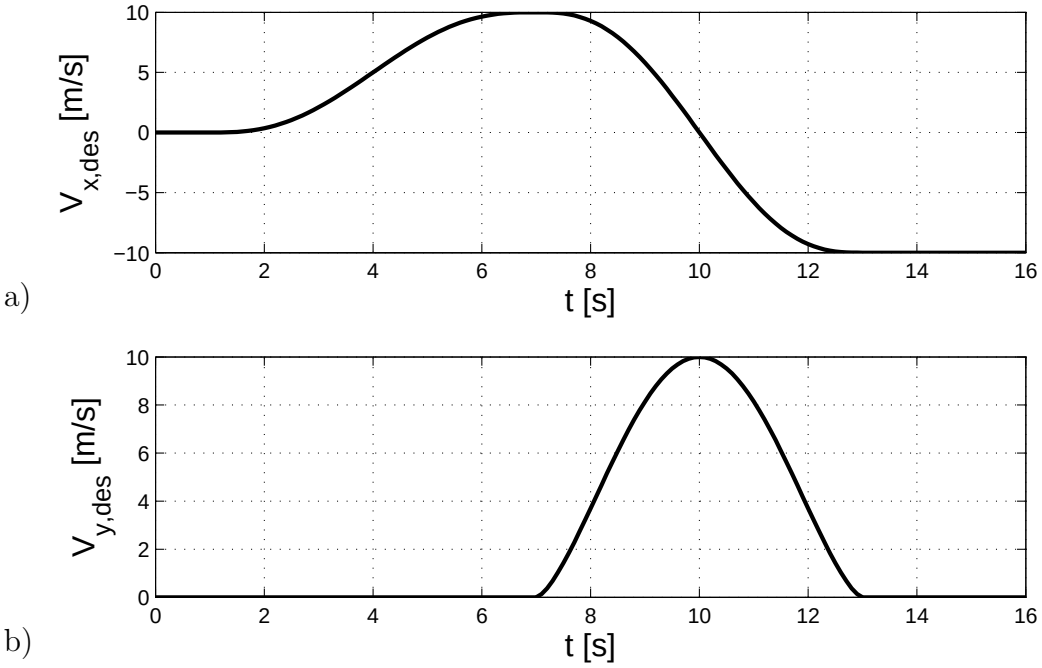

Figure 6.2: U-turn: desired x (a) and y (b) inertial speed.

For the first two test cases the results obtained for the tilting rotor configuration are compared with those of a standard configuration. The third maneuver cannot be tracked by a conventional quad-rotor, which is thus not considered. For all the maneuvers the inverse simulation algorithm determines a piece-wise constant control over a time step $\Delta t = 0.1$ s, but the inverse problem is solved over a longer interval, $N\Delta t = 0.2$ s.

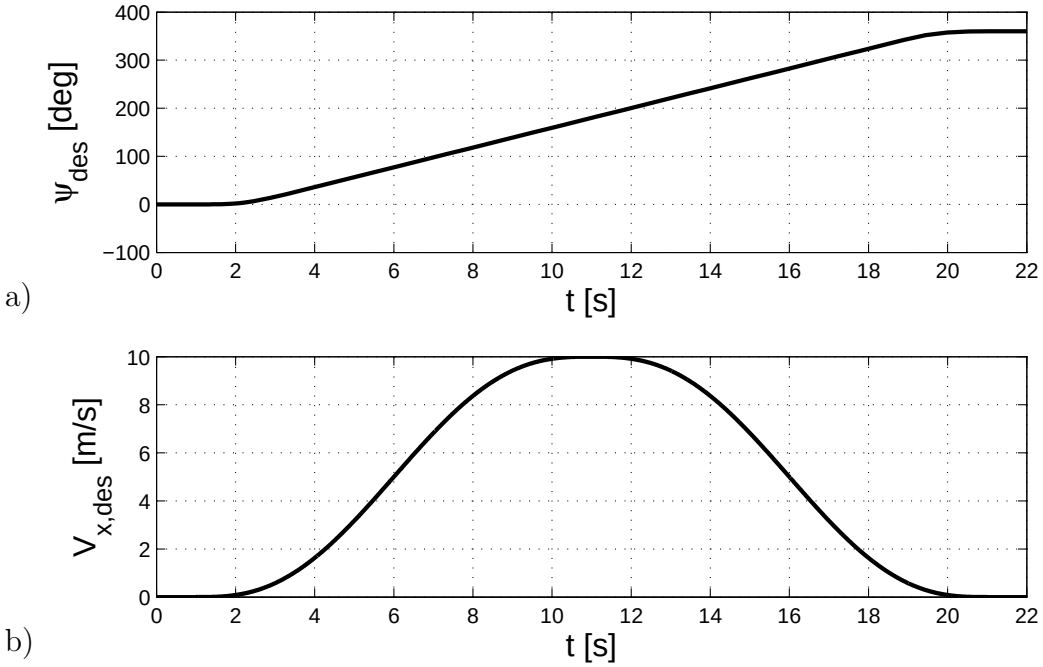

a)

b)

Figure 6.3: Yaw rotation: desired ψ (a) and x inertial speed (b).

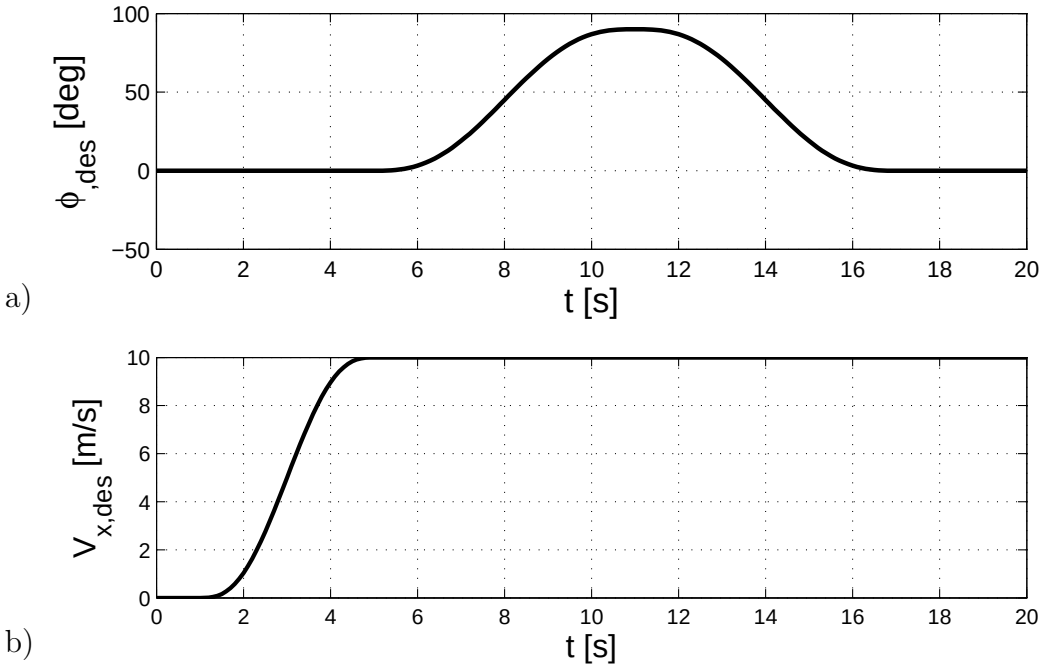

a)

b)

Figure 6.4: Roll tilt: desired ϕ (a) and x inertial speed (b).

6.2.1 U turn maneuver

The first maneuver is a U turn starting from hover. The quad-rotor initially accelerates in the x inertial direction, then it reverts its direction of flight. The desired variation of V_x velocity is obtained using a fifth order polynomial in order to have C^2 continuity at the bounds of the time intervals in which the maneuver is divided (acceleration, turn, forward flight in the reverse direction), whereas V_y is kept equal to zero during the acceleration and final straight flight:

$$
\begin{aligned}
&t < 1, \qquad V_{x,d} = 0, V_{y,d} = 0 \\
&1 < t < T/2, \;\; V_{x,d} = \tilde{V}\left(10\tau^3 - 15\tau^4 + 6\tau^5\right), V_{y,d} = 0 \\
&T/2 < t < T-1, \\
&\quad V_{x,d} = \tilde{V}\left(63 - 240\tau + 360\tau^2 - 260\tau^3 + 90\tau^4 - 12\tau^5\right) \\
&\quad V_y = (\tilde{V}^2 - V_x^2)^{-1/2} \\
&t > T-1, \qquad V_{x,d} = -\tilde{V}, V_{y,d} = 0
\end{aligned}
$$

where τ is the nondimensional time

$$\tau = 2\frac{t-1}{T-2} \tag{6.5}$$

and T is the total simulation time. During the whole maneuver the sideslip angle is maintained as small as possible.

Figures 6.5 to 6.9 show the results for this test case. The variation of inertial speed components (V_x,V_y, and V_z) are presented in figure 6.5. Velocity components in the horizontal plane are tracked with acceptable errors by both the conventional quad-rotor and the configuration with tilting rotors. Conversely, the speed component along the vertical (z) axis presents more significant errors when the conventional configuration is considered. In figure 6.6 the sideslip velocity (v) is shown. It is evident that, during the maneuver, the novel configuration does not maintain the desired zero-sideslip condition with the same accuracy achieved by the standard quad-rotor. This is a side effect of the local optimization process, where pitch and roll angle (θ and ϕ, shown in Fig. 6.7), are kept as small as possible, together with u_2, u_3, and u_4 control variables. When the quad-rotor performs a flat turn with $\phi \approx 0$, a perfectly zero-sideslip condition cannot be maintained. When minor variations of the roll angle are allowed, the sideslip angle drops back almost exactly to zero.

Figure 6.8 represents the variation of commands on rotor angular speed, u_i, $i = 1,2,3,4$, as defined in eq. (3.91). As expected, these commands are significantly smaller when tilting rotor are employed. Only the collective rotor speed command is significantly different from zero. Figure 6.9 shows rotors tilt angles for the tilting

rotor case. Large variations of rotor inclination take the place of quad-rotor attitude angles, a feature that potentially increases the effectiveness of the novel configuration for observation of targets on the ground, provided that a camera mounted on the vehicle would not undergo large rotations associated to vehicle maneuver state.

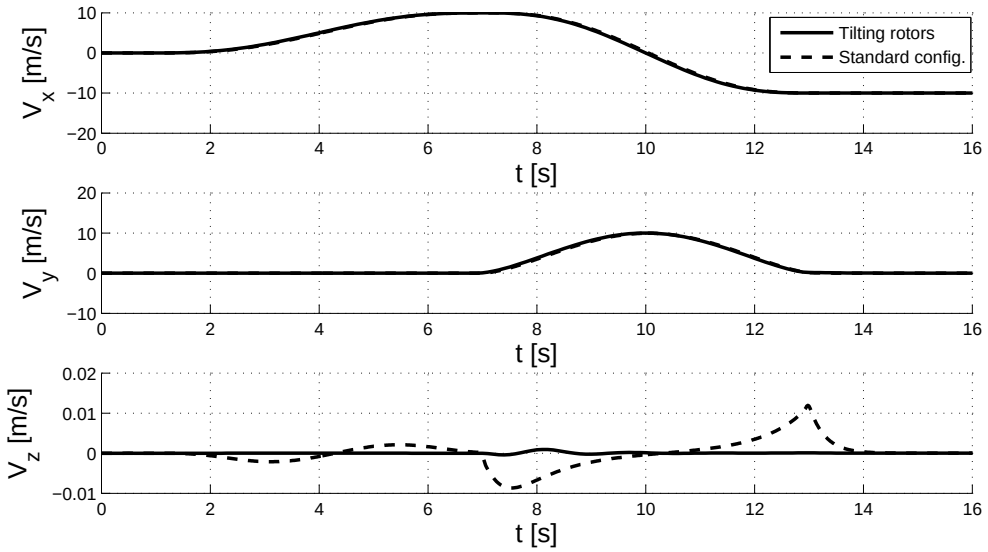

Figure 6.5: Inertial speeds for the U turn maneuver, comparison between the standard case (dashed line) and the tilting rotor configuration (solid line)

6.2.2 360° yaw turn straight flight

The second maneuver starts again from hover. The quad-rotor is required to increase its speed along the inertial x direction, during the first half of a full 360° yaw rotation, while it must decelerate back to hover while completing the second half of the rotation. In this maneuver the controlled variables are the longitudinal inertial speed component V_x and the yaw rate r. The prescribed variations of these variables

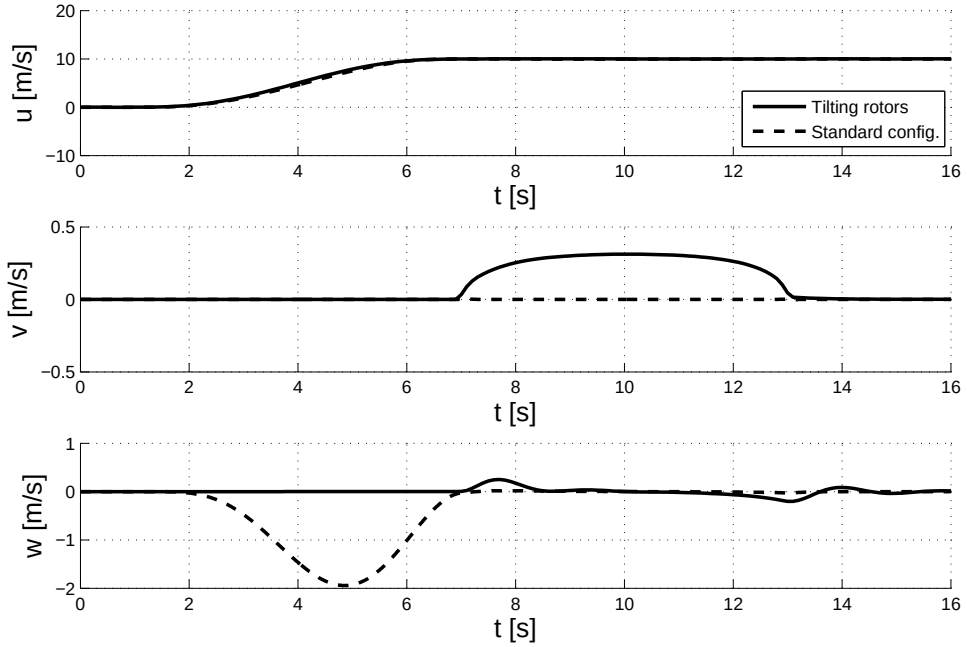

Figure 6.6: Body speeds for the U turn maneuver, comparison between the standard case (dashed line) and the tilting rotor configuration (solid line)

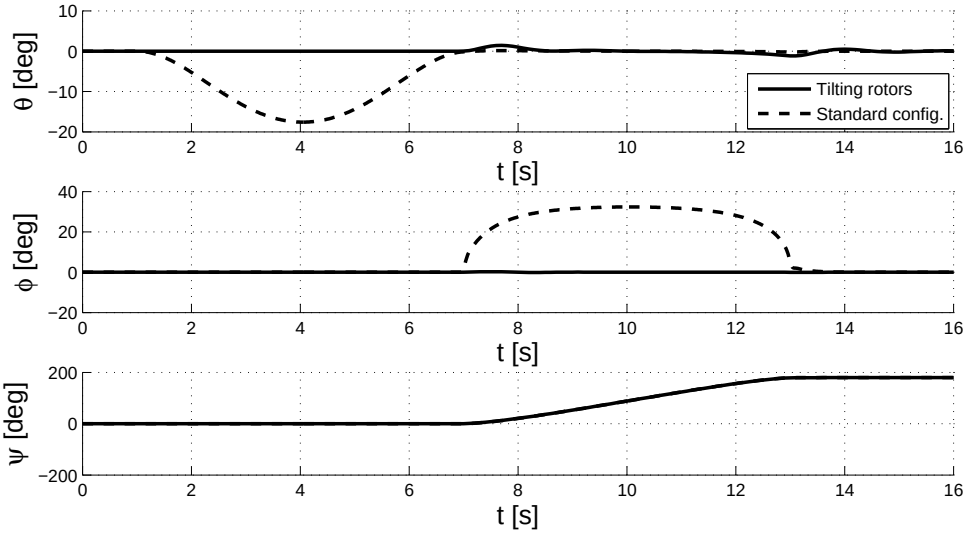

Figure 6.7: Euler angles variation for the U turn maneuver, comparison between the standard case (dashed line) and the tilting rotor configuration (solid line)

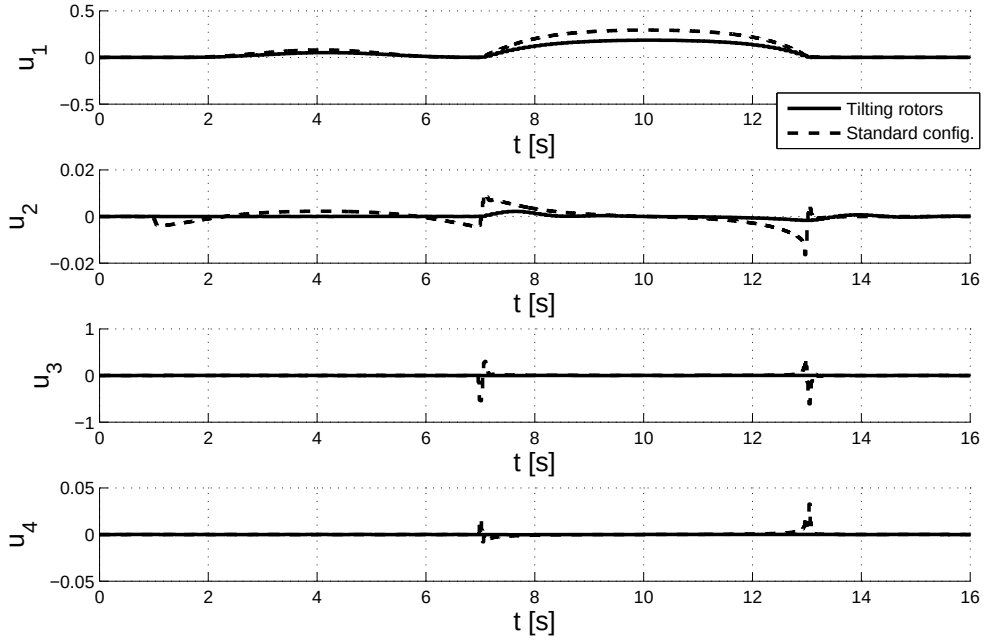

Figure 6.8: Rotor speed commands for the U turn maneuver, comparison between the standard case (dashed line) and the tilting rotor configuration (solid line)

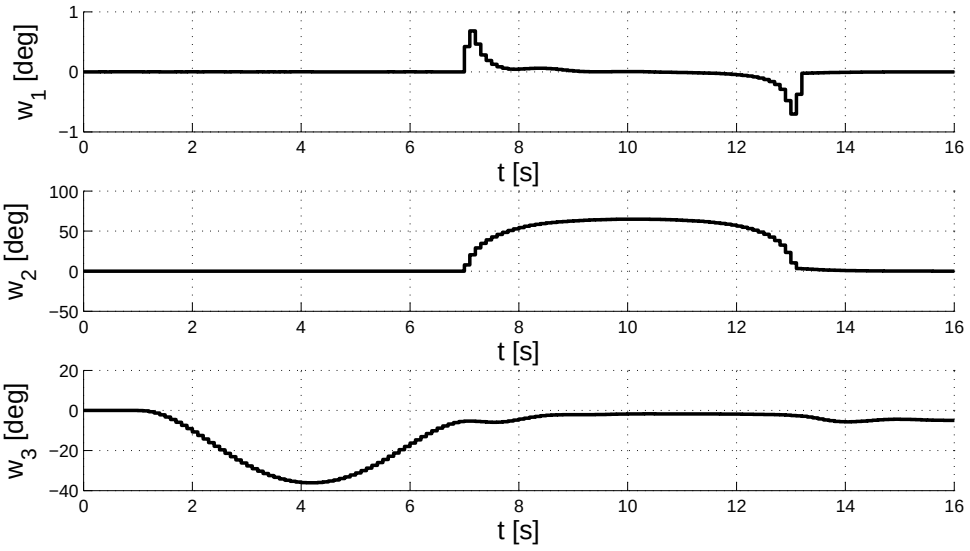

Figure 6.9: Tilting rotors angle command for the U turn maneuver

are

$$
\begin{aligned}
&t < 1, \qquad V_{x,d} = 0, \;\; r_d = 0 \\
&1 \le t < T/8, \;\; V_{x,d} = \tilde{V}\left(10\tau^3 - 15\tau^4 + 6\tau^5\right) \\
&\qquad\qquad r_d = \tilde{r}\left(640\tau^3 - 3840\tau^4 + 6144\tau^5\right) \\
&1 < t < T/2, \;\; V_{x,d} = \tilde{V}\left(10\tau^3 - 15\tau^4 + 6\tau^5\right) \\
&\qquad\qquad r_d = \tilde{r} \\
&T/2 < t < 7T/8 \\
&\quad V_{x,d} = \tilde{V}\left(32 - 120\tau + 180\tau^2 - 130\tau^3 + 45\tau^4 - 6\tau^5\right) \\
&\quad r_d = \tilde{r} \\
&T/8 < t < T/1 \\
&\quad V_{x,d} = \tilde{V}\left(32 - 120\tau + 180\tau^2 - 130\tau^3 + 45\tau^4 - 6\tau^5\right)
\end{aligned}
$$

where τ is defined as in eq. (6.5) and $T = 22s$.

Figures 6.10 to 6.13 present vehicle response and commands. Desired velocity and yaw angle are tracked by both quad-rotor models, but roll and pitch angles exhibit an undesired oscillatory response for the standard configuration. Vertical inertial speed component remain close to zero in both cases, whereas lateral deviations are more significant when the novel configuration is adopted, but this is the cost associated to keeping roll and pitch attitude close to zero, in order to maintain an almost perfectly horizontal attitude during the yaw rotation.

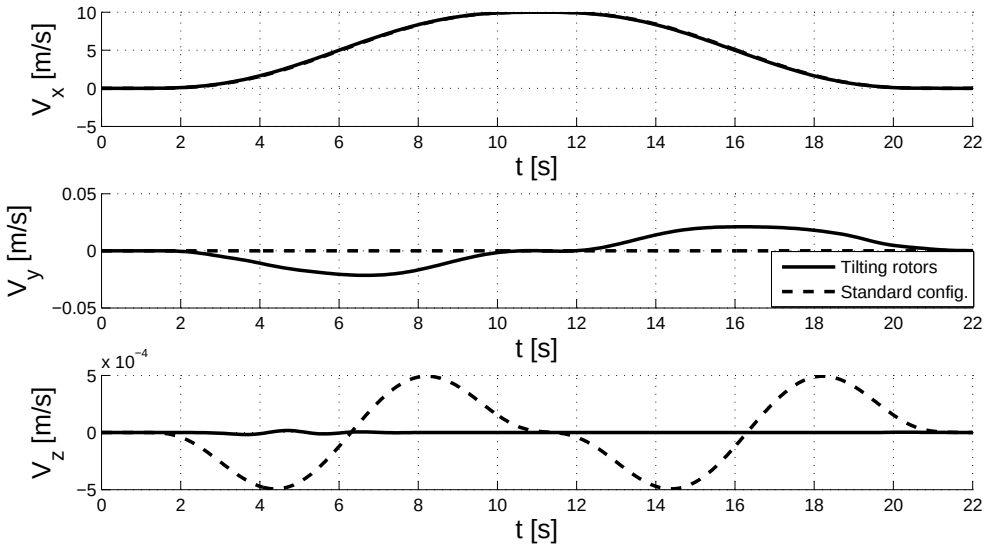

Figure 6.10: Inertial speed for the 360° yaw turn maneuver, comparison between the standard case (dashed line) and the tilting rotor configuration (solid line)

Note that the yaw command needed to perform a complete yaw rotation are small for both models (see u_4 control for the standard configuration in Fig. 6.12 and command w_1 for the quad-rotor with tilting rotors case in Fig. 6.13). This is due to two different reasons. On one side a low-speed maneuver is considered where aerodynamic drag and moments remain small. At the same time, no aerodynamic force in the rotor plane is included in this simple model, where rotors develop only a thrust component in the direction normal to the rotor disk. This means that aerodynamic yaw damping moments are largely underestimated.

6.2.3 90° roll tilt

The third maneuver demonstrates a maneuver capability that is simply unachievable for a conventional quad-rotor. For this reason, only the tilting-rotor model is here considered. The longitudinal inertial velocity component V_x is initially incremented

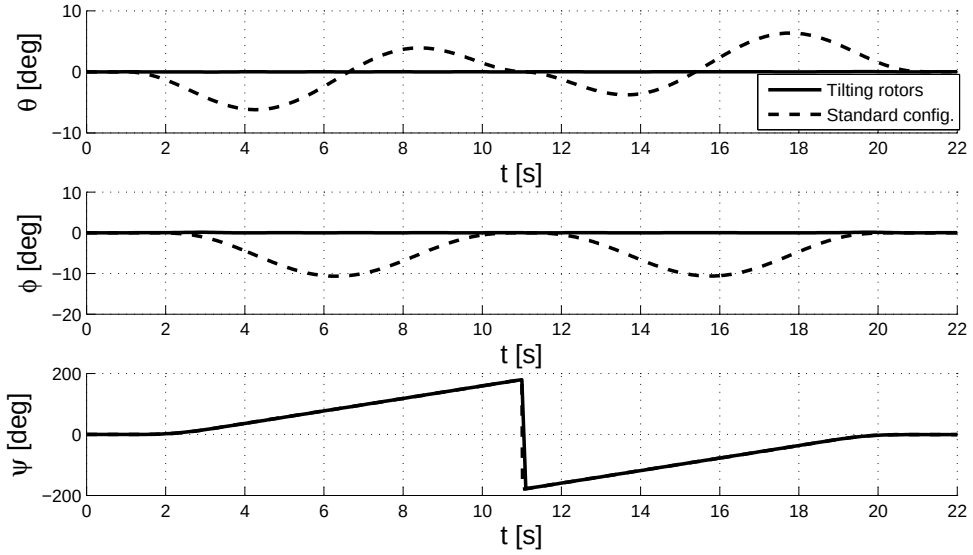

Figure 6.11: Euler angle variations for the 360° yaw turn maneuver, comparison between the standard case (dashed line) and the tilting rotor configuration (solid line)

from hover to a desired value, $\tilde{V}$. Meanwhile the desired roll angle ϕ is incremented from 0 to 90° and then brought back to 0°. This maneuver can be useful when the quad-rotor needs to cross a narrow vertical opening or passage, so that it is necessary to tilt it 90° while flying along a straight trajectory.

Desired inertial velocity and roll angle are defined again using 5th order polynomials:

$$
\begin{aligned}
&t < 1, && V_{x,d} = 0, \;\; \phi_d = 0 \\
&1 < t < T/4, && V_{x,d} = \tilde{V}\left(80\tau^3 - 240\tau^4 + 192\tau^5\right) \\
& && \phi_d = 0 \\
&T/4 \leq t < 5/8T, \; V_{x,d} = \tilde{V} \\
& \quad \phi_d = \tilde{\phi}\left(-6.71 + 49.38\tau - 138.27\tau^2 + 181.73\tau^3 + \right. \\
& \qquad \left. -110.62\tau^4 + 25.28\tau^5\right) \\
&5/8T \leq t < T-1, V_{x,d} = \tilde{V} \\
& \quad \phi_d = \tilde{\phi}\left(240.20 - 790.12\tau + 1027.16\tau^2 - 655.80\tau^3 + \right. \\
& \qquad \left. +205.43\tau^4 - 25.28\tau^5\right) \\
&t > T-1, && V_{x,d} = \tilde{V}, \;\; \phi_d = 0
\end{aligned}
$$

with τ defined as in eq. (6.5), and $T = 20\,\mathrm{s}$.

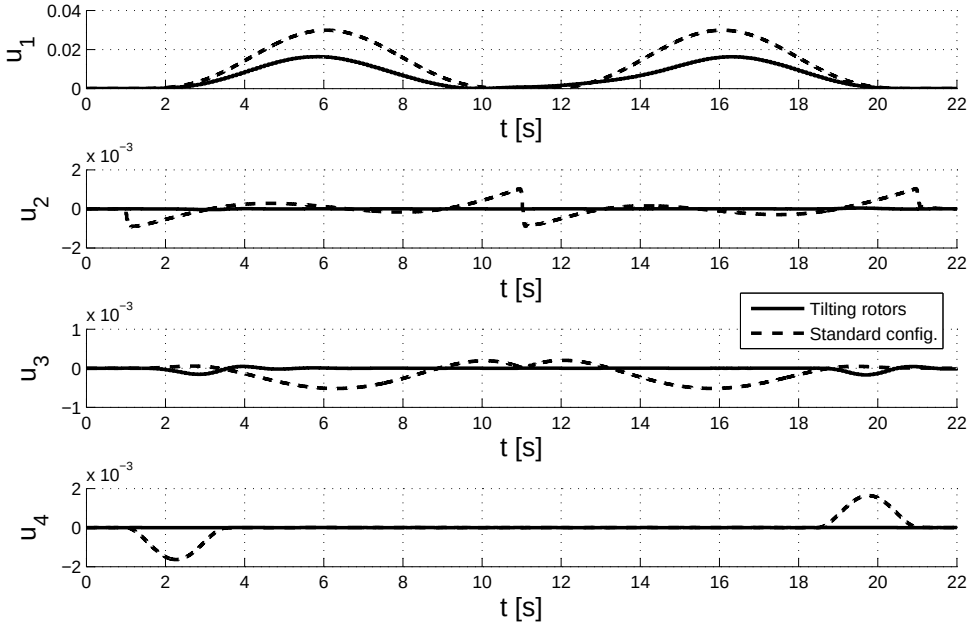

Figure 6.12: Rotor speed command for the 360° yaw turn maneuver, comparison between the standard case (dashed line) and the tilting rotor configuration (solid line)

The inverse simulation algorithm used in this case is slightly different from that used for other maneuvers. Provided that precise tracking of the roll angle is not required, as minor discrepancies in this variable with respect to the desired value would not affect the result, the guidance term in the definition of the desired increment of ϕ was removed. In this case Eq. (6.4) for the roll angle ϕ is thus modified and it is implemented in the form

$$\boldsymbol{F}_{\phi}(\phi_k, \boldsymbol{u}_k^{\star}) = \phi_d(t_F) - \phi_d(t_I) + \boldsymbol{g}(\boldsymbol{x}_k) \tag{6.6}$$

Figures 6.14 to 6.17 present the results obtained for this last case. The vehicle follows the desired inputs, for both velocity and roll angle with satisfactory accuracy (velocity components and roll angle).

The commands needed to perform the maneuver are reported in Figs. 6.16 and 6.17. The variations in rotor angular rates are kept small (Fig. 6.16). Only the "collective" command u_1 is increased when the quad-rotor is completely tilted, which is clearly required by the need for providing enough lift force using only two rotors, in order to maintain the required straight flight condition at constant altitude. As for the other commands on tilt angles (Fig. 6.17), one can note that the

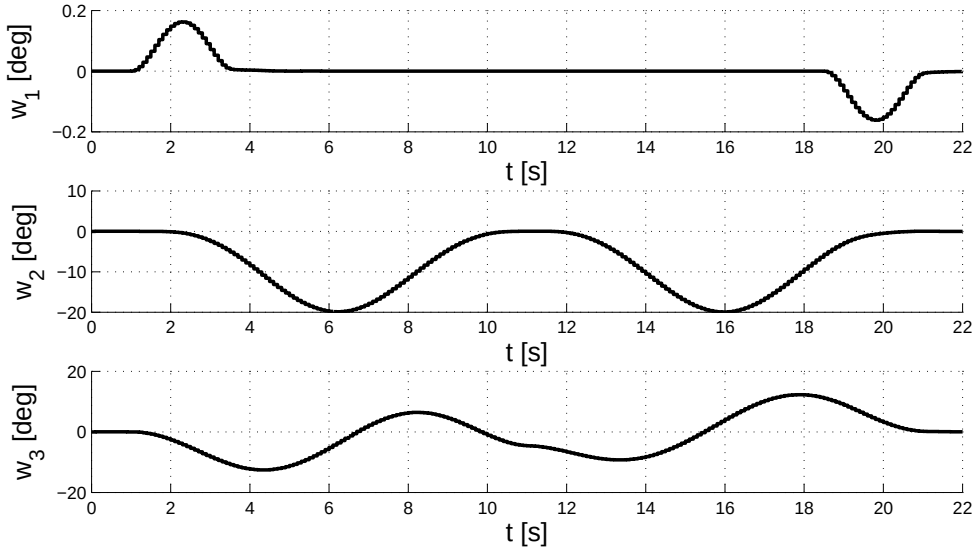

Figure 6.13: Tilting rotors angle command for the 360° yaw turn maneuver, comparison between the standard case (dashed line) and the tilting rotor configuration (solid line)

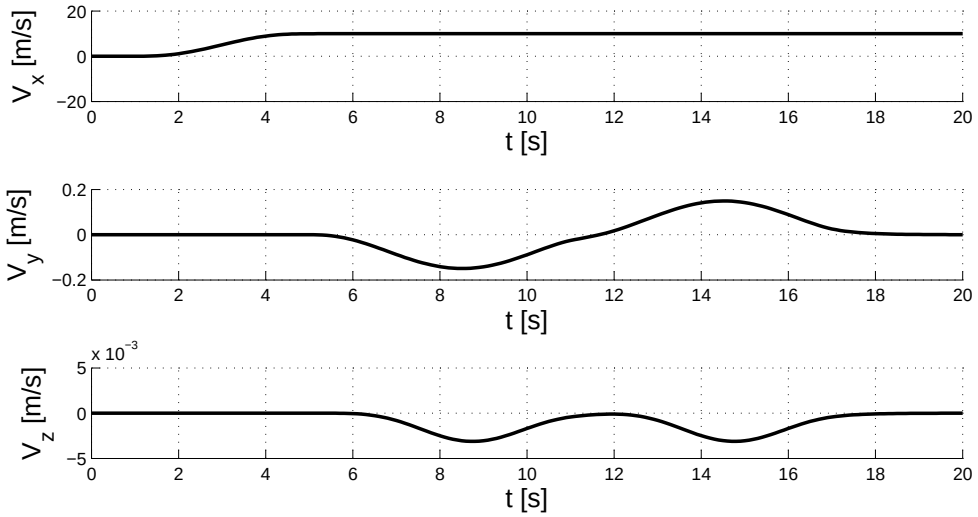

Figure 6.14: Inertial speed for the 90° roll tilt maneuver

maneuver starts with a small increment for w_3 that accelerates the vehicle in the x-direction, than w_2 takes over and this command provides most of the control power for performing the unconventional roll maneuver in forward flight, where rotors 1 and 3 are tilted for most of the duration of the maneuver.

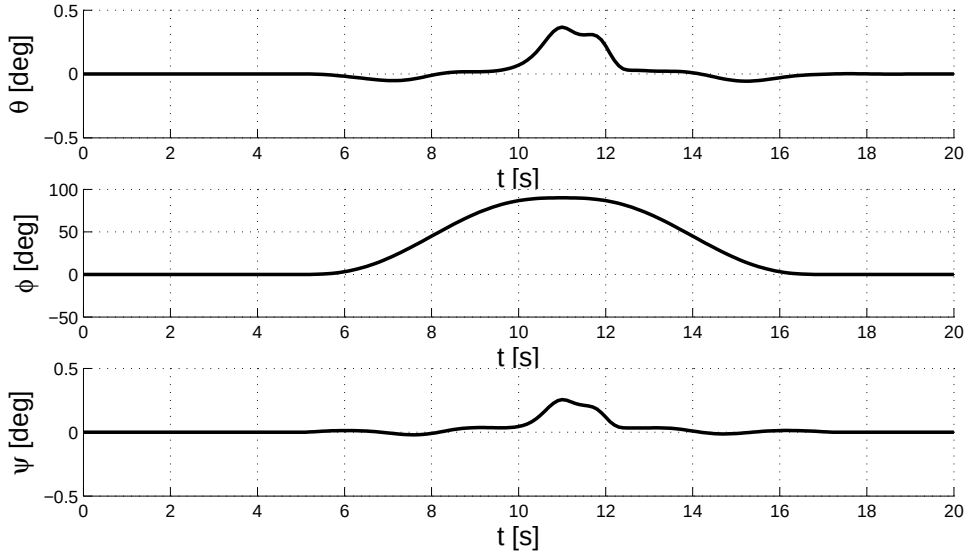

Figure 6.15: Euler angle variations for the 90° roll tilt maneuver

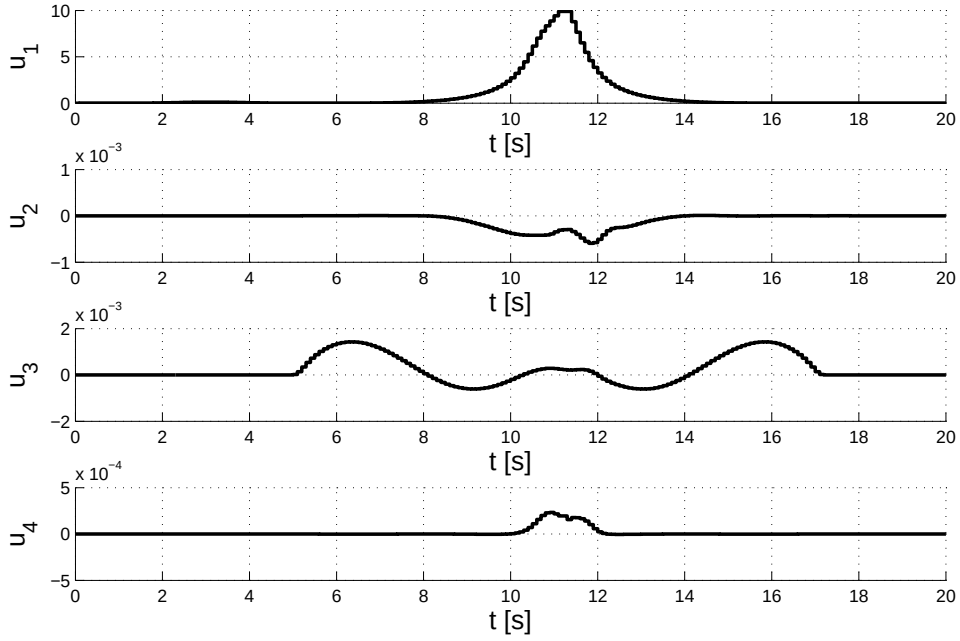

Figure 6.16: Rotor speed command for the 90° roll tilt maneuver

6.3 MPC control of a Quadrotor

The previous section described the solution of a inverse simulation problem for a simple quadrotor model. If the model used for the dynamic description of the vehicle

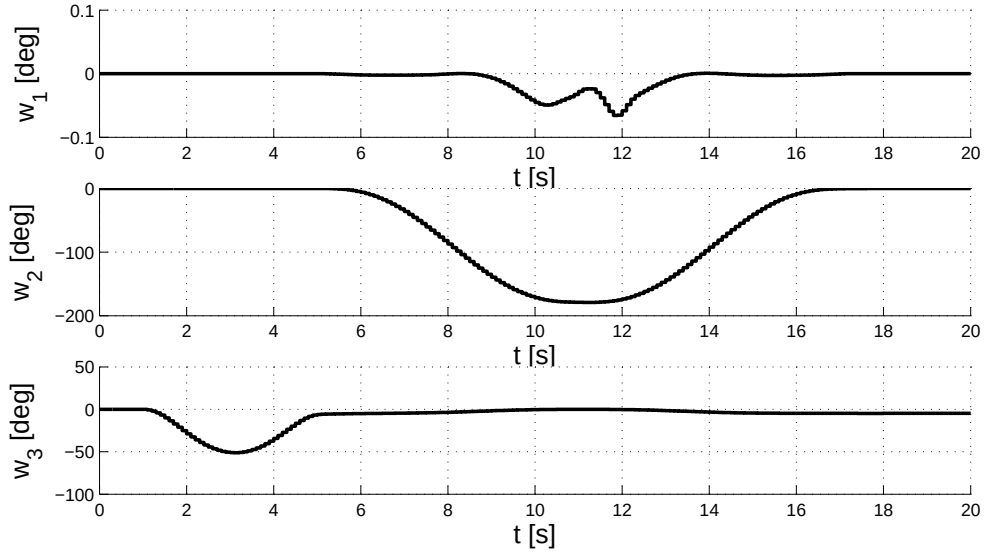

Figure 6.17: Tilting rotors angle command for the 90° roll tilt maneuver

is more complex the inverse simulation becomes too costly. The model predictive control proposed by [89] allows for the evaluation of the solution of an inverse simulation complex model, starting from the solution of the inverse simulation step obtained from a lower–order simplified model of the same vehicle. In this scheme the complex model is used only for the forward simulation step. Differently from what was done in [89] the MPC–IS scheme is implemented for a redundant problem, thus the Newton–Raphson algorithm was not suitable, but an optimization algorithm was instead implemented.

The complex model considered was that described in [24]. This model takes into account bot rotor and motor dynamics, but moreover differs from the simplified one considered above because it considers that the thrust is controlled by variation on the blade pitch for each propeller. This lead to a modification in the simplified model: the thrust was then evaluated as

$$\boldsymbol{T} = k_t \begin{bmatrix} 0 & \mathrm{s}(\delta_2) & 0 & -\mathrm{s}(\delta_4) \\ \mathrm{s}(\delta_1) & 0 & -\mathrm{s}(\delta_3) & 0 \\ -\mathrm{c}(\delta_1) & -\mathrm{c}(\delta_2) & -\mathrm{c}(\delta_3) & -\mathrm{c}(\delta_3) \end{bmatrix} \begin{Bmatrix} \sigma_1\Omega_0^2 \\ \sigma_2\Omega_0^2 \\ \sigma_3\Omega_0^2 \\ \sigma_4\Omega_0^2 \end{Bmatrix} \tag{6.7}$$

where σ_i are appropriate variables that could be rewritten as

$$\boldsymbol{\sigma} = \begin{Bmatrix} \sigma_1 \\ \sigma_2 \\ \sigma_3 \\ \sigma_4 \end{Bmatrix} = \begin{bmatrix} 1 & 0 & 1 & 1 \\ 1 & 1 & 0 & -1 \\ 1 & 0 & -1 & 1 \\ 1 & -1 & 0 & -1 \end{bmatrix} \begin{Bmatrix} u_1 \\ u_2 \\ u_3 \\ u_4 \end{Bmatrix} \tag{6.8}$$

so that the constraints on the command for the MPC–IS can remain the same as those used in the previous section.

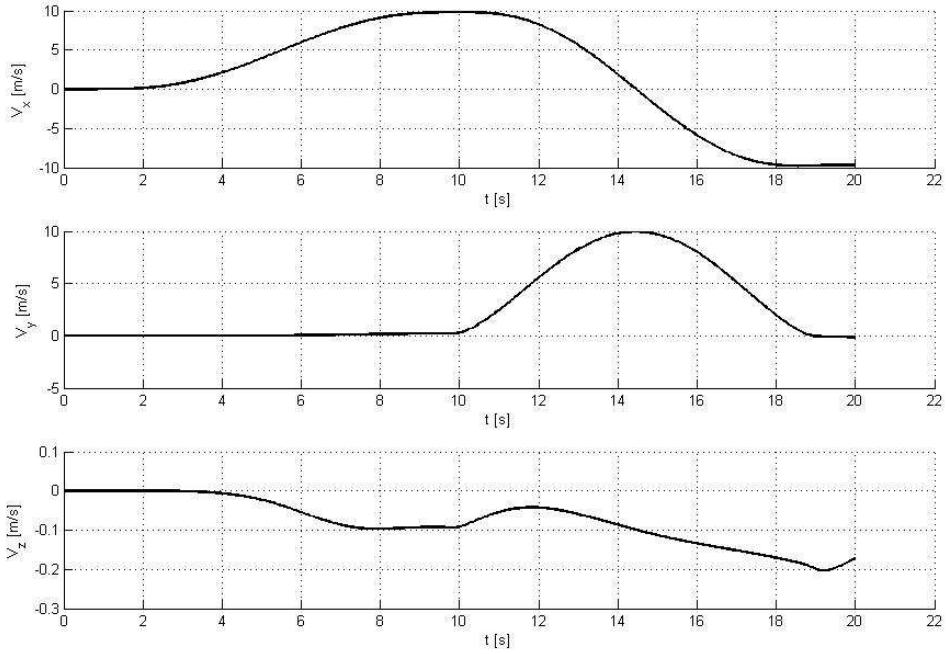

Figure 6.18: Inertial speeds for the U turn maneuver MPC–IS algorithm

Figure 6.18–6.22 present the preliminary results for the implementation of this algorithm. The maneuver considered is the same as presented in 6.2.1. Comparing with the results obtained there the main difference is that the Euler angles are not as well commanded as before and also the sideslip response is worse. The desired speeds are also in this case well followed and the considerations made on the control inputs for the previous case are still valid.

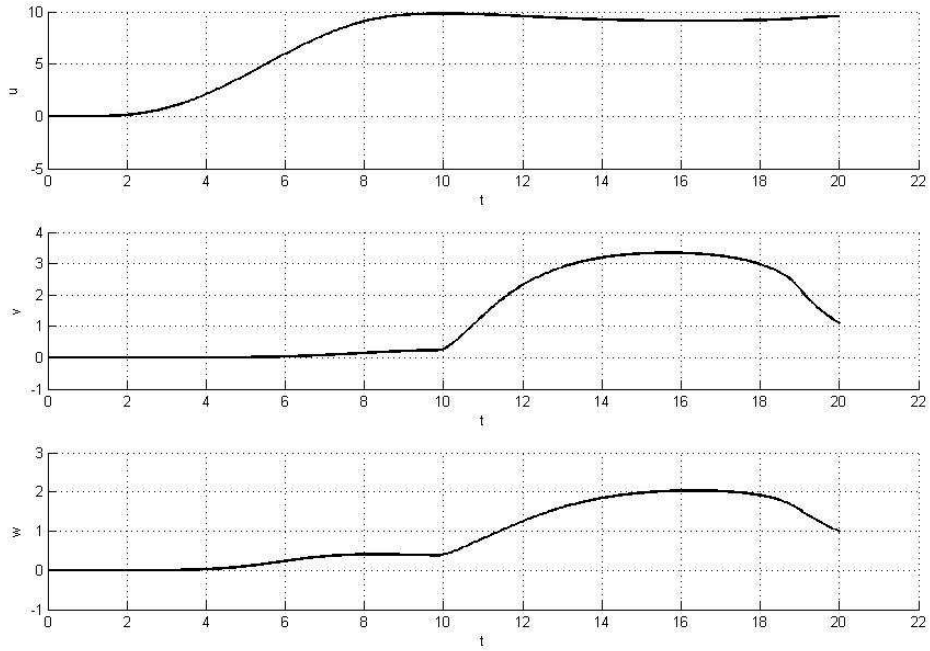

Figure 6.19: Body speeds for the U turn maneuver MPC–IS algorithm

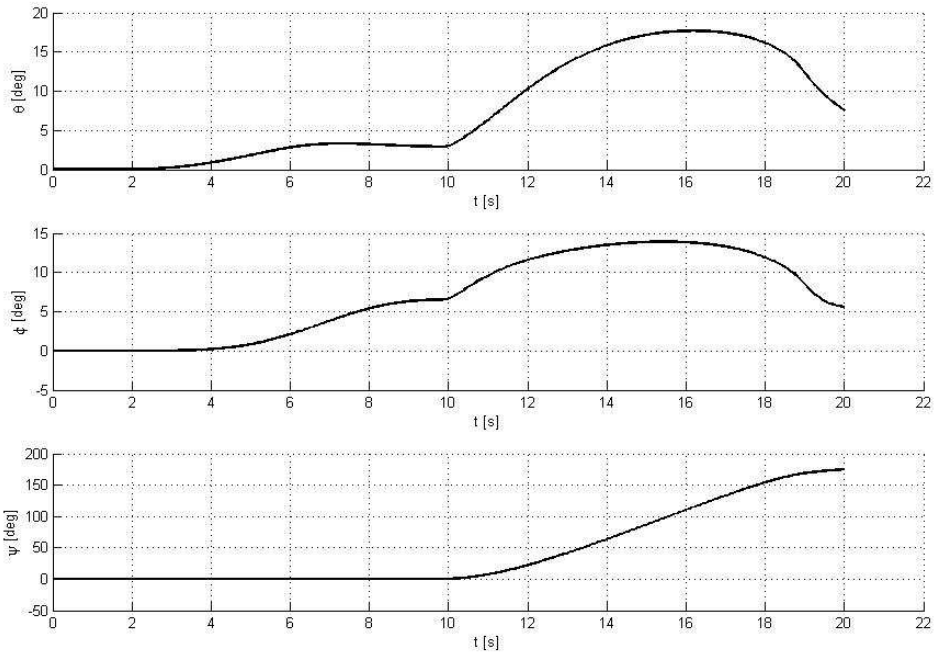

Figure 6.20: Euler angles variation for the U turn maneuver MPC–IS algorithm

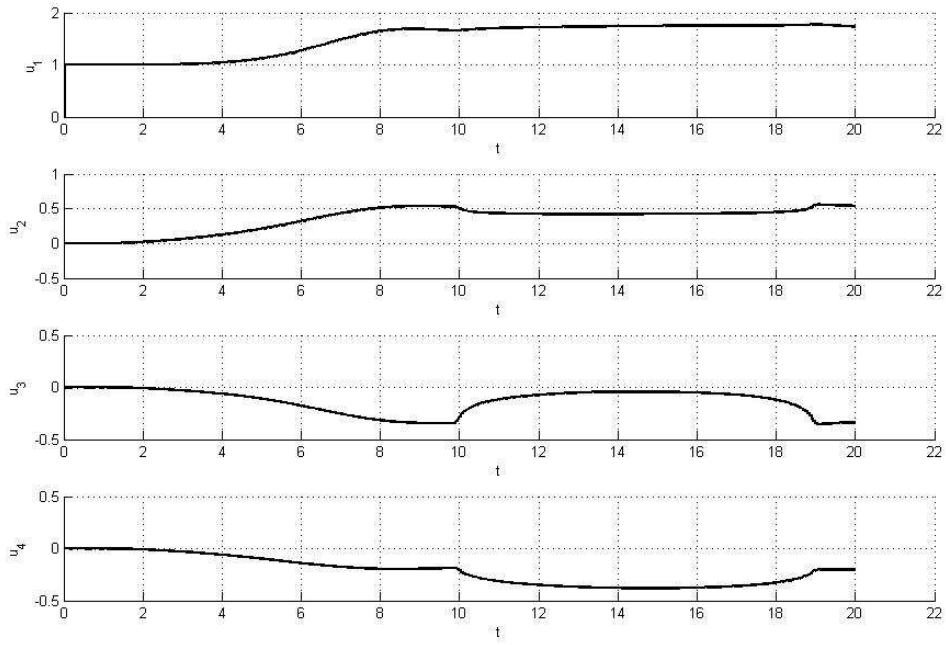

Figure 6.21: Rotor speed commands for the U turn maneuver MPC–IS algorithm

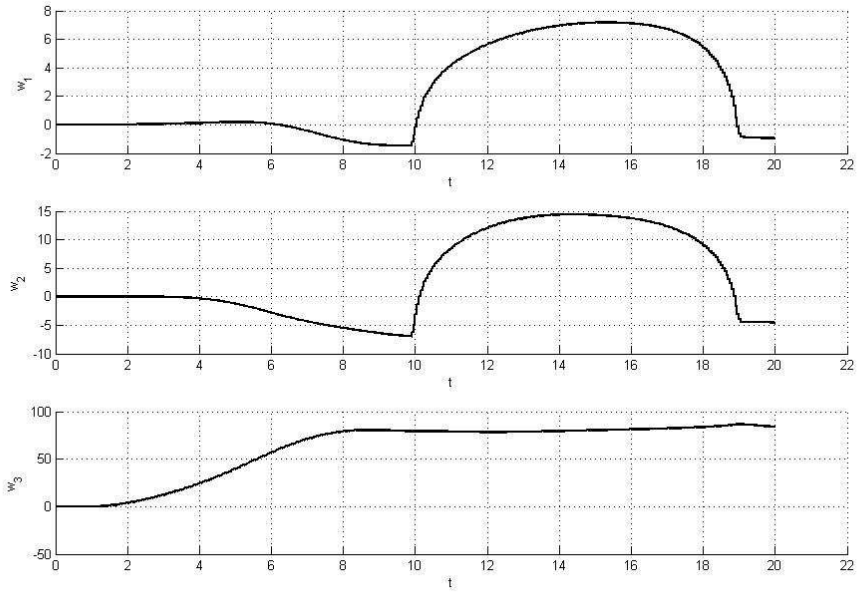

Figure 6.22: Tilting rotors angle command for the U turn maneuver MPC–IS algorithm

Chapter 7

Conclusions

Aim of this work was to provide simplified models for the analysis of flight dynamics of atmospheric vehicles that take into account specific issues of modern and innovative configurations for various classes of flying vehicles, namely fixed– and rotary–wing aircraft and small scale multi–rotor Unmanned Aerial Vehicles (UAVs). The preliminary analysis often neglects aspects like those analyzed here, but the error, as has been shown, can be quite large in some flight conditions. As stated above the reason for neglecting them is that most of the studies present in literature develop very complex models, computationally too demanding or that need large amounts of informations. During real-time simulations, the information needed are usually available, but the computation effort necessary require faster, thus more expensive, computer. The models developed in the present work quite successfully deal with this kind of problems, presenting viable approaches that could be used during preliminary design or for pilot–in–the–loop simulations. The analysis was carried on in different framework in order to show how these aspects are common for many different aircraft.

First a minimum complexity flexible aircraft model is derived, which is based on a limited set of structure parameters, which lends itself to a preliminary analysis of coupling terms between the dynamics of transport variables and deformation states. The derivation of the equations of motion hinges on a mixed Newtonian–Lagrangian approach, where linear and angular momentum balance equations are used for deriving the dynamic equations of transport variables, whereas deformation dynamics is obtained from the expression of the Lagrangian for the whole system, as a function of generalized coordinates that represent the amplitude of structure assumed modes. This modeling technique maintains a stronger link to classical rigid body equations, where coupling terms between transport and deformation variable dynamics are easily identified and their relevance assessed in terms of effect on stability and response. For the case study here considered, which represents a fictitious modern transport aircraft, the response obtained for the fully flexible and completely rigid aircraft

were compared to two quasi-static deformations models (one that consider both torsion and bending as quasi–static, while in the second only the first one dynamic was neglected) and constant moment of inertia one. From the analysis results that the quasi–static model apparently capture most of the effects of flexibility on aircraft behavior. The main advantage of the method proposed is that the magnitude of the effects considered is evaluated more easily with respect to previous works. This allows for the determination whether the effects of flexibility or its dynamics can be neglected, thus the use of one of the simplified model lead to save computational time during the simulation. The same approach, with some modification, was also considered for the analysis of helicopter blade flexibility.

Then a unified model for the description of dynamic airloads of a helicopter rotor model was discussed. The modelization of a conventional helicopter dynamics was augmented with a thin airfoil theory and a ONERA dynamic stall model. In order to determine the coefficients necessary for ONERA methods, first some tests were performed on a 2D case and compared to the wind–tunnel test of a NACA0012 airfoil. The model thus obtained was then implemented on a rotor in order to evaluate the differences with a quasi–static aerodynamic model. The same models were then liken to simplified models, that consider approximations for the higher order derivatives and states needed. From the analysis performed on the main rotor it can be asserted that the simplifications used guarantee good results with an improvement in the computational time necessary. One of the main drawback of this method is that there is still a strong dependency on wind–tunnel test or, at least, CFD analysis to determine the dynamic stall parameters, tests that are not always available for all airfoils and flight conditions. Moreover the results presented for the 3D case should be validate comparing with more results obtained from tests on a actual helicopter. Anyway the results show that the presence of unsteady aerodynamics modify the rotor loads and trim conditions, thus the overall helicopter response, but these effect are well represented also when the simplifying assumptions were considered.

Finally a novel quad-rotor configuration that features tilting rotors was analyzed in order to assess the maneuvering potential of the vehicle and possible advantages over conventional quad-rotors. When the two configurations are compared, it is shown that tilting the rotors provides a larger control power that allows to maintain a constant rotor rate. This would allow for the use of constant RPM variable pitch rotors instead of fixed pitch, variable RPM propellers. In the former case rotor thrust is controlled by means of propeller pitch, which results in a more efficient propulsion system. Moreover, the inverse simulation algorithm used for tracking three different maneuvers demonstrates that it is possible to use the additional control degrees of freedom for either minimizing the control effort or for flying with unconventional attitude, that range from a simple horizontal attitude in forward flight (instead of the usual pitch down attitude of standard quadcopters) to more

demanding transition to 90 deg roll attitude in forward rectilinear flight. The model considered is simplified, thus the implementation of the MPC–IS scheme (Model Predictive Control–Inverse Simulation) problem was considered also for a complex non–linear quadrotor model, that take into account also motor and rotor dynamics, for the forward simulation, thus obtaining more realistic results. Even if this scheme has been implemented before on a helicopter configuration, here was modified to take into account the optimization problem for a redundant case.

Bibliography

[1] Abbot W., Oliver R., J.O. B., and R.A. W., *Validation Flight Test of UH–60A for Rotorcraft System Integration Simulator (RSIS)*, Tech. rep., USAAEFA PROJECT NO. 79–24, 1982.

[2] Ahaus L.A., *An Airloads Theory for Morphing Airfoils in Dynamic Stall with Experimental Correlation*, Ph.D. Thesis, Washington University, St.Louis, Missouri, May 2010.

[3] Arra M., *L'Elicottero*, HOEPLI, Milano, Italy, 2001

[4] Avanzini, G., Capello, E., Piacenza, I., Quagliotti F., Hovakimyan, N. and Xargay, E., $\mathcal{L}_1$ *Adaptive Control of Flexible Aircraft: Preliminary Results*, AIAA Guidance, Navigation, and Control Conference, Toronto, Canada, 2-5 August 2010.
d.o.i.: 10.2514/6.2010-7501

[5] Avanzini G., De Matteis G., and Torasso A.,*Modelling Issues in Helicopter Inverse Simulation*, 36^{th} European Rotorcraft Forum ERF 2010, Paris, France, 7–9 September 2010.

[6] Avanzini G., and Giulietti F., *Quadcopter configuration with tilting rotors*, Pat. WO2013098736 A2, request No. PCT/IB2012/057589, Dec. 2012.

[7] Avanzini G., Thomson D., and Torasso A., *Model Predictive Control Architecture for Rotorcraft Inverse Simulation*, Journal of Guidance, Control & Dynamics, Vol. 36, No. 1, 2013, pp. 207–217.

[8] Beddoes T.S., *A Synthesis of Unsteady Aerodynamics Stall Effects, Including Hysteresis*, Proceeding of the First European Rotorcraft and Powered Lift Aircraft Forum, University of Southampton, England, Paper n° 17, Sep.1975.

[9] Borri M., Bottasso C.L., and Montelaghi F., *Numerical Approach to Inverse Flight Dynamics*, Journal of Guidance, Control & Dynamics, Vol. 20, No. 4, Jul.-Aug. 1997, pp. 742–747.

[10] Bramwell A., Done G., and Balmford D., *Bramwell's Helicopter Dynamics, 2^{nd} ed.*, Butterworth Heinemann, Oxford, UK, 2001

[11] Bryan, G.H., *Stability in Aviation*, MacMillan and Co., London, 1911, pp. 19–36.

[12] Buttrill, C.S., Zeiler, T.A., and Arbuckle, P.D., *Nonlinear Simulation of a*

Flexible Aircraft in Manouvering Flight,AIAA Flight Simulation Technologies Conference, AIAA Paper 87-2501-CP, Monterey, CA, August 17–19, 1987.
d.o.i.: 10.2514/6.1987-2501

[13] Carta F.O., *Unsteady Normal Investigation of Airfoil Dynamics Stall and Its Influence on Helicopter Control Loads*, U.S. Army AMRDL TR-72-51, Eustis Directorate, Sept. 1973.

[14] Cavin, III R.K., and Dusto, A.R., *Hamilton's Principle: Finite Element Methods and Flexible Body Dynamics*, AIAA Journal, Vol. 15, No. 12, 1977, pp. 1684–1690.
d.o.i.: 10.2514/3.7473

[15] Chen, R., *A Simplified Rotor System Mathematical Model for Piloted Flight Dynamics Simulation*, NASA Technical Report TM 18575, 1979.

[16] De Matteis G., De Socio L.M., and Leonessa A., *Solution of aircraft inverse problems by local optimization*, Journal of Guidance, Control & Dynamics, Vol. 18, No. 3, May-Jun. 1995, pp. 567–571.

[17] DuVal R., *A Real–Time Multi–Body Dynamics Architecture for Rotorcraft Simulation. The Challenge of Realistic Rotorcraft Simulation.*, RAeS Conference, 7–9 November 2001, pp. 9.1–9.12.

[18] Dinyavari M.A.H., and Friedmann P.P., *Application of time-domain unsteady aerodynamics to rotary–wing aeroelasticity*, AIAA Journal, 24(9):1424–1432, 1986.

[19] Dowell E.H., *A modern Course in Aeroelasticity* Sijthoff and Noordhoff, The Netherlands 1980.

[20] Dowell E.H., *A simple method for converting frequency domain aerodynamics to the time domain*, NASA TM-81844, October 1980.

[21] Dowell E.H., *Eigenmode analysis in unsteady aerodynamics: Reduced–order models*, AIAA Journal, 34(8):1548–1583, August 1996.

[22] Etkin, B., *Dynamics of Atmospheric Flight*, John Wiley & Sons, New York, 1972, pp. 104-190.

[23] Faller W.E., and Schreck S.J., *Neural Networks¿ Applications and Opportunity in Aeronautics*, Progress in Aerospace Sciences, 1996, 32 (5), pp. 433–456.

[24] Ferrarese G., Giulietti F., and Avanzini G., *Modeling and Simulation of a Quad–Tilt Rotor Aircraft*, Proceedings of the 2^{nd} RED UAS Workshop, Compiegne, France, November 20–22 2013.

[25] Gangwani S.T., *Prediction of Dynamic Stall and Unsteady Airloads on Rotor Blades*, Journal of the American Helicopter Society, 1982, 27(4), pp 57–64.

[26] Gangwani S.T., *Synthetized Airfoil Data Method for Prediction of Dynamic Stall and Unsteady Airloads*, Vertica, 1984, 8 (2), pp. 93–118.

[27] Garrick, I. E., *Propulsion of flapping and oscillating airfoil*, NACA TR 567, May 1936.

[28] Glaz B., Liu L., and Friedmann P., *Reduced order Nonlinear unsteady aerodynamics and its application to a rotor dynamic problem*, AHS Specialist-s Conference on Aeromechanics, pp. 613–634, San Francisco, CA, January 2010.

[29] Gormont R.E., *A Mathematical Model of Unsteady Aerodynamics and Radial Flow for Application to Helicopter Rotor*, U.S. Army AMRDL TR-72-67, Eustis Directorate, 1973.

[30] Greenberg J.M., *Airfoil in sinusoidal motion in a pulsating stream*, NACA TN No. 1326, June 1947.

[31] Haycock B., Grant P., *A Real-time Helicopter Model with Flexible Main Rotor Blades*, AIAA Modeling and Simulation Technologies Conference, August 2011, Portland, Oregon.

[32] Heffley R., Mnich M., *Minimum Complexity Helicopter Simulation Math Model*, NASA Technical Report CR–177476, 1988

[33] Hess R.A., Gao C., and Wang S.H., *Generalized technique for inverse simulation applied to aircraft manoeuvres*, Journal of Guidance, Control & Dynamics, Vol. 14, No. 5, Sep.–Oct. 1991, pp. 920–926.

[34] Hilbert K., *A Mathematical Model of the UH-60 Helicopter*, Tech. rep., NASA TM-85890, 1984.

[35] Hodges D.H., Ormiston R.A., *Stability of elastic bending and torsion of uniform cantilevered rotor blades in hover with variable structure coupling*, NASA Tech. Rep. TN D–8192,Ames Research Center and US Army Air Mobility RGD Laboratory, Moffett Field, Calif. 94035.

[36] Hoerner S.F., *Fluid-Dynamic Drag*, Hoerner Fluid Dynamic, 1965.

[37] Hoffmann G.H., Huang H., Waslander S.L., and Tomlin C.J., *Precision flight control for a multi–vehicle quad–rotor helicopter testbed*, Control Engineering Practice, 2011.

[38] Hovakimyan N., and Cao C., $\mathcal{L}_1$ *Adaptive Control Theory*, Society for Industrial and Applied Mathematics, Philadelphia, PA, 2010, pp. 241–259.

[39] Howlett J., *UH–60A Black Hawk Engineering Simulation Program, Volume 1: Mathematical Model*, Tech. rep., NASA CR 166309, 1981

[40] Howlett J., *UH–60A Black Hawk Engineering Simulation Program, Volume 2: Background Report*, Tech. rep., NASA CR 166310, 1981

[41] Issacs R., *Airfoil theory for flows of variable velocity*, Journal of the Aeronautical Sciences, 12(1):113–117, 1945.

[42] Johnson W., *Helicopter Theory*, Dover, New York, NY, 1994.

[43] Johnson W., *The Effect of Dynamic Stall on the Response and Airloading of Helicopter Rotor Blades*, Journal of the American Helicopter Society, vol.14, n° 2, pp.68–79, Apr.1969.

[44] Jones R. T., *Operational treatment of the nonuniform lift theory to airplane dynamics*, NACA TN 667, pages 347–350, March 1938.

[45] Junkins, J.L., and Youdan, K.,*Introduction to Dynamics and Control of Flexible Structures*, AIAA Ed. Series, USA, 1993, pp. 139–234.

[46] Kato O., and Sugiura I., *An interpretation of airplane general motion and control as inverse problem*, Journal of Guidance, Control& Dynamics, Vol. 9, No. 2, Mar.–Apr. 1986, pp. 198–204.

[47] Kendoul F., *Survey of advances in guidance, navigation, and control of unmanned rotorcraft systems*, Journal of Field Robotics, 2012.

[48] Kim F., *Formulation and validation of high-order mathematical models of helicopter flight dynamics*, Ph.D. thesis, University of Maryland College Park, 1991

[49] Leishman J., *Principles of Helicopter Aerodynamics*,2nd Ed., Cambridge University Press, New York, NY, 2006.

[50] Leishman J.G., and Beddoes, T. S., *A semi-empirical model for dynamic stall*, Journal of the American Helicopter Society, 34(3):3–17, July 1989.

[51] Lin K.C., *Comment on 'Generalized Technique for Inverse Simulation Applied to Aircraft Maneuvers'*, Journal of Guidance, Control & Dynamics, Vol.16, No. 6, Nov.–Dec. 1993, pp. 1196–1197.

[52] Lin K.C., Lu P., and Smith M., *The Numerical Errors in Inverse Simulation*, AIAA Paper 93-3588, Aug. 1993.

[53] Loewy R.G., *A two-dimensional approximation to unsteady aerodynamics in rotary wings*, Journal of the Aeronautical Sciences, 24(2):81–92, 1957.

[54] McAlister K., Lambert O., and Petot D., *Application of the ONERA model of dynamic stall*, NASA Technical Paper 2399, 1984.

[55] McCroskey W.J., *Prediction of Unsteady Separated Flows on Oscillating Airfoils*, AGARD Three Dimensional and Unsteady Separation at High Reynolds, 8, pp. 12.1–12.8, 1978.

[56] Meirovitch, L., *Principles and Techniques of Vibrations*, Prentice Hall, Upper Saddle River, NJ, 1997, pp. 501–583.

[57] Meirovitch, L., and Nelson, H. D., *On the High-Spin Motion of a Satellite Containing Elastic Parts*, Journal of Spacecraft and Rockets, Vol. 3, No. 11, 1966, pp. 1597–1602.
d.o.i.: 10.2514/3.28713

[58] Meirovitch, L., *Hybrid State Equations of Motion for Flexible Bodies in Terms of Quasi-Coordinates*, Journal of Guidance, Control, and Dynamics, Vol. 14, No. 5, 1991, pp. 1008–1013.
d.o.i.: 10.2514/3.20743

[59] Meirovitch, L., *Methods of analytical dynamics*, McGraw- Hill, New York, 1970, pp. 45–100

[60] Meirovitch, L., and Stemple, T.J., *Hybrid Equations of Motion for Flexible Multibody Systems Using Quasi-Coordinates*, Journal of Guidance, Control, and Dynamics, Vol. 18, No. 4, 1995, pp. 678–688.

d.o.i.: 10.2514/3.21447

[61] Meirovitch, L., and Tuzcu, I., *Integrated Approach to the Dynamics and Control of Maneuvering Flexible Aircraft*, NASA Technical Report CR-2003-211748, June 2003.

[62] Michael N., Scaramuzza D., and Kumar V., *Special issue on micro–UAV perception and control*, Autonomous Robots, 2012.

[63] Milne, R.D., *Dynamics of the Deformable Aeroplane*, Her Majesty's Stationary Office Reports and Memoranda, No. 3345, London, 1964.

[64] Munk M., *General theory of thin wing sections*, NACA Report 142, 1923.

[65] Padfield D.G., *Helicopter Flight Dynamics: The Theory and Application of Flying Qualities and Simulation Modeling*, 2nd ed., Blackwell Publishing, Oxford, UK, 2007.

[66] Palacios, R., Wang, Y., Karpel, M., *Intrinsic models for nonlinear flexible-aircraft dynamics using industrial finite-element and loads packages*, 53rd AIAA/ASME/ASCE/AHS/ASC Structures, Structural Dynamics and Materials Conference, Honolulu, Hawaii, 23–26 April, 2012.
d.o.i.: 10.2514/6.2012-1401

[67] Paranjape, A., Chung, S., Hilton, H., and Chakravarthy, A., *Dynamics and Performance of Tailless MAV with Flexible Articulated Wings*, AIAA Journal, Vol. 50, No. 5, 2012, pp. 1177–1188.
d.o.i.: 10.2514/1.J051447

[68] Peters D.A., *Towards a unified lift model for use in rotor blade stability analysis*, Journal of the American Helicopter Society , July 1985.

[69] Peters D.A., *How Dynamic Inflow Survives in the Competitive World of Rotorcraft Aerodynamics*, Journal of the American Helicopters Society, Vol. 54, No. 1, 2009, pp. 1–15.

[70] Peters D.A., and Ahaus L.A., *Comparison of Finite–State Dynamic Stall Theory with Unsteady Data*, 34th European Rotorcraft Forum, Sept. 16–19, 2008, Liverpool, UK.

[71] Peters D.A., and Ahaus L.A., *Unified Airloads Model for Morphing Airfoils in Dynamic Stall*, American Helicopter Society Specialist's Conference on Aeromechanics, San Francisco, California, January 20–22, 2010.

[72] Peters D.A., Barwey D., and Johnson M., *Finite–state airloads modeling with compressibility and unsteady free–stream*, in Proceedings of the Sixth International Workshop on Dynamics and Aeroelastic Stability Modeling of Rotorcraft Systems, November 1995.

[73] Peters D., HaQuang N., *Dynamic Inflow for Practical Applications*, Journal of the American Helicopters Society, Vol. 33, 1988, pp.64–68.

[74] Peters D.A., He C.J., *Finite State Induced Flow Models. Part II: Three-Dimensional Rotor Disk*, Journal of Aircraft, Vol. 32, No. 2, March-April 1995.

[75] Peters D.A., Hsieh M., and Torrero A., *A state space airload theory for flexible airfoils*, Proceedings of the American Helicopter Society 62th Annual Forum, May 2006.

[76] Peters D.A., Karunamoorthy S., Cao W., *Finite State Induced Flow Models. Part I: Two-Dimensional Thin Airfoil*, Journal of Aircraft, Vol. 32, No. 2, March-April 1995.

[77] Petot D., *Progress in the semi–empirical predictionof the aerodynamic forces due to large amplitude oscillations of an airfoil in attached or separated flow*, Proceedings of the Ninth European Forum, September 1983.

[78] Pounds P., Mahony R., and Corke P., *Modelling and Control of a Large Quadrotor Robot*, Control Engineering Practice, 2010.

[79] Prouty R., *Helicopter Performance, Stability, and Control*, Krieger, Malabar, FL, 2001.

[80] Rea, Co. J.B., *Aeroelasticity in stability and control*, Wright Air Development Center, Technical report 55-173, 1957.

[81] Stingu E., and Lewis F., *Design and Implementation of a Structured Flight Controller for a 6DoF Quadrotor Using Quaternions*, 17^{th} Mediterranean Conference on Control & Automation, Makedonia Palace, Thessaloniki, Greece, June 24–26, 2009.

[82] Talbot P., Tinling B., Decker W., and Chen R., *A Mathematical Model of a Single Main Rotor Helicopter for Piloted Simulation*, Tech. rep., NASA TM 84281, 1982

[83] Taylor, A.S., *The Present Status of Aircraft stability Problems in the Aeroelastic Domain*, Journal of the Royal Aeronautical Society, Vol. 63, No. 580, 1959, pp. 227–238.

[84] Theodore C., Celi R., *Helicopter Flight Dynamic Simulation with Refined Aerodynamics and Flexible Blade Modeling*, Journal of Aircraft, 39(4), 577-586..

[85] Theodorsen T., and Garrick I. E., *General potential theory of arbitrary wing sections*, NACA Rept. 452, 1934.

[86] Theodorsen T., *General theory of aerodynamic instability and the mechanism of flutter*, NACA Rept. 496, May 1934.

[87] Thomson D.G., and Bradley R., *Inverse simulation as a tool for flight dynamics research: Principles and applications*, Progress in Aerospace Sciences, Vol. 42, No. 3, May 2006, pp. 174–210.

[88] Tomasello A., *Modelli aerodinamici non stazionari per rotori di elicotteri*, Master of Science thesis, Università La Sapienza, Roma, .

[89] Torasso A., *Low–Order Model and Numerical Techniques for the Analysis of Rotorcraft Flight Mechanics*, Ph.D. thesis, Politecnico di Torino, 2012

[90] Turnour S., and Celi R., *Modellig of Flexible Rotor Blades for Helicopter Flight Dynamics Applications*, Journal of American Helicopter Society, Vol. 41, N. 1, 1996, pp. 52–66.

[91] Vepa R., *On the use of Padé approximants to represent unsteady aerodynamic loads for arbitrarily small motions of wings*, in Proceedings of AIAA 14th Aerospace Sciences Meeting, 1976.

[92] von Kármán T., and Burgers J. M., *General Aerodynamic Theory - Perfect Fluids, volume II*, Julius Springer, Berlin, 1935.

[93] Wagner H., *Uber die entstehung des dynamischen auftriebs von trag ugeln*, ZAMM, Bd. 5, Heft 1, pages 17–35, 1925.

[94] Waszak, M.R., Davidson, J.B., and Schmidt, D.K., *A simulation study of the flight dynamics of elastic aircraft. Volume 1: Experiment, results and analysis*, NASA-CR-4102, Langley Research Center, 1987.

[95] Wertz J.R., *Spacecraft Attitude Determination and Control*, Springer, 1978, pp. 758–760.

[96] Wilson J. and Mineck R., *Wind Tunnel Investigation of Helicopter-Rotor Wake effects oh Three Helicopter Fuselage Models*, Tech. rep., NASA TM-X-3185, 1975

[97] Yip K.M., and Leng G., *Stability analysis for inverse simulation of aircraft*, Aeronautical Journal, Vol . 102, No. 1016, 1998, pp. 345–351.

Appendix A

Definition of the rotation matrices

A.1 Coordinate Systems

For the development of the helicopter equations of motion, the following reference frames are used:

- inertial coordinate system $\mathcal{F}_I$
- body coordinate system $\mathcal{F}_B$
- wind coordinate system $\mathcal{F}_W$
- non–rotating shaft coordinate system $\mathcal{F}_S$
- rotating shaft coordinate system $\mathcal{F}_R$
- hub–wind coordinate system $\mathcal{F}_{HW}$
- rotating hub coordinate system $\mathcal{F}_H$
- blade span coordinate systems $\mathcal{F}_{BL,i}$ with $i = 1,2,\ldots,N_{BL}$
- tail rotor coordinate system $\mathcal{F}_T$

Coordinate transformation matrices between different frames are defined through suitable sets of Euler angles.

A.2 Inertial reference frame

The inertial frame is assumed fixed to a flat, non rotating Earth, $\mathcal{F}_I\{N,E,D\}$ (North–East–Down). The coordinates of the center of mass of the aircraft are defined in terms of latitude, longitude, and altitude $h = -D$.

A.3 Body axes

The body fixed reference frame $\mathcal{F}_B$ has its origin at the fuselage center of mass and moves with it. The x_B axis lies in the longitudinal plane towards the nose of the aircraft, the z_B axis lies in the longitudinal plane towards the bottom, and the y_B axis directed towards the right side of the aircraft completes a right–hand triad. Aircraft equations of motion are written in body reference frame. The attitude of the body fixed reference frame with respect to the inertial one can be described by means of roll ϕ, pitch θ, ad yaw ψ angles. The transformation between the two reference frames is given by the matrix

$$\boldsymbol{L}_{BI} = \begin{bmatrix} \cos\theta\cos\psi & \sin\psi\cos\theta & -\sin\theta \\ \sin\phi\sin\theta\cos\psi - \cos\phi\sin\psi & \sin\phi\sin\theta\sin\psi + \cos\phi\cos\psi & \sin\phi\cos\theta \\ \cos\phi\sin\theta\cos\psi + \sin\phi\sin\psi & \cos\phi\sin\theta\sin\psi - \cos\phi\cos\psi & \cos\phi\cos\theta \end{bmatrix} \tag{A.1}$$

In order to prevent singularities, Euler angles are limited in the following range

$$\begin{aligned} -\pi \leq \ & \psi \ \leq \pi \\ -\pi/2 \leq \ & \theta \ \leq \pi/2 \\ -\pi \leq \ & \phi \ \leq \pi \end{aligned} \tag{A.2}$$

A.4 Wind axes

The origin of the wind reference frame, $\mathcal{F}_W$, lies on the fuselage center of mass. The x_W axis points in the direction of the velocity, z_W towards the bottom and y_W completes a right–handed coordinate system, as shown in Fig. A.1. The transformation between the body and wind reference frames is given by

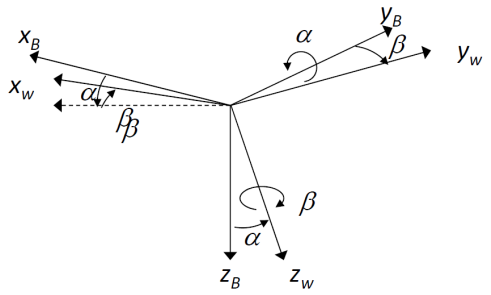

Figure A.1: Wind axes reference frame.

$$\boldsymbol{L}_{BW} = \begin{bmatrix} \cos\alpha_F\cos\beta_F & -\cos\alpha_F\sin\beta_F & -\sin\alpha_F \\ \sin\beta_F & \cos\beta_F & 0 \\ \sin\alpha_F\cos\beta_F & -\sin\alpha_F\sin\beta_F & \cos\alpha_F \end{bmatrix} \tag{A.3}$$

where α_F is the fuselage angle of attack, whereas β_F is the fuselage angle of sideslip. The velocity vector in wind axis is written as $\boldsymbol{v}_W = (V,0,0)^T$. In body reference frame it becomes

$$\boldsymbol{v}_B = \boldsymbol{L}_{BW}\boldsymbol{v}_W \tag{A.4}$$

A.5 Rotor reference frames

A.5.1 Non–rotating and Rotating shaft

Both non–rotating and rotating shaft coordinate systems, $\mathcal{F}_S$ and $\mathcal{F}_R$, have their origin at the rotor hub center, in position r_{HB} with respect to the aircraft center of mass. The orientation depends on shaft longitudinal i_θ and lateral i_ϕ tilt as shown in Fig.A.2. The transformation between body and non–rotating shaft reference frames is given by

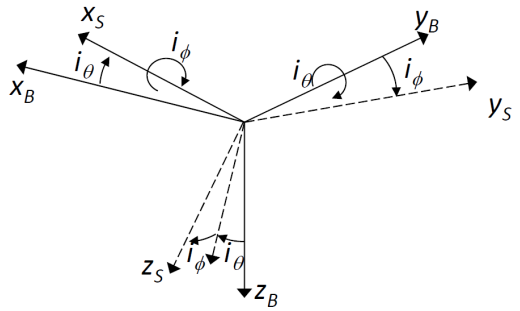

Figure A.2: Non–rotating shaft reference frame

$$\boldsymbol{L}_{SB} = \begin{bmatrix} \cos(i_\theta) & 0 & -\sin(i_\theta) \\ \sin(i_\theta)\sin(i_\phi) & \cos(i_\phi) & \cos(i_\theta)\sin(i_\phi) \\ \sin(i_\theta)\cos(i_\phi) & \sin(i_\theta) & \cos(i_\theta)\cos(i_\phi) \end{bmatrix} \tag{A.5}$$

The y_R axis of $\mathcal{F}_R$ is aligned with the reference blade, x_R axis is aligned with the reference blade advancing direction, while $z_R = z_S$ is aligned with the z axis of the non–rotating shaft frame, so that its orientation depends on the shaft longitudinal i_θ and lateral i_ϕ tilt. The rotation angle between the non–rotating and rotating shaft coordinate systems is given by the reference blade azimuth position counted from the $-x_S$ axis and positive in the direction of rotation of the rotor, as described in figure A.3. The transformation between nonrotating and rotating shaft reference frames is given by, when the rotor turns in anticlockwise direction when seen from

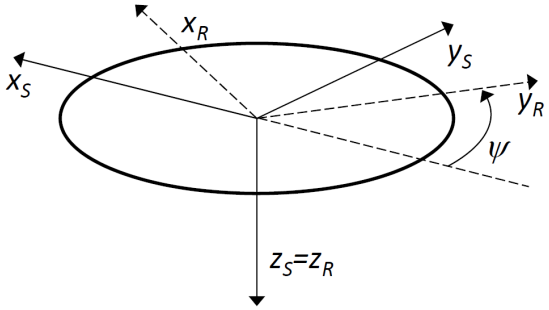

Figure A.3: Rotating shaft reference frame

above,

$$\boldsymbol{L}_{RS} = \begin{bmatrix} \sin(\psi) & \cos\psi & 0 \\ -\cos\psi & \sin\psi & 0 \\ 0 & 0 & 1 \end{bmatrix} \tag{A.6}$$

A.5.2 Blade span

The blade span coordinate system $\mathcal{F}_{Bl,i}$ with $i = 1,2,\dots N_{BL}$, is centered at the i^{th} blade hinge, in a position $r_R^{R,e} = (0,e,0)$ in the rotating shaft reference frame with respect to the rotor hub center, when an articulated rotor is considered. The y_{BL} axis is aligned with the blade, the x_{BL} axis is aligned with the blade advancing direction, and z_{BL} completes a right–handed coordinate system. The transformation between the rotating shaft (or rotating hub) and blade span reference frames depends on flap (or coning) β and lag (if present) ζ angles and on the hinge system geometry. For the UH–60A helicopter the lag and flap hinges are assumed as coincident but the lag degree of freedom anticipates the flap one. The transformation matrix is thus given by

$$\boldsymbol{L}_{BL,R} = \begin{bmatrix} \cos\zeta & -\cos\beta\sin\zeta & \sin\beta\sin\zeta \\ \sin\zeta & \cos\zeta\cos\beta & -\cos\zeta\sin\beta \\ 0 & \sin\beta & \cos\beta \end{bmatrix} \tag{A.7}$$

A.6 Tail rotor reference frame

Tail rotor coordinate system is fixed to the vehicle. The origin is placed at the tail rotor centre. The x_T axis is parallel to the x_B axis, z_T axis is aligned with the tail rotor shaft. The tail rotor is canted with respect to the fuselage around the x_T axis. The tail rotor cant angle Γ correspond to the main rotor lateral can angle i_ϕ. The

transformation matrix between body and tail reference frame is given by

$$\boldsymbol{L}_{RS} = \begin{bmatrix} 1 & 0 & 0 \\ 0 & \cos\Gamma & \sin\Gamma \\ 0 & -\sin\Gamma & \cos\Gamma \end{bmatrix} \tag{A.8}$$

Appendix B

Evaluation of the Main Rotor loads

B.1 Blade element kinematics

To describe the motion of a generic blade element, the motion of rotor hub is related to the motion of the helicopter center of mass first, then the motion of the blade element with respect to the rotor center is added. In this process the selection of the correct reference frames is fundamental in achieving a formulation as compact as possible. The equations are derived only in vector form. The components are presented only for the most important variables. The starting points in the description of blade element motion are the linear (v_B) and angular (ω_B) velocities of the helicopter in body–fixed reference frame, where

$$\boldsymbol{v}_B = (u,v,w)^T \tag{B.1}$$
$$\boldsymbol{\omega}_B = (p,q,r)^T \tag{B.2}$$

To evaluate the linear and angular speed of the hub center in non–rotating frame, the position vector r_B^H of the hub center in body frame is required,

$$\boldsymbol{r}_B^H = (x_H,y_H,z_H)^T \tag{B.3}$$

Using the transformation matrix $\boldsymbol{L}_{SB}$ from body to non–rotating shaft reference frames (see A.5) the linear and angular speed in non–rotating shaft are evaluated as

$$\boldsymbol{v}_S = (u_S,v_S,w_S)^T = \boldsymbol{L}_{SB}\boldsymbol{v}_B^S = \boldsymbol{L}_{SB}\left(\boldsymbol{v}_B + \boldsymbol{\omega}_B \times \boldsymbol{r}_{HB}\right) \tag{B.4}$$
$$\boldsymbol{\omega}_S = (p_S,q_S,r_S)^T = \boldsymbol{L}_{SB}\boldsymbol{\omega}_B^S = \boldsymbol{L}_{SB}\boldsymbol{\omega}_B \tag{B.5}$$

The body frame and the non–rotating frame are both fixed to the fuselage. The only difference lies in the shaft tilt angles i_θ and i_ϕ in the longitudinal and lateral plane

respectively. The relative rotation speed $\boldsymbol{\omega}_B^{S/B}$ between the two reference frames is equal to zero and the transformation matrix $\boldsymbol{L}_{SB}$ is constant in time. In the description of blade motion and rotor force and moments the components of linear and angular motion in the non–rotating frame are used in place of the components in body frame to save the overhead of the rotation matrix and radius between center of gravity and hub center.

The rotating shaft reference frame shares the same origin with the non–rotating one, but the relative angular speed between the two frames $\boldsymbol{\omega}_R^{R/S}$ is determined by the rotor angular speed. For an anticlockwise rotation of the rotor when seen from above, $\boldsymbol{\omega}_R^{R/S} = (0,0,-\Omega)^T$. Linear and angular speed in rotating frame are

$$\boldsymbol{v}_R = \boldsymbol{L}_{RS}\boldsymbol{v}_S \tag{B.6}$$

$$\boldsymbol{\omega}_R = \boldsymbol{L}_{RS}\boldsymbol{\omega}_S^S + \boldsymbol{\omega}_R^{R/S} = \boldsymbol{L}_{RS}\boldsymbol{\omega}_S^S + (0,0,-\Omega)^T \tag{B.7}$$

To evaluate the speed of a generic blade element, the position vector $\boldsymbol{r}_R^{R,BL}$ with respect to the origin of the rotating shaft reference frame is defined for a generic blade element. This vector is characterized by two parts: the first part describes the distance of the flap/lag hinge from the rotor center along blade span, whereas the second term accounts for the radial distance r of the blade element from the hinge in blade reference frame:

$$\boldsymbol{r}_R^{R,b} = (0,e,0) + \boldsymbol{L}_{R,BL}(0,r,0)^T \tag{B.8}$$

The speed of the generic blade element in rotating shaft frame is thus given by

$$\boldsymbol{v}_R^{BL} = \boldsymbol{v}_R + \boldsymbol{\omega}_R \times \boldsymbol{r}_R^{R,BL} + \dot{\boldsymbol{r}}_R^{R,BL} \tag{B.9}$$

Finally, the speed of the blade element in blade span reference frame can be evaluated as:

$$\boldsymbol{v}_{BL} = \boldsymbol{L}_{BL,R}\boldsymbol{v}_R^{BL} \tag{B.10}$$

To determine rotor inertial force, blade element acceleration is required. Among the reference frames available, the non–rotating shaft is preferred, as it allows to write the equations in the most compact form. To evaluate the acceleration of the blade element, as a first step the blade element speed is transformed into non–rotating shaft components:

$$\boldsymbol{v}_S^{BL} = \boldsymbol{L}_{SR}\boldsymbol{v}_R^{BL} \tag{B.11}$$

Then the acceleration is evaluated as

$$\boldsymbol{a}_S^{BL} = \dot{\boldsymbol{v}}_S^{BL} + \boldsymbol{\omega}_S \times \boldsymbol{v}_S^{BL} \tag{B.12}$$

The derivation of blade equations of motion requires the blade element accelerations written in blade span reference frame, so

$$\boldsymbol{a}_{BL}^{BL} = \boldsymbol{L}_{BL,R}\boldsymbol{L}_{RS}\boldsymbol{a}_S^{BL} \tag{B.13}$$

B.2 Aerodynamic loads

Equation B.10 can be modified in order to include the speed of the blade element with respect to the surrounding air including the effect of the inflow. In this respect, the usual approach presented in the literature (see for example [48]) is to write the components of $\boldsymbol{v}_{BL}$ in terms of tangential, radial and vertical terms,

$$\boldsymbol{v}_{BL} = U_T \boldsymbol{i}_{BL} + U_R \boldsymbol{j}_{BL} + U_P \boldsymbol{k}_{BL} \tag{B.14}$$

where the components U_T ,U_R, and U_P are

$$\begin{aligned} U_T &= [u_S \sin(\psi+\zeta) + v_S \cos(\psi+\zeta)] - e(r_S - \Omega)\cos\zeta + r\left\{\dot{\zeta}\cos\beta + \right. \\ &\quad \left. + \sin\beta\,[p_S \cos(\psi+\zeta) - q_S \sin(\psi+\zeta)] - (r_S - \Omega) cos\beta\right\} \qquad \text{(B.15)} \\ U_R &= -[u_S \cos\beta \cos(\psi+\zeta) - v_S \cos\beta \sin(\psi+\zeta) + w_S \sin\beta] + \\ &\quad -e\,[sin\beta(q_S \cos\psi + p_S \sin\psi) + (r_S - \Omega)\cos\beta \sin\zeta] + U_{R\lambda} \qquad \text{(B.16)} \\ U_P &= [-u_S \sin\beta \cos(\psi+\zeta) + v_S \sin\beta \sin(\psi+\zeta) + w_S \cos\beta] + \\ &\quad +e\,[cos\beta(q_S \cos\psi + p_S \sin\psi) - (rS - \Omega)\sin\beta \sin\zeta] + \\ &\quad +r\left[-\dot{\beta} + q_S \cos(\psi+\zeta) + p_S \sin(\psi+\zeta)\right] + U_{P\lambda} \qquad \text{(B.17)} \end{aligned}$$

The contribution of the inflow to the local velocity components assuming a three–states triangular inflow model (described in 3.4.2) are

$$U_{R\lambda} = \omega R \sin\beta \left\{ -\ni_0 - \epsilon\,(\ni_c \cos\psi + \ni_s \sin\psi) - \frac{r}{R}\,[\ni_c \cos(\psi+\zeta) + \ni_s \sin(\psi+\zeta)]\right\} \tag{B.18}$$

$$U_{P\lambda} = \omega R \cos\beta \left\{ -\ni_0 - \epsilon\,(\ni_c \cos\psi + \ni_s \sin\psi) - \frac{r}{R}\,[\ni_c \cos(\psi+\zeta) + \ni_s \sin(\psi+\zeta)]\right\} \tag{B.19}$$

When the effects of inflow are included in the vertical and radial speed, the angle of attack on the blade element can be evaluated as

$$\alpha = \theta_G + \tan^{-1}\frac{U_P}{U_T} \tag{B.20}$$

where the geometric pitch θ_G at the desired blade element is given by

$$\theta_G = \theta_0 + A_{1S}\cos\psi + B_{1S}\sin\psi + \theta_{TW} + \theta_{DT} \tag{B.21}$$

In the most general case blade twist is a nonlinear function $\theta_{TW} = \theta_{TW}(r)$ which can be obtained from lookup tables as a function of blade element radial position. The dynamic twist (when included in the model) is a function of radial position through

a shape function in the spatial domain and of the generalized coordinate φ_1, which describe the motion in time, $\theta_{DT} = \theta_{DT}(r,\varphi_1)$. The dynamic twist is described in detail in B.5.

The direction φ of the airstream imping on the blade element in blade span reference frame is given by

$$\varphi = tan^{-1}\frac{U_P}{U_T} \tag{B.22}$$

The lift and drag coefficient (C_L and C_D respectively) are read from lookup tables as a function of angle of attack α and Mach number or computated using the unified theory. The blade is divided into N_s elements with width Δy_{BL} and area $S_{BL} = c\Delta y_{BL}$, which center is at a distance r_k from the blade hinges. If the elements are all equal, $\Delta y_{BL} = (R-e)/N_s$. The aerodynamic loads acting on the k^th blade elements are

$$\boldsymbol{F}_{Ak} = \left\{ \begin{array}{c} \frac{1}{2}\rho V^2 S_{BL}\left(-C_D\cos\varphi - C_L\sin\varphi\right) \\ 0 \\ \frac{1}{2}\rho V^2 S_{BL}\left(C_D\sin\varphi - C_L\cos\varphi\right) \end{array} \right\} \tag{B.23}$$

where $V^2 = U_P^2 + U_T^2$. The aerodynamic load is assumed to act at the midpoint r_k of the blade element. The total aerodynamic shear forces at the hinge and the aerodynamic moments about the hinge in blade span frame for the i^{th} blade are given by

$$\boldsymbol{F}_{A,i_{BL}} = \sum_{k=1}^{N_s} \boldsymbol{F}_{Ak} \tag{B.24}$$

$$\boldsymbol{M}_{A,i_{BL}} = (M_{\beta A},0,M_{\zeta A})^T = \sum_{k=1}^{N_s} \boldsymbol{r}_k \times \boldsymbol{F}_{Ak} \tag{B.25}$$

The force and moments of the i^{th} blade in non rotating shaft can be evaluated as

$$\boldsymbol{F}_{A,i_S} = \boldsymbol{L}_{SR}\boldsymbol{L}_{R,BL_i}\boldsymbol{F}_{A,i_{BL}} \tag{B.26}$$

$$\boldsymbol{M}_{A,i_S} = \boldsymbol{L}_{SR}\left[\boldsymbol{r}_R^e \times (\boldsymbol{L}_{R,BL_i}\boldsymbol{F}_{A,i_{BL}})\right] \tag{B.27}$$

B.3 Inertial loads

The inertia forces are derived integrating blade accelerations in the non–rotating frame, as described in B.12. Shear forces are transmitted to the rotor hub through

the hinges. The components of the inertia forces $\boldsymbol{F}_{IS} = F_{I,x_S}\boldsymbol{i}_S + F_{I,y_S}\boldsymbol{j}_S + F_{I,z_S}\boldsymbol{k}_S$ for each blade can be evaluated as

$$F_{I,x_S} = \int_e^R \rho_{BL} a_{S,x} dr \tag{B.28}$$

$$F_{I,y_S} = \int_e^R \rho_{BL} a_{S,y} dr \tag{B.29}$$

$$F_{I,z_S} = \int_e^R \rho_{BL} a_{S,z} dr \tag{B.30}$$

The main rotor inertial forces include terms which depend on state highest order derivatives. For this reason these terms need to be grouped in an inertial coupling matrix $\mathbb{M}$. As a consequence, Eq. B.28–B.30 can be rearranged in the form

$$\mathbb{M}_{F_{I,x}}\dot{x}_c = f_{F_{I,x}} \tag{B.31}$$

$$\mathbb{M}_{F_{I,y}}\dot{x}_c = f_{F_{I,y}} \tag{B.32}$$

$$\mathbb{M}_{F_{I,z}}\dot{x}_c = f_{F_{I,z}} \tag{B.33}$$

where $\mathbb{M}_{F_{I,i}}$ with $i = x,y,z$ is the array which contains the term of the inertial forces depending on highest order state derivatives and $\dot{x}_c$ is the vector which contains the derivatives of the velocity variables which are inertially coupled. These states are expressed in body fixed reference frame and the vector of coupled velocity variables for an articulated rotor with N_b blades is given by
$x_c = \left\{u_B,v_B,w_B,p_B,q_B,r_B,\dot{\beta}_i,\ldots,\dot{\beta}_{N_{BL}},\dot{\zeta}_i,\ldots,\dot{\zeta}_{N_{BL}}\right\}^T$

Equation B.31–B.33 and all the following equations in the present section are referred to the i^{th} blade. No i subscript is included in the formula in order to maintain the notation as simple as possible. The coupling matrices can be reorganized as follows

$$\mathbb{M}_{F_{I,x}} = \left(\mathbb{M}_{F_{I,x_V}}\boldsymbol{L}_{SB}, \mathbb{M}_{F_{I,x_V}}\boldsymbol{L}_{SB}\tilde{r}_B^H + \mathbb{M}_{F_{I,x_\omega}}\boldsymbol{L}_{SB}, \mathbb{M}_{F_{I,x_\beta}}, \mathbb{M}_{F_{I,x_\zeta}}\right) \tag{B.34}$$

$$\mathbb{M}_{F_{I,y}} = \left(\mathbb{M}_{F_{I,y_V}}\boldsymbol{L}_{SB}, \mathbb{M}_{F_{I,y_V}}\boldsymbol{L}_{SB}\tilde{r}_B^H + \mathbb{M}_{F_{I,y_\omega}}\boldsymbol{L}_{SB}, \mathbb{M}_{F_{I,y_\beta}}, \mathbb{M}_{F_{I,y_\zeta}}\right) \tag{B.35}$$

$$\mathbb{M}_{F_{I,z}} = \left(\mathbb{M}_{F_{I,z_V}}\boldsymbol{L}_{SB}, \mathbb{M}_{F_{I,z_V}}\boldsymbol{L}_{SB}\tilde{r}_B^H + \mathbb{M}_{F_{I,z_\omega}}\boldsymbol{L}_{SB}, \mathbb{M}_{F_{I,z_\beta}}, \mathbb{M}_{F_{I,z_\zeta}}\right) \tag{B.36}$$

Inertial moments are generated by the inertial shear forces that the blade transmit to the hub at the flap/lag hinge, which is placed at a distance e with respect to the hub center. Rotor inertial moments $\boldsymbol{M}_{IS} = M_{I,x_S}\boldsymbol{i}_S + M_{I,y_S}\boldsymbol{j}_S + M_{I,z_S}\boldsymbol{k}_S$ in the non–rotating frame are thus evaluated as

$$\boldsymbol{M}_{IS} = \boldsymbol{r}_S^e \times \boldsymbol{F}_{IS} \tag{B.37}$$

where the position of the flap/lag hinge in non–rotating frame is $r_S^e = (-e\cos\psi_i, e\sin\psi_i, 0)^T$.

The i^{th} blade inertial forces and moments can be summed up as:

$$\mathbb{M}_{FI,i}\dot{x}_c = \boldsymbol{F}_{I,i_S} = \boldsymbol{f}_{FI} \quad (B.38)$$

$$\mathbb{M}_{MI,i}\dot{x}_c = \boldsymbol{M}_{I,i_S} = \boldsymbol{f}_{MI} \quad (B.39)$$

B.4 Blade equations of motion

The derivation of the blade equations of motion for articulated blades follows the approach proposed in Refs. [Howlett, Kim]. The flap and lag equations of motion are formulated by enforcing moment balance around the hinges. The applied moments can be divided into aerodynamic moments ($M_{\beta A}$ and $M_{\zeta A}$), inertial moments ($M_{\beta I}$ and $M_{\zeta I}$), hinge spring moments ($M_{\beta K}$ and $M_{\zeta K}$), and lag damper moments ($M_{\beta LD}$ and $M_{\zeta LD}$). The moment balance can be expressed as

$$M_{\beta A} + M_{\beta I} + M_{\beta K} + M_{\beta LD} = 0 \quad (B.40)$$

$$M_{\zeta A} + M_{\zeta I} + M_{\zeta K} + M_{\zeta LD} = 0 \quad (B.41)$$

The expressions for aerodynamic moments are derived in B.2 whereas lag damper loads are presented in B.6. The inertial moments are derived by integrating the contribution of the acceleration of each differential blade element dr along blade span. If we define ρ_{BL} as the linear mass density of the blade and take the acceleration of the blade element in blade span reference frame $\boldsymbol{a}_{BL}^{BL}$, as described in Eq. B.13, the moment of inertial forces is given by

$$M_{\beta I} = -\int_e^R r\rho_{BL}a_z dr \quad (B.42)$$

$$M_{\zeta I} = -\int_e^R r\rho_{BL}a_x dr \quad (B.43)$$

where a_x and a_z are the components of the acceleration $\boldsymbol{a}_b^b = a_x\boldsymbol{i}_{BL} + a_y\boldsymbol{j}_{BL} + \boldsymbol{k}_{BL}$ along x and z axes evaluated in Eq. B.13. The equations are written including the hinge stiffness term for the seek of generality. The UH-60A helicopter has no springs in the flap and lead/lag hinges and as a consequence no contribution of stiffness in the flap and lag equations.

The equations derived can not be directly used in the simulation, as flap and lag accelerations depend on the derivative of rigid body velocity variables, that is, flap and lag dynamics are inertially coupled to fuselage degrees of freedom. As in the previous section dedicated to the inertial forces and moments, the elements of the coupling matrix here described are referred to the i^{th} blade. A subscript i is omitted

for the seek of conciseness. The flap and lag equation can be cast in matrix form as

$$\mathbb{M}_\beta \dot{x}_c = f_\beta \tag{B.44}$$
$$\mathbb{M}_\zeta \dot{x}_c = f_\zeta \tag{B.45}$$

where the coupling matrices $\mathbb{M}_\beta$ and $\mathbb{M}_\zeta$ are given by:

$$\mathbb{M}_\beta = \left(\mathbb{M}_{\beta_V}\boldsymbol{L}_{SB}, \mathbb{M}_{\beta_V}\boldsymbol{L}_{SB}\tilde{r}_B^H + \mathbb{M}_{\beta\omega}\boldsymbol{L}_{SB}, \mathbb{M}_{\beta_\beta}, \mathbb{M}_{\beta_\zeta}\right) \tag{B.46}$$
$$\mathbb{M}_\zeta = \left(\mathbb{M}_{\zeta_V}\boldsymbol{L}_{SB}, \mathbb{M}_{\zeta_V}\boldsymbol{L}_{SB}\tilde{r}_B^H + \mathbb{M}_{\zeta\omega}\boldsymbol{L}_{SB}, \mathbb{M}_{\zeta_\beta}, \mathbb{M}_{\zeta_\zeta}\right) \tag{B.47}$$
$$\tag{B.48}$$

and the state derivative vector, $\boldsymbol{x}_c$ is the same as defined before.

B.5 Dynamic twist

Together with pilot control (θ_0, A_{1S} and B_{1S}) and built–in twist (θ_{TW}), the local feathering angle $\theta_G(r)$ of the section at station r along the blade span is affected by aerodynamic loads, that twist the rotor blades. The value of θ_G is thus given by

$$\theta_G = \theta_0 + A_{1S}\cos\psi + B_{1S}\cos\psi + \theta_{TW} + \theta_{DT} \tag{B.49}$$

The dynamic twist θ_{DT} is expressed in terms of the product of a shape function times a generalized state variable as

$$\theta_{DT} = \varphi\left[0.28 + 0.72\sin(\epsilon + \frac{r}{R})\right] \tag{B.50}$$

The dynamics of φ is described in terms of a second order dynamical system, so that the evolution of θ_{DT} is described by two states (twist amplitude and twist rate). The dynamic twist is driven by the x and z components of the aerodynamic load on the blade F_A:

$$\frac{\ddot{\varphi}(i)}{\omega_\theta^2} + \frac{2\zeta_\theta}{\omega_\theta}\dot{\varphi}(i) + \varphi(i) = K_\theta\sqrt{F_{Ax}^2 + F_{Az}^2} \qquad for i = 1, \ldots N_{BL} \tag{B.51}$$

where

$$\zeta_\theta = 0.3 \tag{B.52}$$
$$\omega_\theta = 23.63 \tag{B.53}$$
$$K_\theta = -1.17\cdot 10^{-5} - 1.72\cdot 10^{-8}(u_B - 51.42) \tag{B.54}$$

K_θ is expressed in rad/N and is bounded to $-2.04\cdot 10^{-6} \leq K_\theta \leq -1.17\cdot 10^{-5}$ so that the twist is always negative. As a consequence, when dynamic twist is accounted

for, the rotor requires more collective pitch to generate a given force compared to the case when dynamic twist is neglected. To convert the constant K_θ to metric system, and therefor be measured in rad/N, it must be multiplied by 0.0039.

The dynamic twist equation can be divided into two first order differential equations, assuming $\varphi_1 = \varphi$ and $\varphi_2 = \dot{\varphi}$, Eq. B.51 can be cast as

$$\dot{\varphi}_1 = \varphi_2 \tag{B.55}$$

$$\dot{\varphi}_2 = \omega_\theta^2 \left(K_\theta \sqrt{F_{Ax}^2 + F_{Az}^2} - \varphi_1 \right) - 2\zeta_\theta \omega_\theta \varphi_2 \tag{B.56}$$

B.6 Lag damper

The lag damper model used in the present analysis is taken from Ref. [39]. Figure B.1 presented the lag damper geometry and attachment points on both the hub and blade sides.

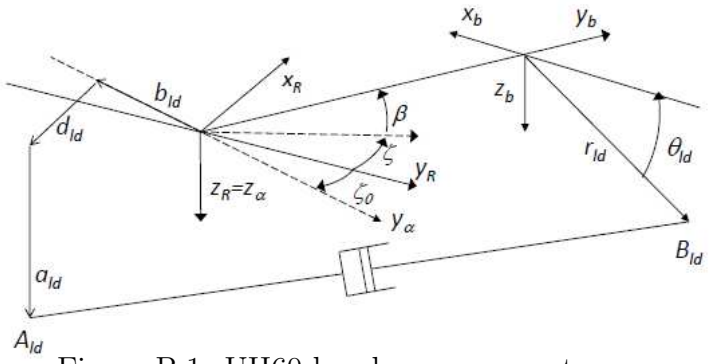

Figure B.1: UH60 lag damper geometry.

To describe the lag damper, the attention should be focused on the relative motion of the two attach points: A_{LD} is the lag damper attach point on the rotor hub, while B_{LD} is the attach point on the rotor blade. The present formulation is based on the peculiar geometry of the UH-60A lag damper, but the same approach can be used for any helicopter once its geometry is known.

For the description of lag damper geometry, a new reference frame, named α, is defined. This reference frame is centered at the flap/lag hinge (as the blade span one) and is rotated ζ_0 around the z axis. The rotation matrix $L_{\alpha R}$ between the rotating and the α reference frames is given by

$$L_{\alpha R} = \begin{bmatrix} \cos\zeta_0 & \sin\zeta_0 & 0 \\ \sin\zeta_0 & \cos\zeta_0 & 0 \\ 0 & 0 & 1 \end{bmatrix} \tag{B.57}$$

The position $\boldsymbol{r}_{\alpha}^{c,A_{LD}}$ of the lag damper attach point on the rotor hub A_{LD} with respect to the flap/lag hinge in the α reference frame is given by $\boldsymbol{r}_{\alpha}^{c,A_{LD}} = (-d_{LD}, -b_{LD}, a_{LD})^T$ The position $\boldsymbol{r}_{b}^{c,B_{LD}}$ of the lag damper attach point on the blade B_{LD} with respect to the flap/lag hinge in the blade span reference frame is equal to: $\boldsymbol{r}_{BL}^{c,B_{LD}} = (-r_{LD}\cos\theta_{LD}, c_{LD}, r_{LD}\sin\theta_{LD})^T$ where a_{LD}, b_{LD}, c_{LD}, d_{LD}, r_{LD}, θ_{LD} are parameters which define the geometry of the lag damper. The attach point A_{LD} in blade reference frame is evaluated as $\boldsymbol{r}_{BL}^{c,A_{LD}} = \boldsymbol{L}_{BL,R}\boldsymbol{L}_{R\alpha}r^{c,A_{LD}}\alpha$ so that its components are

$$\boldsymbol{r}_{BL}^{c,A_{LD}} = \left\{ \begin{array}{c} b_{LD}\sin(\zeta+\zeta_0) - d_{LD}\cos(\zeta+\zeta_0) \\ -b_{LD}\cos\beta\cos(\zeta+\zeta_0) - d_{LD}\cos\beta\sin(\zeta+\zeta_0) - a_{LD}\sin\beta \\ -b_{LD}\sin\beta\cos(\zeta+\zeta_0) - d_{LD}\sin\beta\sin(\zeta+\zeta_0) + a_{LD}\cos\beta \end{array} \right\} \quad \text{(B.58)}$$

The vector which connects the two lag damper attach points is evaluated as $\boldsymbol{r}_{BL}^{B_{LD},A_{LD}} = \boldsymbol{r}_{BL}^{c,A_{LD}} - \boldsymbol{r}_{BL}^{c,B_{LD}}$ while its length is equal to $l_{LD} = \left\| \boldsymbol{r}_{BL}^{B_{LD},A_{LD}} \right\|$. As the lag damper force is proportional to its speed, its deformation speed $\boldsymbol{v}_{BL}^{B_{LD},A_{LD}}$ is given by

$$\boldsymbol{v}_{BL}^{B_{LD},A_{LD}} = \left\{ \begin{array}{l} b_{LD}\dot{\zeta}\cos(\zeta+\zeta_0) + d_{LD}\dot{\zeta}\sin(\zeta+\zeta_0) - r_{LD}\dot{\theta}_{LD}\sin\theta_{LD} \\ b_{LD}\dot{\beta}\sin\beta\cos(\zeta+\zeta_0) + b_{LD}\dot{\zeta}\cos\beta\sin(\zeta+\zeta_0) + \\ \quad + d_{LD}\dot{\beta}\sin\beta\sin(\zeta+\zeta_0) - d_{LD}\dot{\zeta}\cos\beta\cos(\zeta+\zeta_0) - a_{LD}\dot{\beta}\cos\beta \\ -b_{LD}\dot{\beta}\cos\beta\cos(\zeta+\zeta_0) + b_{LD}\dot{\zeta}\sin\beta\sin(\zeta+\zeta_0) + \\ \quad - d_{LD}\dot{\beta}\cos\beta\sin(\zeta+\zeta_0) - d_{LD}\dot{\zeta}\sin\beta\cos(\zeta+\zeta_0) + \\ \quad - a_{LD}\dot{\beta}\sin\beta - r_{LD}\dot{\theta}_{LD}\cos\theta_{LD} \end{array} \right\} \quad \text{(B.59)}$$

The absolute speed $\boldsymbol{V}_{LD}$ of the lag damper is given by

$$\boldsymbol{V}_{LD} = \left(\left(\boldsymbol{r}_{BL}^{B_{LD},A_{LD}} \right)^T \boldsymbol{v}_{BL}^{B_{LD},A_{LD}} \right) / l_{LD} \quad \text{(B.60)}$$

and is used to generate the damping force generated by the lag damper $\boldsymbol{F}_{LD} = \boldsymbol{F}_{LD}(\boldsymbol{V}_{LD})$. In the case of the UH-60A a lookup table is used to evaluate the lag damper force as the relation between $\boldsymbol{F}_{LD}$ and $\boldsymbol{V}_{LD}$ is highly nonlinear. The moment generated by the lag damper in blade span reference is given by

$$\boldsymbol{M}_{BL}^{LD} = \frac{\boldsymbol{F}_{LD}}{l_{LD}} (\boldsymbol{r}_{BL}^{c,B_{LD}} \times \boldsymbol{r}_{BL}^{c,A_{LD}}) \quad \text{(B.61)}$$

The components along the flap and lag degrees of freedom needed in Eq. B.41 are evaluated as $M_{LD_{BL}} = (M_{\beta_{LD}}, 0, M_{\zeta_{LD}})^T$.

B.7 Equations summary

Equations B.27 and B.39 describe the aerodynamic and inertial forces and moments of the i^{th} blade expressed in non–rotating shaft. Rotor forces and moments are

obtained adding the contribution of all blades.

$$\boldsymbol{F}_{r_S} = \sum_{i_S=1}^{N_{BL}} (\boldsymbol{F}_{I,i_S} + \boldsymbol{F}_{A,i_S}) \tag{B.62}$$

and

$$\boldsymbol{M}_{r_S} = \sum_{i_S=1}^{N_{BL}} (\boldsymbol{M}_{I,i_S} + \boldsymbol{M}_{A,i_S} + \boldsymbol{M}_{LD,i_S}) \tag{B.63}$$

where $\boldsymbol{M}_{LD,i_S}$ is the moment generated by the i^{th} lag damper in non rotating shaft reference frame and evaluated as $\boldsymbol{M}_{LD,i_S} = \boldsymbol{L}_{SR}\boldsymbol{L}_{R,BL}\boldsymbol{M}_{LD,i_{BL}}$. A similar approach is followed in the coupling matrix where the effect of all blades is added

$$\mathbb{M}_{FI_S} = \sum_{i=1}^{N_{BL}} \boldsymbol{M}_{FI,i} \tag{B.64}$$

$$\mathbb{M}_{MI_S} = \sum_{i=1}^{N_{BL}} \boldsymbol{M}_{MI,i} \tag{B.65}$$

Finally rotor force and moments in body.fixed frame can be evaluated as

$$\boldsymbol{F}_r = \boldsymbol{L}_{S_b}^{-1}\boldsymbol{F}_{r_S} \tag{B.66}$$

$$\boldsymbol{M}_r = \boldsymbol{L}_{S_b}^{-1}\boldsymbol{M}_{r_S} + \boldsymbol{r}_B^H \times \boldsymbol{F}_r \tag{B.67}$$

and

$$\mathbb{M}_{F_r} = \boldsymbol{L}_{S_b}^{-1}\mathbb{M}_{FI_S} \tag{B.68}$$

$$\mathbb{M}_{M_r} = \boldsymbol{L}_{S_b}^{-1}\mathbb{M}_{MI_S} + r_B^H \times \mathbb{M}_{\boldsymbol{F}_r} \tag{B.69}$$

Blade flapping and lagging equations Eq. B.44 and B.45 are already written in a proper reference frame and need no transformation. Assuming

$x_c = \left(u_B,v_B,w_B,p_B,q_B,r_B,\dot{\beta}_i,\ldots,\dot{\beta}_{N_{BL}},\dot{\zeta}_i,\ldots,\dot{\zeta}_{N_{BL}}\right)^T$ the part of the coupling matrix which depends on the rotor can be assembled using $\mathbb{M}_{F_r}$, $\mathbb{M}_{M_r}$, $\mathbb{M}_\beta$, and $\mathbb{M}_\zeta$ as

$$\mathbb{M}_{r_c} = \begin{Bmatrix} \mathbb{M}_{F_r} \\ \mathbb{M}_{M_r} \\ \mathbb{M}_{\beta_i} \\ \vdots \\ \mathbb{M}_{\beta_{N_{BL}}} \\ \mathbb{M}_{\zeta_i} \\ \vdots \\ \mathbb{M}_{\zeta_{N_{BL}}} \end{Bmatrix} \tag{B.70}$$

This matrix is added to the contribution of the fuselage to generate the coupling matrix $\mathbb{M}_c$.

When dynamic twist is accounted for, Eq. B.56 needs to be added to include the 2^{nd} order dynamics.

Appendix C

Matrices and vectors definition for the Unsteady Thin Airfoil Theory

In this appendix the matrix and vectors necessary for the unified model derivation are defined. N is the number of inflow states used for the 2D case, while M is the number of states in the Glauert expansion.

$$
\begin{aligned}
\mathbf{1} &= \{1\ 0\ 0\ 0 \ldots\}^T \\
\boldsymbol{b} &= \{b_1\ b_2\ b_3 \ldots b_N\}^T \\
\boldsymbol{c} &= \{2\ 1\ 2/3\ 1/2 \ldots 2/N\}^T \\
\boldsymbol{d} &= \{1/2\ 0\ 0 \ldots\}^T \\
\boldsymbol{e} &= \{1\ 1/2\ 0\ 0 \ldots\}^T \\
\boldsymbol{f} &= \{0\ 1\ 2 \ldots M\}^T \\
\boldsymbol{h}_n &= \{h_0\ h_1\ h_2 \ldots h_M\}^T \\
\boldsymbol{v}_n &= \{v_0\ v_1\ 0 \ldots\}^T \\
\boldsymbol{\lambda}_0 &= \{\lambda_0\ 0\ 0 \ldots\}^T \\
\boldsymbol{\lambda}_1 &= \{\lambda_0\ \lambda_1\ 0 \ldots\}^T
\end{aligned}
$$

$$
\boldsymbol{A} = \boldsymbol{D} + \boldsymbol{d}\boldsymbol{b}^T + \boldsymbol{c}\boldsymbol{d}^T + \frac{1}{2}\boldsymbol{c}\boldsymbol{b}^T
$$

$$\boldsymbol{C} = \begin{bmatrix} f & 1 & 0 & 0 & 0 & \dots \\ -1/2 & 0 & 1/2 & 0 & 0 & \dots \\ 0 & -1/2 & 0 & 1/2 & 0 & \dots \\ 0 & 0 & -1/2 & 0 & 1/2 & \ddots \\ \vdots & \vdots & \ddots & \ddots & \ddots & \ddots \end{bmatrix}$$

$$\boldsymbol{D} = \begin{bmatrix} 0 & -1/2 & 0 & 0 & 0 & \dots \\ 1/4 & 0 & -1/4 & 0 & 0 & \dots \\ 0 & 1/6 & 0 & -1/6 & 0 & \dots \\ 0 & 0 & 1/8 & 0 & -1/8 & \ddots \\ \vdots & \vdots & \ddots & \ddots & \ddots & \ddots \end{bmatrix}$$

$$\boldsymbol{G} = \begin{bmatrix} 0 & 1/2 & 0 & 0 & 0 & \dots \\ 0 & 0 & 1/4 & 0 & 0 & \dots \\ 0 & -1/4 & 0 & 1/4 & 0 & \dots \\ 0 & 0 & -1/4 & 0 & 1/4 & \ddots \\ \vdots & \vdots & \ddots & \ddots & \ddots & \ddots \end{bmatrix}$$

$$\boldsymbol{H} = \begin{bmatrix} 0 & 0 & 0 & 0 & 0 & \dots \\ 0 & 1/2 & 0 & 0 & 0 & \dots \\ 0 & 0 & 2/2 & 0 & 0 & \dots \\ 0 & 0 & 0 & 3/2 & 0 & \ddots \\ \vdots & \vdots & \ddots & \ddots & \ddots & \ddots \end{bmatrix}$$

$$\boldsymbol{K} = \begin{bmatrix} 0 & f & 2 & 3f & 4 & \dots \\ 0 & -1/2 & 0 & 0 & 0 & \dots \\ 0 & 0 & -2/2 & 0 & 0 & \dots \\ 0 & 0 & 0 & -3/2 & 0 & \ddots \\ \vdots & \vdots & \ddots & \ddots & \ddots & \ddots \end{bmatrix}$$

$$\boldsymbol{K'} = \begin{bmatrix} f & 1/2 & 0 & 0 & 0 & \dots \\ -1/2 & 0 & 1/4 & 0 & 0 & \dots \\ 0 & -1/4 & 0 & 1/4 & 0 & \dots \\ 0 & 0 & -1/4 & 0 & 1/4 & \ddots \\ \vdots & \vdots & \ddots & \ddots & \ddots & \ddots \end{bmatrix}$$

$$\boldsymbol{M} = \begin{bmatrix} 1/2 & 0 & -1/4 & 0 & 0 & \dots \\ 0 & 1/16 & 0 & -1/16 & 0 & \dots \\ -1/4 & 0 & 1/6 & 0 & -1/24 & \dots \\ 0 & -1/16 & 0 & 3/32 & 0 & \ddots \\ \vdots & \ddots & \ddots & \ddots & \ddots & \ddots \\ 0 & 0 & 0 & -1/8M & 0 & \dfrac{M}{4(M^2-1)} \end{bmatrix}$$

$$\boldsymbol{S} = \begin{bmatrix} f & 0 & 0 & 0 & 0 & \dots \\ 0 & 0 & 0 & 0 & 0 & \dots \\ 0 & 0 & 0 & 0 & 0 & \dots \\ 0 & 0 & 0 & 0 & 0 & \dots \\ \vdots & \vdots & \vdots & \vdots & \vdots & \ddots \end{bmatrix}$$

Appendix D

Helicopter Configuration Data

This chapter collects the important configuration data for the rotorcraft used in this study.

Table D.1: Helicopter configuration data.

Fuselage	mass	m	7257.5	kg
	moments of inertia	I_{XX}	6316.8	kg m^2
		I_{YY}	52215.0	kg m^2
		I_{ZZ}	49889.0	kg m^2
		I_{XZ}	2551.6	kg m^2
Main Rotor	number of blades	N_{BL}	4	
	radius	R	8.18	m
	chord	c	0.53	m
	blade mass	m_{BL}	116.5	kg
	blade first moment	S_{BL}	385.7	kg m
	blade moment of inertia	I_{BL}	2050.8	kg m^2
	hinge eccentricity	e	0.38	m
	forward tilt	i_θ	3	deg
	lateral tilt	i_ϕ	0	deg
	blade pitch/flap coupling	δ_3	0	deg
	rotor speed	Ω	27	rad s^{-1}
	position in $\mathcal{F}_B$	r_S	[0.3,0,-2.3]	m
Tail Rotor	number of blades	N_{TR}	4	
	radius	R_{TR}	1.68	m
	cant angle	Γ	70	deg
	blade pitch/flap coupling	δ_{3TR}	35	deg
	rotor speed	Ω_{TR}	124.6	rad s^{-1}
	position in $\mathcal{F}_B$	r_{TR}	[-9.7,0.3,-2.5]	m
Horizontal Tail	surface	S_{HT}	4.18	m^2
	position in $\mathcal{F}_B$	r_{HT}	[-8.8,0,-0.46]	m
Vertical tail	surface	S_{VT}	3.00	m^2
	position in $\mathcal{F}_B$	r_{VT}	[-8.7,0,-1.2]	m